Insights into the genesis and dynamics of the solar spicule forest: aided by simulations and laboratory experiments

A Thesis

Submitted for the Degree of

Doctor of Philosophy

in the Faculty of Science

by

Sahel Dey

Department of Physics
Indian Institute of Science
Bangalore – 560 012, INDIA

July 2023

Declaration

I hereby declare that the work reported in this doctoral thesis titled “Insights into the genesis and dynamics of the solar spicule forest: aided by simulations and laboratory experiments” is entirely original and is the result of investigations carried out by me at the Indian Institute of Astrophysics (IIA) and the Department of Physics, Indian Institute of Science (IISc), Bangalore, under the supervision of Dr. Piyali Chatterjee, Associate Professor, IIA as part of the Joint Astronomy Programme.

I further declare that this work has not formed the basis for the award of any degree, diploma, fellowship, associateship, or similar title of any University or Institution.

Date: July 31, 2023
Bangalore, India

Sahel Dey
Department of Physics
Indian Institute of Science

To all my teachers

from whom I learned not only physics but many invaluable life lessons.

Acknowledgements

A Ph.D. is not just a degree but extensive training to handle various ups and downs of research activity and beyond and to stay focused over a long period of time. This long journey would not be successful without the invaluable support, encouragement, and motivation of numerous remarkable people. Here is a token of appreciation to them for making this journey memorable. First and foremost, I would like to convey my deepest gratitude to my Ph.D. supervisor, Dr. Piyali Chatterjee. For me, she is always Piyali-di. Initially, I developed a deep interest in fluid dynamics and plasma physics only after going through her highly engaging and in-depth course. Being her first Ph.D. student, I got an endless amount of her time to learn everything from scratch and discuss various aspects of the project. With her great patience, she always listens to all my queries and gives valuable input to tackle any critical problems. I greatly admire her love and passion for physics, as well as her positive attitude toward the development of our country's solar community. One can always notice her enormous motivation, work ethic, multi-tasking capabilities, and hard-working mindset. I have endeavored some of these incredible skills within my own capacity. Thank you so much, Piyali-di, for guiding me through this transformative journey. Working with you has been a truly exceptional experience for me. I am profoundly grateful to work with Murthy O.V.S.N as our collaborator. It was a fantastic learning experience for me to observe his dedication and commitment to his field of work: Laboratory experiments and physics in general. I asked many questions to understand his setups, and he always described them with great patience. I would like to thank Prof. Robertus Erdelyi from the University of Sheffield for giving me the opportunity to work closely with him. He is a global leader in the domain of Solar MHD waves and, above all, a great teacher. His great enthusiasm for exploring different arenas of Solar physics and extremely hard-working nature served as constant motivations to push my limits. For the advancement of our scientific interests, he was always there to support us in every possible way. I am also thankful to Dr. Sayan Chakrabarti, my Master's guide from IIT Guwahati, for his constant support over the years. I got the first flavor of doing research while working with him. I am also immensely grateful to my other collaborators: Chris, Marianna, and Jiajia. Their guidance, assistance,

insights, and encouragement have been invaluable in shaping my academic journey.
My heartfelt gratitude extends to the esteemed faculty members of IIA & IISc: BGS-IIA, Dean-IIA, Director-madam-IIA, Chairman-Physics department, DCC chair, Arnab-sir, Chanda mam, Tarun-sir, Rajeev, Dipu-da, Ravindra, Nagaraju, Tanmoy-da, Jayant, and Wageesh. I would like to thank all the course instructors (Piyali-di, Nirupam-da, Prateek, Bani-da, Rajaguru, Sampoorna, Nagendra-sir) who played a crucial role in shaping my basic knowledge in the field of Astrophysics. Apart from that, I always acknowledge how Nirupam-da and Prateek helped me to arrange a sitting place in B2-10 and offered a workstation there. Without such a working environment and computing facility, I couldn't continue my daily research work seamlessly. Many thanks to Prasad Hegdge and Biplob-da from the CHEP for those nice conversations in the corridor and enjoyable Table Tennis sessions in our free time. I wish to thank Susmita-di and again Nirupam-da for treating me like their own group member, for those extremely relevant discussions, and most importantly for their countless treats.
I want to acknowledge IIA, Department of Science and Technology for all financial assistance to complete this thesis. I would also like to mention GARP funding of IISc for covering all expenses during my international travel. Many thanks to the DiRAC COSMA HPC facility at Durham for providing us with valuable computational resources. A vote of thanks to all office members of the Physics department-IISc, helpdesk members of SERC, Shankar sir and Vijayalakshmi-madam from BGS-IIA, and Anish from IIA: for their continuous support and assistance. Their contributions have been vital to the successful completion of this journey.
Now it is probably once in a lifetime chance to acknowledge my batchmates, seniors, and juniors for this thesis. Here is a disclaimer that it is a completely random order in which I mention their names. Let me start with one of the most interesting characters in IISc, Subham-da. Although he was one year senior than me but the equation between us evolved to a different level than a usual senior-junior relationship. Our discussion started with some physics problems over the blackboard, and with time, it went much beyond the academic talks. From random chats to exploring exotic foods, from roaming around to handling extreme stress, he was always there at my side in different critical phases of my life. If one can ignore some rigid parts of his personality, he can easily take place in anyone's heart. Now if someone asks me with whom I have spent the most amount of time in the last six years, that would be probably Nilanjan-da. Many of his interests, e.g., coding, physics, food, and films, resonate with mine. He has also had a great impact on me in developing a soft corner for literature. I will always remember those late-night discussions on politics, future uncertainties, and various personal issues at the gymkhana ground. On the same line, I would like to mention about Sambrita-da. I know him since my college days, and I am still amazed by his breadth of knowledge in politics, Bengali literature, and history. One can literally lose track of time while in conversation with him. From

my JAP batchmates, I am very close to Prerana. She is a very open-hearted, helpful person and great in friendship. Together we shared countless cheerful office hours, spent time over exciting chats, and enjoyed a lot of good food together. I also want to mention another gem of our group, Sibaram-da. He is an achiever in winning hearts and a highly passionate, motivated person. I have many good memories with him, especially in the last few years. I hope it is not too late to acknowledge Samriddhi. Being my immediate junior from Piyali-di's group, he has helped me with many academic and non-academic issues. With his unique talent for making instant stories and jokes, he has become our constant source of entertainment. Samriddhi is really good at heart and a close companion of mine. I will miss him and especially his smiling face badly after leaving the institution. From my early groups at IISc, I would like to mention Sayantan and Parthiv. From the first day on campus, I knew Sayantan for his unique personality. He was one of the most brilliant students I have ever seen. For Parthiv, it took time to build a great bond of friendship, but after that, I always felt amazing, even in our regular conversations. Let me also thank Md. Rashid for being a very supportive, encouraging junior. With his charming character, he can make anyone feel happy. Many thanks to my recent juniors, Subhadip, Sougata, Sai, and Mayusree. Even within a short duration of time, they have become very close and essentially an integral part of my core friend groups. I have so many good memories with them, starting from daily night walks to our recent trip to Coorg. How can I forget to mention those random chats over the dinner table and weekend gatherings with food and music, which are like antidotes to my monotonous life? They have also done a lot for me, even going beyond their comfort zone. I feel lucky to have them on this journey and will do my best to keep this connection alive. Furthermore, I want to extend my heartfelt appreciation to Vikrant, Ankit, Surajit, Jayeeta-di, Alam, Prabhat, Mithun, Partha, Ayan, Biprajit, jr Jyotirmoy, Debarshi, Afsar, Tarun, Arpit, Sudeb-da, Debashmita-di, Sudipta-di, Tushar-da, Atanu-da, Prasun-da, Gopal-da, Jyotirmoy-da, Biswapriyo-da, Debargha-da, Ratan-da from IISc. Being a JAP student of both IISc and IIA, I have many friends in IIA. I want to convey my sincere gratitude to Harsh, Satabdwa, Bibhuti, Subhamoy-da, Ritesh, Naveen bhaiya, Sioree, Jyoti, Deepthi, Anirban, and Vishnu for always being supportive and considering me as part of the IIA family.

It is a great pleasure for me to say thanks to my school friends Arnab and Manas for always supporting me irrespective of the situation. They probably understand me the best after my parents. During this long Ph.D. tenure, we spent hours after hours rejuvenating childhood memories, talking about our friendships, personal struggles, and whatnot. Along with them, many thanks to my other close friends, Atanu, Debabrata, and Subhadip, for always caring for me and spending time from their busy schedules.

Lastly, I am deeply grateful to my parents for their unwavering love, care, and support in every phase of my life. I know how much struggle and sacrifice they did from my childhood to

witness this day. Due to higher studies, I couldn't stay with them for the last eight years. But they always encourage me to choose the best path for the future, even if I need to stay away. Thank you so much for being my ultimate support system and lifelong mentors. I am sure Maa and Baba will feel happiest about this achievement today. There was also someone about whom I would love to write hundreds of words. But that time has gone, and I have come far from everything. Let me only say that as time passes, only good memories persist, and I am very grateful to you for them.

Synopsis

The solar atmosphere is embedded with an enormous no of plasma structures with a vast range of spatial and temporal scales. Solar spicules are one of such ubiquitous features of the sun, which are present in millions over the entire solar disk and often appear as a forest of jets. These are magnetized plasma jets, impinging periodically on the dynamic interface region between the visible solar surface and the hot corona. From the time first reported in 1877, solar spicules have remained a puzzle to the community mainly in the absence of a unified formation mechanism, their highly dynamic nature, and their potential effect on the solar corona. A large fraction of these jets are observed in a nearly open magnetic field region on the sun, where a stream of highly energetic charged particles escapes the solar gravity, known as the solar wind. This wind fills up the entire heliosphere as a primary component of the space weather and sets up the connection between the Sun and Earth. Hence it becomes of paramount interest to investigate solar spicules, which predominately originate from the same source location of solar winds and contribute to the mass budget and acceleration of winds.

In the first part of the thesis, we will focus on the genesis of the solar spicule forest with the help of radiative Magnetohydrodynamics (rMHD) modeling and their similitudes with Laboratory experiments of fluids. Several mechanisms have been suggested to account for the formation of solar spicules, including granular squeezing, shocks and pulses, solar global acoustic waves, Alfvén waves, magnetic reconnection, magnetic tension release aided by ion-neutral coupling, and the Lorentz force. Although, models based on these drivers have not been able to quantitatively match the heights and abundance of the observed solar spicules. To start with a simple rMHD model, we do not consider the turbulent solar convection zone. We mimic the generation of global acoustic oscillations with a dominant period of 5 min instead by a sinusoidal forcing at the photospheric base of a gravitationally stratified solar-like atmospheric model. Here, the constant magnetic fields are imposed in the vertical direction. With sufficiently large amplitude forcing, these simplistic models are able to assemble a forest of synthetic spicules. In the Laboratory experiment, we find a similar jetting phenomenon at

the free surface of a polymeric fluid layer when high amplitude vertical oscillations are applied by a subwoofer speaker, also known as the Faraday excitation. To understand the threshold acceleration required to drive jets in both systems, we perform a series of numerical and tabletop experiments with different driving frequencies and accelerations. The phase plots clearly depict a similar behavior of the threshold acceleration curve with frequency for two disparate systems. One can also find the analogous nature of the interaction of magnetic fields with the plasma turbulence to long-chain polymers with thermal fluctuations in a viscoelastic fluid. The role of anisotropy in the jet formation process is further demonstrated by comparing two fluid solutions with similar viscosity and surface tension,e.g., visco-elastic fluid in the presence of polymer chains and isotropic Newtonian fluids. Under harmonic driving, numerous coherent jets form in the viscoelastic solution, whereas a large number of droplets are observed for the Newtonian fluid. The droplet formation occurs due to underlying Plateau-Rayleigh Instability, which is arrested by the turbulent energy absorption of polymer chains. For the MHD counterpart, it may be concluded that the magnetic field provides this anisotropy by collimating the rising plasma to form coherent jet structures via Maxwell's stress tensor, thereby suppressing the Kelvin-Helmholtz instability. Finally, we report the sufficient conditions (a) fluid medium, (b) gravity, (c) large-amplitude quasi-periodic driving, (d) anisotropy of the medium to excite a forest of jets irrespective of the nature of the medium by inducing non-linear development.

As a next step in realistic modeling, we include the turbulent convection zone and couple it with the stratified solar atmosphere, reaching coronal height. With sub-surface convection, solar global surface oscillation is excited self-consistently by the turbulent convection process. These dominant 5-min acoustic oscillations at the photosphere impinge on the chromosphere, transition regions, and assemble a forest of spicules with a remarkable agreement to observed characteristics. The impact of photospheric undulations steepens to large amplitude acceleration fronts or shock fronts like the Domino effect in the presence of a much less dense upper atmosphere and induces jet structures. Upon careful analysis with the Lagrangian tracking technique, we find a range of heights (6-25 Mm) amongst the simulated spicular jets. The shortest spicules generally form above the convective down-flow regions or the intergranular regions where the magnetic field opens up as a funnel. The formation of a convective plume squeezes the magnetic flux tube, forcing the plasma trapped inside to shoot upwards along the magnetic field lines into the upper atmosphere. On the contrary, long spicules are located in regions above the convective granules where the magnetic field is organized in the form of low-lying loops. It is known from previous studies that the power of the solar global oscillations reaching the atmosphere is higher over a granule than above an intergranular lane. At the chromospheric height, the resultant plasma motions can push oppositely directed magnetic field lines together, causing magnetic reconnection between the open field lines and these

low-lying loops. This mechanism aids the plasma to eject along the newly opened field lines leading to the generation of taller and faster spicules. The acceleration fronts in the higher atmosphere are generated by several mechanisms, including, e.g., (i) squeezing by granular buffeting (ii) solar global modes (iii) aided by magnetic reconnection. However, each process is ultimately controlled by the same underlying driver: solar convection. In addition to the forest feature of spicules, our model also captures their main properties, similar to observed counterparts, even in the absence of chromospheric microphysics of ambipolar diffusion and non-local thermodynamic equilibrium of the partially ionized plasma.

Finally, we shed light on the morphology of spicular jets and several observed features of their motion by combining three-dimensional rMHD simulation data sets and high-resolution solar observations. The standard perception of the spatial structure of an astrophysical jet is a conical shape. The shape and extent of jets directly relate to the filling factor of the solar atmosphere, hence of tremendous importance in estimating mass, momentum, and energy fluxes to the solar corona. In our 3D rMHD model, spicules are detected as pleated drapery of compressible plasma, in contrast to conical or tube-like geometry. These extended spicular plasma structures mainly follow the slow MHD wavefronts resulting from global acoustic oscillations. A fluted sheet-like morphology has already been observationally conjectured for spicules, although the dense sheets are reported as tangential discontinuities like in current sheets. Our laboratory fluid experiments also direct to such morphology of jets. However, the line-of-sight (LOS) integrated profile retains the bright conical structure by taking into consideration of several warps of nonuniform plasma sheets. The dynamical complexity of solar spicules is another fascinating area, which is recently advanced with the availability of high-resolution, high-cadence observations. Transverse oscillations and bulk spinning motions of spicules constitute a significant part of their rapid evolutionary phase. The observed lateral swaying or the transverse oscillation is interpreted as a manifestation of propagating fast magnetohydrodynamic (MHD) kink mode through spicules. At the same time, the bulk spinning motion is still debated and believed to be either due to torsional Alfvén waves or because of mini-filament eruption. We detect several cases of bulk spinning motions amongst clusters of spicules in our self-sustained 3D rMHD simulation data cubes. For comparison, we analyze an observed dataset from the Broadband Filter Imager (BFI) of the Solar Optical Telescope (SOT) instrument onboard the Hinode satellite, focusing on a region near the northern polar coronal hole. Time-distance diagram of LOS integrated images shows the common inter-crossing feature of spicular strands as an outcome of the bulk spinning motion for both observed and simulated jets with similar order of magnitude time periods. Upon investigating the rudimentary mechanism behind this robust spinning motion, we identify several highly dynamic, coherent helical velocity streamlines that interact with spicules in the solar atmosphere and make them

rotate. We introduce the term – coronal swirling conduits (CoSCo)– for the stream tubes since they are tall, cylindrical structures, have rotational speeds of 2–20 km/s, and average lifetime of 20–120 s. The CoSCos are parallel to the local magnetic field and, according to the dominant vorticity source, may be categorized into two classes. The CoSCo-I, or magnetic tension-driven swirls, whose origin may be traced to the lower atmosphere, where magnetic fields are continuously perturbed by the turbulent convective motions. They are characterized by co-spatial magnetic, velocity swirls, and oppositely phased velocity and magnetic field perturbations. The twisted magnetic fields at the exact location of the swirl support a strong tension force and therefore driving of CoSCo-I swirls. The second kind, CoSCo-II, is triggered next to spicules by the misaligned density and temperature gradients existing at their periphery, which is formally known as Baroclinic instability. These newly reported swirls are indirectly induced by the spicular jets in the atmosphere. For CoSCo-II, we find a prominent velocity swirl, but there is no signature of the corresponding magnetic swirl. Unlike CoSCo-I, the horizontal velocity and magnetic field vectors in CoSCo-II do not follow a 180-degree phase difference over the entire height range of the swirl. Apart from several differences, both types of CoSCos frequently overlap and rotate spicules along with them and propagate above the chromosphere regions with local Alfvén speed. Therefore detection of the rotating clusters of spicules both in observations and simulations confirms that rotating spicules are indirect tracers of CoSCos in the solar atmosphere.

Further, we comprehensively discuss the energy and mass flux contribution of spicules and swirls to the solar corona, which can support against the local radiative losses and supply mass and momentum to the solar wind. The rotational energy of swirls and mass flux contribution of spicules are anti-correlated in time as the spinning motion is mostly dominant at the falling phase of spicules under solar gravity. A curious phenomenon is also noticed regarding the mass and the Poynting fluxes carried by spicules. The Poynting flux curve is anti-correlated with spicular mass flux, although it correlates with the rotational energy of swirls. It strongly indicates that CoSCos form by drawing energy from the thermal and magnetic energy reservoir of spicular plasma and transport it to much higher heights in the atmosphere due to their tall structure. One could also deduce that the Poynting fluxes are not just transported by spicules but also by the surrounding regions that include the dimmer regions of the drapery as well as the swirls. For the horizontally averaged mass flux over the domain, a periodic profile in time is prominent due to the solar global acoustic oscillation and the Domino effect on the subsequent higher atmosphere. It is found that the simulated mass flux is also adequate to support the mass reservoir of the fast solar wind. Therefore for a complete picture of momentum and energy transport to the solar wind, it is necessary to consider this interplay effect between spicules and CoSCos.

Finally, we compare our rMHD model results with two publicly available rMHD setups from the Bifrost code. Surprisingly we find some remarkable similarities in the qualitative and quantitative aspects of the Pencil and Bifrost data cubes. However, several differences are also present in terms of the characteristics of spicules, swirls, thermodynamic quantities, and overall magnetic topology. Hence it helps us to understand essential physical processes responsible for such parallels and opens up the door to future studies for coherent physical outcomes across different numerical frameworks.

List of Publications

1. **Dey, S.**, Chatterjee, P., O. V. S. N., M. et al. Polymeric jets throw light on the origin and nature of the forest of solar spicules. Nat. Phys. **18**, 595–600 (2022).

2. **Dey, S.**, Chatterjee, P., Erdelyi E. Solar spicules as plasma drapery and their connection to coronal swirling conduits (**under review in the Nature Astronomy**)

Table of contents

List of figures **xxiii**

List of tables **xxvii**

1 Introduction **1**

1.1 The Sun . . . 1
1.2 The internal structure of the sun . . . 2
1.3 Solar atmosphere . . . 4
1.3.1 Photosphere: . . . 4
1.3.2 Chromosphere . . . 5
1.3.3 Transition region . . . 8
1.3.4 Solar Corona . . . 8
1.4 Forest of Solar spicules . . . 10
1.5 Fibrils . . . 13
1.6 Outline of the thesis . . . 15

2 Governing equations of radiative-Magnetohydrodynamics **17**

2.1 Introduction . . . 17
2.2 Mass and momentum conservation equation . . . 18
2.3 Induction equation . . . 19
2.4 Energy conservation equation . . . 20
2.5 The equation of state . . . 21
2.6 Numerical scheme . . . 22
2.7 Initial Condition . . . 23
2.8 Boundary Condition . . . 23
2.9 Radiative transfer and cooling process . . . 26
2.9.1 Radiative cooling in solar corona . . . 28

2.10 Shock diffusivity . . . 30
2.11 Semirelativistic Boris correction . . . 31
2.12 Hyperdiffusion as numerical filter . . . 33
2.12.1 Linear and Angular momentum conservative schemes . . . 33
2.13 Anisotropic thermal conductivity . . . 34
2.14 Transport coefficients . . . 36
2.15 Characteristic non-dimensional numbers . . . 38
2.16 Various physical time scales and time integration method . . . 39

3 Genesis of Solar spicule forest: from MHD simulations and laboratory experiments 41
3.1 Similarity between plasma jets and polymeric fluid jets . . . 42
3.2 Methods . . . 58
3.2.1 The radiative MHD set-up: . . . 58
3.2.2 Measure of anisotropy in the plasma . . . 63
3.2.3 Synthetic plasma emission: . . . 64
3.2.4 Lagrangian Tracking . . . 65
3.2.5 Polymeric fluid experimental set-up. . . . 65
3.2.6 Excitation experiments . . . 67
3.2.7 Polymer stretching on excitation . . . 67
3.3 Supplementary material . . . 68
3.3.1 Comparison of viscoelastic and Maxwell stresses . . . 68
3.3.2 Threshold magnetic field for suppression of Kelvin-Helmholtz instability 71
3.4 Threshold concentration for suppression of Plateau-Rayleigh instability . . . 72
3.4.1 Determination of $A_{\min}$ . . . 74

4 Dynamics of solar spicules in the presence of swirls 79
4.1 Morphology of Spicules as warped plasma sheets. . . . 80
4.2 High-resolution observations from Hinode Satellite . . . 85
4.2.1 Filtering of Hinode SOT-BFI images: . . . 86
4.3 Comparison of observed solar spicules with their simulated counterparts . . . 87
4.4 Interplay between Spicule–CoSCo . . . 90
4.4.1 Vorticity sources in MHD . . . 93
4.4.2 Classification of CoSCos . . . 94
4.5 Contribution to the energy and mass flux . . . 102
4.6 Appendix . . . 106
4.6.1 Vortex detection and visualization with ASDA and LIC . . . 106
4.6.2 Characteristics of shock-fronts . . . 106

5 A brief overview of the forest of solar spicules: from different numerical models 109
5.1 Introduction . . . 109
5.2 Description of numerical models . . . 110
5.2.1 Bifrost Code: ch024031_by200bz005 . . . 110
5.2.1.1 Bifrost Code: qs006005_dyc . . . 110
5.2.2 Pencil Code: setup1 . . . 111
5.2.3 Pencil Code: setup2 . . . 111
5.3 Results . . . 113

6 Discussions and future prospects 117
6.1 Discussions . . . 117
6.2 Future Prospects . . . 120

References 123

List of figures

1.1 Aurora Borealis: a consequence of the interaction of charged particles of solar wind and earth's magnetic field . . . 3
1.2 A high-resolution image of solar photosphere with characteristic convective granulation structure . . . 6
1.3 An on-disk view of solar chromosphere with the plethora of small-scale jet structures . . . 7
1.4 A whole disk image of solar corona filled with large-scale coronal loop structures 8
1.5 An illustration of Sun-Earth connection via solar wind and energetic events . 10
1.6 Forests of solar spicules observed with high-resolution Hα images . . . 11
1.7 Hα observation of fibrils at the vicinity of a pair of sunspots . . . 14

2.1 Initial stratification profile of thermodynamics variables for constant solar gravity 24
2.2 Variation of horizontally averaged opacity profile κ of the solar atmosphere with height (z): (i) opacity for bound-free and free-free emission (black-solid) (ii) H^- ions (red dashed) (iii) effective total opacity, $\kappa_{\rm tot}$ (blue-dot-dashed) . . 28
2.3 Behaviour of the radiative loss function for the optically thin medium with the plasma temperature . . . 29

3.1 Effect of large acceleration and anisotropy to trigger jets . . . 43
3.2 Signature of polymer stretching in the polarization experiment . . . 46
3.3 Behaviour of Kelvin-Helmholtz instability . . . 47
3.4 Comparison of 2D simulation with observation and laboratory experiment . . 49
3.5 Observed and simulated spicules seen in Si IV and Mg II emission lines . . . 51
3.6 Origin of forest of spicular plasma in the 2D simulation with convection . . . 52
3.7 Propagation of shock compression and hyper-sonic regions . . . 53
3.8 Plasma heating processes . . . 54
3.9 Comparison of height distribution of solar spicules and fluid jets . . . 55

3.10 Phase plot of vertical component of velocity versus vertical acceleration . . . 57
3.11 Solar atmospheric stratification with convection . . . 62
3.12 An example of a uniaxial extensional flow field . . . 69
3.13 The A_0–f_0 phase space to represent and compare the variation of threshold accelerations . . . 75

4.1 Examples of various magnetic field topologies in the solar atmosphere . . . 81
4.2 Spinning cluster of solar spicules from simulation and observation . . . 82
4.3 Association of the slow MHD shock fronts with spicules . . . 83
4.4 Line-of-sight integration realization of spicules . . . 84
4.5 Density and temperature profile of spicule tips . . . 85
4.6 Simulated forest of spicules as seen from different LOS angles . . . 86
4.7 A representation of the Hinode satellite . . . 87
4.8 Identification of the forest of spinning using time-distance diagrams . . . 88
4.9 Identification of spinning spicules in observations and simulations using time-distance diagrams . . . 89
4.10 Temperature distribution of spicules and CoSCos . . . 91
4.11 Presence of Alfvén waves in the solar atmosphere . . . 92
4.12 Examples of CoSCos, deeply rooted at the convective down-flow lanes of the solar photosphere . . . 95
4.13 An example of CoSCo-I which is rooted deep in the chromosphere region . . . 96
4.14 Formation mechanism of CoSCo-I and their contribution to the bulk spinning motion of spicules . . . 97
4.15 Generation of CoSCo-II from the baroclinic instability at the periphery of a synthetic spicule . . . 99
4.16 Examples of different types of CoSCos and their associated enstrophy sources 100
4.17 Correlation between spicule and swirl abundance in a periodically forced setup 101
4.18 Temporal variation of the horizontally averaged kinetic energy, mass, and Poynting energy fluxes . . . 103
4.19 Spatial distribution of the vertical Poynting flux . . . 104
4.20 Time-distance diagram of the (a) horizontally averaged Poynting flux . . . 104
4.21 Characteristics of shock-fronts . . . 107

5.1 A comparison of simulated granulation structures at the photosphere . . . 112
5.2 Stratification profile of plasma density, temperature, and plasma-β under constant solar gravity: (a) From model **PC1** (b) **Bif1** (c) **Bif2** . . . 114

5.3 A comparative analysis of line-of-sight integrated synthetic intensity profile of spicular jets 115
5.4 Association of the shock fronts with spicular jets: shock fronts are shown with green iso-contours, and synthetic intensity of spicule is presented in the vertical plane for model (a) **PC1** (b) **Bif1** (c) **Bif2** 116

List of tables

3.1 List of non-dimensional parameters to compare plasma and fluid system . . . 47
3.2 List of numerical and table top experiments 61

4.1 A list of performed 3D rMHD simulations 95

1

Introduction

1.1 The Sun

Sun is a hot, differentially spinning sphere of magnetized plasma around which a system of eight planets revolves. The existence of flora and fauna on the earth would not be possible without the continuous energy flow from the Sun. Almost every aspect of habitability on our planet relies on the closest star, either directly or indirectly. Starting from the day-night cycle, tides in the oceans and rivers, global climate, sustenance of life by means of food and energy resources are very few of an endless list. Therefore the study of our own star, the Sun, becomes one of the first steps in the understanding of the vast cosmos. Stars are one of the building blocks of the galaxy. For the Sun, Milky Way is the host spiral galaxy. The first stars of the universe were born roughly a few hundred million years after the Big Bang, going through different stages of Cosmological evolution (Tegmark et al., 1997). Although the sun was formed much later, around 9.2 billion years after the birth of the universe. There are approximately 100 billion stars in each galaxy (Maoz, 2016) and 2 trillion galaxies in the visible universe (Conselice et al., 2016). These myriads of stars can be classified into seven major categories in terms of spectral types. These are O, B, A, F, G, K, M types, in the decreasing order of surface temperature of stars. Our sun is a G-class star with an approximate surface

temperature of 5780 K. From the astrophysical point of view, it is a slowly rotating, ordinary star of mass 1.99×10^{33} gm, radius of 6.96×10^{11} cm compared to the whole family of stars. But for us, it is one of our foremost interests to understand the governing physical processes of the sun in great detail. Besides supporting life on the earth, the sun has the immense potential to disrupt our day-to-day life by expelling magnetized plasma, charged particles in the form of space weather storms towards the earth's magnetosphere. Aurora borealis or aurora australis are common incidents when highly energetic charged particles from the sun penetrate into the earth's atmosphere (Fig.1.1). These energetic events can directly impact the use of Global Positioning System (GPS), communication sectors, power grids, on which we rely completely. The systematic study of the sun goes back to the early seventeen century when Galileo discovered the telescope and observed the dark patches on the Solar surface, later known as Sunspots. Christoph Scheiner, a contemporary astronomer of Galileo, also observed spots independently (Casanovas, 1997). However, large dark spots were noticed with the naked eye by Chinese astronomers during 165 BCE. Due to the nearest position, the sun has been observed with great detail over a long time span that is nearly impossible for other stars, even with modern-day facilities. With the developments of instrumentation, and observation techniques, now Solar Physics is not limited to only images of the visible surface. It is now possible to obtain valuable insights from multi-wavelength astronomy, magnetic field, and Doppler velocity measurements with unprecedented spatial, spectral, and temporal resolution. This sheds light on the complexity of the process and reminds us that there are a large number of conundrums that are yet to be solved.

1.2 The internal structure of the sun

Sun is a main sequence star with several internal and atmospheric layers, which are distinct from each other. In this section, we will discuss the regions that form the interior of the star. The understanding of the solar inner structure is mostly developed from Helioseismology, a study of different oscillation modes of the sun.

Core region: As the name suggests, it is the closest region to the center of the star, spanning $0-25$ % of the solar radius (Priest, 2014). Here ionized hydrogens or protons go through the Fusion process at 1.5×10^7 K overcoming the coulomb repulsion force under the enormous gravitational pressure of the own weight of the sun. The fusion process follows PP chains and the CNO cycle reactions and forms Helium, gamma-ray photons, and neutrinos (Bethe, 1939). These photons then travel outward from the core, lose their energy from enormous no of scattering with dense plasma elements, and can emerge from the solar surface as blackbody radiation as late as 170000 years from their birth (Mitalas & Sills, 1992). Although neutrinos

Fig. 1.1 A spectacular view of Aurora Borealis: a consequence of the interaction of charged particles of solar wind and earth's magnetic field. Image Credit & Copyright: Christophe Suarez. source: https://apod.nasa.gov/apod/ap220404.html

reach the surface in approximately 2 seconds due to their non-interacting nature with matter. Along with Helioseismology, they are also useful in probing the internal structure of the star.
Radiative zone: This is an interface region between the core and convection zone, covering 45 % of the solar radius. As the name suggests, energy is transferred from the core region to the base of the convection zone in the form of gamma-ray and x-ray radiation.

Convection zone: This layer covers 30% of the outermost solar radius where energy is carried by the plasma parcels themselves as part of the turbulent convection process. Hot plasma cells rise against gravitational force due to the buoyancy effect and reach the top of the convection zone. There, expanding blobs radiate the heat, become cool down and go back to the convection zone. At this zone, differential rotation which varies both with depth and solar latitude plays a pivotal role. At the bottom of the zone, rotational speed changes sharply with latitudes, which is known as the Tachocline (Priest, 2014). This is the region where magnetic fields are generated by the large-scale dynamo mechanism. These magnetic fields then rise due to the buoyancy force and undergo twists as a result of the Coriolis force. Finally, at the top of the convection zone or the visible surface, the localized magnetic field appears as sunspots pairs (Zirin, 1988). Their distribution varies rapidly with solar latitude and follows a periodic cycle of eleven years, famously known as the solar cycle. Along with matter, the radiation field

tries to escape radially outward but for large density of plasma, photons are scattered. Finally at the top boundary of the convection zone, radiation can escape and the solar surface becomes visible to us.

1.3 Solar atmosphere

1.3.1 Photosphere:

This is a thin layer of the solar atmosphere that extends approximately 500 km in the vertical direction. The base of the region behaves as the blackbody, from where radiation decouples from the plasma material, and the surface becomes visible. Photosphere can be observed in several optical and near-infrared channels, e.g., Fe I, Fe XI, TiO, G-band and continuum images (Rutten & Kostik, 1982; Solanki & Stenflo, 1984; Berger & Title, 2001; Wöger et al., 2021). It is one of the highly structured and dynamic regions of the sun due to the presence of turbulent convective granules, small and large-scale magnetic features. There are several length and time scales associated with this region. Hot plasma blobs, which rise from the deep convection zone, appear as brighter expanding granules at the photosphere with a spatial scale of $1.0 - 2.0$ Mm in the horizontal direction and a lifetime of $5 - 10$ minutes (Priest, 2014) (Fig. 1.2). The horizontal size can be explained by combining the mass conservation and the fact of rapid decrease of density scale height near the photosphere, for which cell structure has to expand (Nordlund et al., 2009). The lifetime of granules is described in terms of the time periods of p-modes. After radiatively cooling down, plasma blobs become denser and descend to the convection zone by forming intergranular lanes. Doppler measurements near the center of the solar disk have shown the upward and downward vertical velocity over the granules and intergranular lanes. The correlation between the velocity and temperature of granular structures is also established (Asplund, 2005). Other than small-scale granular structures, there are cellular flow structures with $25 - 35$ Mm characteristic scale, larger horizontal rms velocity ($300 - 400$ m/s) compared to the vertical velocity ($20 - 30$ m/s), called supergranulation patterns. However, the formation mechanism of the supergranulation is not completely understood. It is suggested that several granules can merge and form these large-scale structures (Rast, 2003). In terms of the time scale, granules have a typical time scale of $4 - 6$ minutes, whereas supergranules can be visible with a lifetime of $1 - 2$ days on the photosphere (Rieutord & Rincon, 2010). Considering magnetic field structure, collapsing granules advect magnetic fields with them and often form small-scale strong concentrations of magnetic fields at the downflow lanes. These localized bright structures are known as magnetic bight points (MBP) with maximum magnetic

strength of approximately 1.3 kG and a diameter of several hundred km (Beck et al., 2007). The largest structures in the hierarchy are sunspots with a maximum diameter of roughly 60000 km, observed as dark patches in white light and G-band images (Solanki, 2003). The reduced emission from the patches is due to a lower plasma temperature than the neighborhood. It is explained with the help of magnetic fluxtubes with strength up to 3.5 kG, which provides magnetic pressure to counter the reduced gas pressure and maintain equilibrium with the outside of the tube.

There are also variations in dominant magnetic field patterns with different phases of the solar cycle. we observe different magnetic topologies dominate at the surface, known as, Active regions, Quiet Sun, and Coronal holes. An active region is single sunspot pair or a group of pairs, which is a dominant feature at the rising phase of the Solar cycle. As solar activity minimizes, the number of active regions diminishes. But there are small-scale mixed polarity regions with less magnetic fluxes, known as Quiet Sun regions. The origin of these stochastic magnetic fields is either believed to be the small-scale dynamo mechanism or the diffused magnetic field structures from the large-scale active regions (Martínez-Sykora et al., 2019). Unipolar large-scale magnetic fields also persist on the solar surface, known as Coronal holes. Due to the open magnetic field nature, the solar wind can easily escape from these regions to the heliosphere. In X-ray images, these regions appear as dark patches due to the lower plasma density. coronal holes appear at the higher latitude

1.3.2 Chromosphere

It is a highly dynamic and structured region of the atmosphere, which starts at 0.5 Mm above the solar photosphere and extends to 2 Mm height (Fig. 1.3). The average temperature profile reaches the minimum value in this layer at around 4000 K and again increases to $10000 - 20000$ K. Due to the decrement in the temperature, many ionized atoms become neutral. These neutral atoms are partially coupled to the ionized plasma only by collision as the magnetic field has no effect on neutrals. Using optically thick lines such as Hα, Ca II, Mg II, we observe immensely complex structure of the chromosphere (Pereira et al., 2014). This region also acts as an invisible boundary from where magnetic fields start to dominate the overall plasma dynamics over the gas pressure. Due to such an interface, a fraction of all propagating waves are either partially or perfectly reflected back to the photospheric surface. The characteristics of the transmitted waves are also changed after crossing this region. (Priest, 2014)

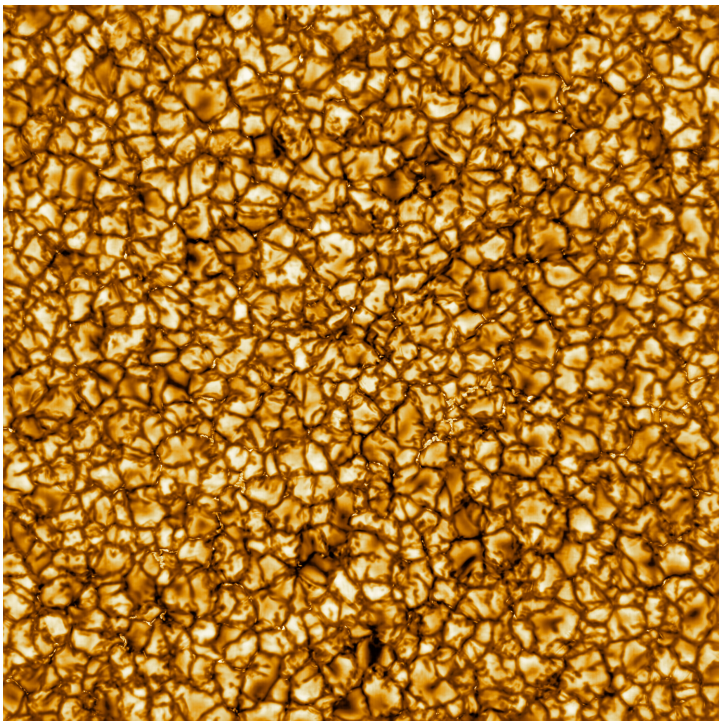

Fig. 1.2 A high-resolution image of solar photosphere with characteristic convective granulation structure. This image is observed from the Daniel K. Inouye Solar Telescope (DKIST) at 789 nm with an unprecedented resolution of 30 km. Image credit: DKIST/NSO/AURA/NSF

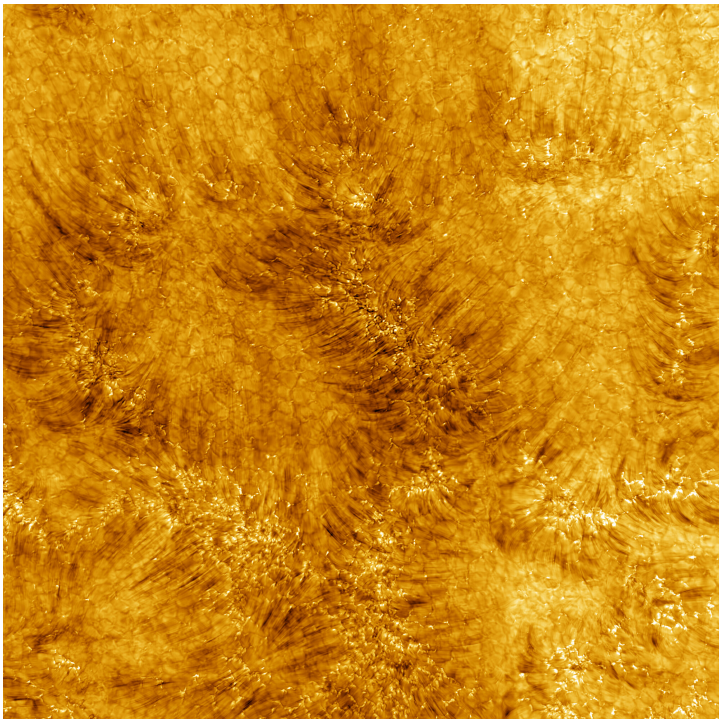

Fig. 1.3 An on-disk view of the solar chromosphere with the plethora of small-scale jet structures. This image is observed from DKIST in the hydrogen-beta line (486.13 nm). Image Credit: DKIST/NSO/AURA/NSF

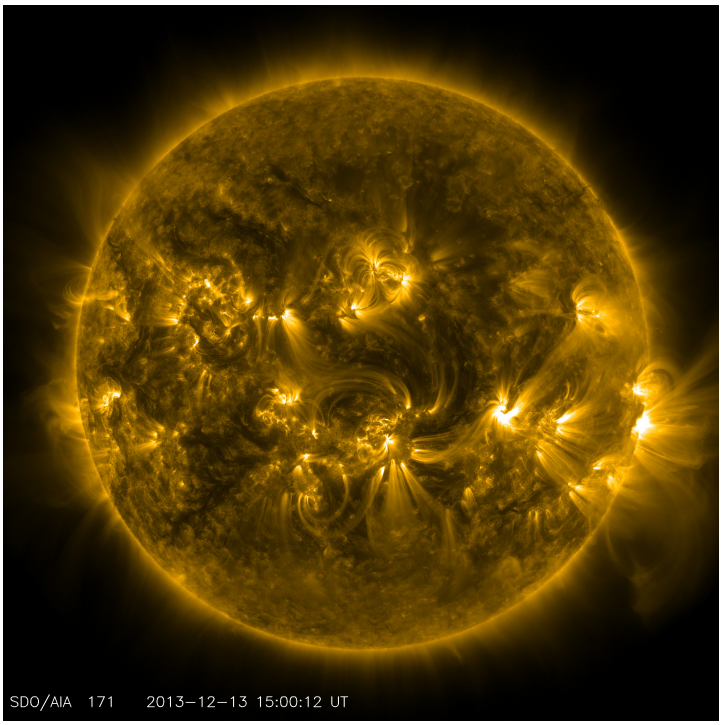

Fig. 1.4 A full disk image of solar corona filled with large-scale coronal loop structures. source: https://svs.gsfc.nasa.gov/vis/a030000/a030400/a030481/EarthSunSystem_HW.jpg

1.3.3 Transition region

This is a 100 km thick interface region between the chromosphere and the million-kelvin hot solar corona. At the base, plasma temperature is around 40000 K, and within 100 km, density rapidly falls and the temperature reaches a million Kelvin. This is one of the poorly understood although tremendous of interest. There are a few UV lines, e.g., Si IV, He II, which give us the window to study the transition region and lower corona.

1.3.4 Solar Corona

This is the outermost part of the solar atmosphere which starts from $2.0 - 2.5$ Mm. The existence of this region was first realized when the bright solar disc was blocked during the solar eclipse. The solar corona is almost 10^7 times fainter than the visible surface due to the small plasma density and this makes it impossible to observe along with the disc (Zirin, 1988). During the eclipse, observers reported a highly structured solar corona with several streamers, pseudo streamers, and a continuous flow of charged particles, known as the solar wind. The idea of solar wind was first coined by Eugene Parker in his seminal theoretical work on the

stellar wind (Parker, 1958). He first proposed that wind must originate continuously from the sun, flow radially outward against solar gravity, and fills up the whole heliosphere. Apart from wind, there are several large-scale structures, e.g., streamers, filaments, coronal loops, coronal mass ejection, flares, which are mostly governed by the coronal magnetic field (Withbroe & Noyes, 1977). For regular observations, astronomers use an occulter, which blocks the bright solar disk like an artificial eclipse and provides images of the outer coronal. With the beginning of space-based solar missions (SDO), corona was observed in several near UV and X-ray lines of Fe XIV, Fe XV atoms (Burgess, 1964) (Fig. 1.4). From ground-based facilities, this information is never accessible due to the absorption from the earth's atmosphere. With the presence of highly ionized atoms, it was realized that the coronal plasma has temperatures between $0.5 - 2$ million K. This was an utmost surprise to the Astrophysicists that plasma temperature increases with distance from the star and reaches to a million kelvin whereas the surface temperature is of the order of few thousand of Kelvin. This is popularly known as the Coronal heating problem, which apparently looks like a violation of the second law of thermodynamics. With several decades of active research in the field, people have realized that the answer to the problem lies either in the damping of myriads of Magnetohydrodynamics (MHD) waves or the turbulent magnetic reconnection process or both (Hudson, 1991). At the peak of solar activity, several large-scale transient events dominate the solar corona, e.g., flares, coronal mass ejection. Flares are large-scale flashes or electromagnetic radiation after going through the magnetic reconnection process. Coronal mass ejection is a process when a large chunk of magnetized plasma is thrown away from the solar atmosphere to the heliosphere and accelerates charged particles in the interplanetary medium. If a CME is faced along the earth, it can impact the magnetosphere of the earth and break the magnetic shielding (Fig. 1.5). Therefore these highly energetic events can pose tremendous threats to life on Earth and in space. The physics behind these individual features are entirely subjects of their own and have been studied thoroughly by a large part of the community.

In this thesis, we will focus on one of the ubiquitous chromospheric and near-transition features of the solar atmosphere, called spicules. Due to their enormous presence over the entire lower atmosphere, spicules are believed to be conduits for mass and energy from the solar chromosphere into the corona to maintain the million-kelvin temperature of Solar Corona. Even if only $\approx 1\%$ of spicular dense material is able to leave the solar atmosphere, that mass and momentum would account for the whole plasma in the solar wind (Tian et al., 2014). Hence to understand the Sun-Earth connection through solar winds, it becomes crucial to first study solar spicules as the primary component of winds.

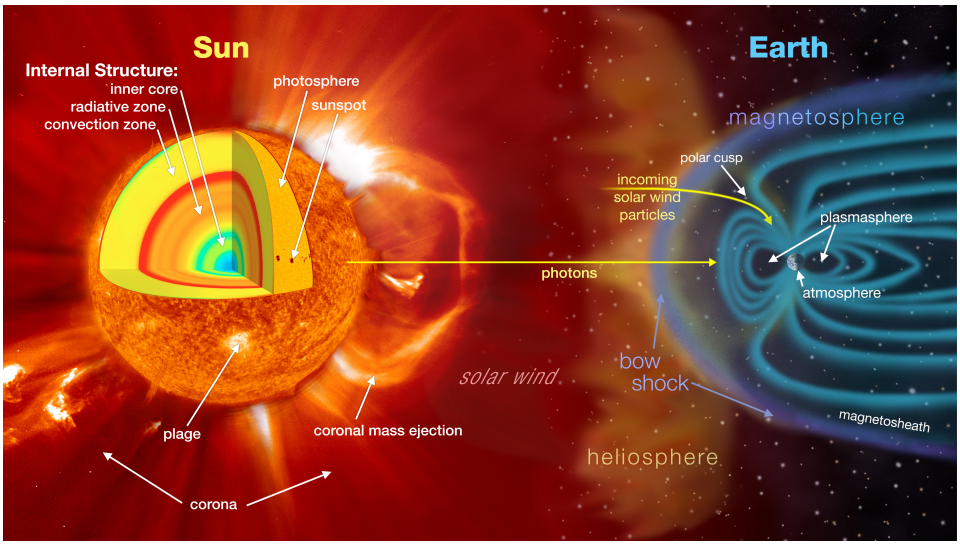

Fig. 1.5 An illustration of Sun-Earth connection via solar wind and energetic events, e.g., Coronal Mass Ejection (CME). Source: https://svs.gsfc.nasa.gov/vis/a030000/a030400/a030481/EarthSunSystem_HW.jpg

1.4 Forest of Solar spicules

The solar chromosphere is pervaded with innumerable spicules each of which are thin jets of cooler plasma shooting into the transition region and the corona. In 1877, Father Angelo Sechhi discovered that the solar atmosphere is embedded with a large number of small-scale needle-like structures, therefore making an impression of a forest of jets, called spicules (Secchi, 1877) (Fig. 1.6). Later it is realized that these fine-scale jets are comprised of dense plasma and distributed over the entire solar atmosphere in a million numbers at any given time. These jets are highly elongated with a height range between $4000 - 12000$ km, typical width $300 - 1100$ km (Beckers, 1972; Sterling, 2000; Tsiropoula et al., 2012; Samanta et al., 2019). With several lines sensitive to the density and temperature, it is realized that the spicular plasma is denser and cooler than the ambient environment. Although over their entire height range ($2 - 12$ Mm), they are multi-thermal in nature. Therefore several UV (Mg II H & K, Si IV, He II), visible (Hα) and infrared channels (Ca II, Mg II) can observe spicules with great detail (Pereira et al., 2014; Zhang et al., 2012). This approach is called Multiwavelength astronomy, which helps to get tremendous insights into these features and their subsequent impact on the higher atmosphere. One of the crucial differences between spicules and jets from eruptive events, e.g., solar flares, is that the plasma temperature at such explosive transient events are around $0.5 - 2$ Million Kelvin (MK) whereas for spicular plasma, temperature ranges in between $15000 - 80000$ K. The typical lifetime of spicules is measured in between $5 - 10$ minutes. Depending on the observation locations and magnetic topology, similar classes of jets are called

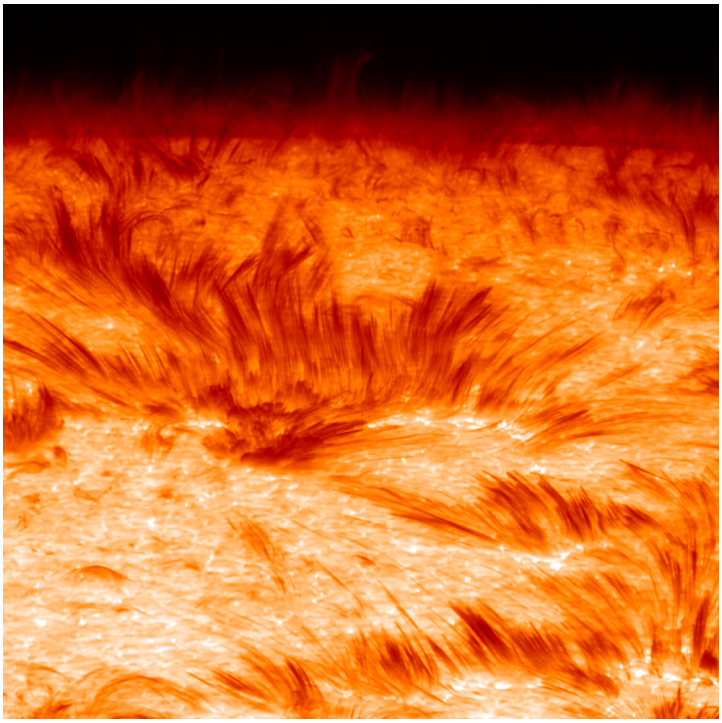

Fig. 1.6 Forests of solar spicules observed with high-resolution Hα images of Swedish 1-meter Solar Telescope (SST). Source: Wikipedia. Credit: Oystein Langangen and Luc Rouppe van der Voort

by different terms. If these jets are observed at the polar limb positions and the local magnetic fields are almost open, then they are termed spicules. Similar magnetic configurations are observed at the solar coronal holes and outside of the active regions, called plages. We will discuss akin jet structures but observed at different locations and magnetic backgrounds in the following sections. Apart from observations, spicules are very well studied by simple analytical, data-driven, ideal Magnetohydrodynamics (MHD), intricate non-ideal MHD formalisms over several decades. One of the first models was developed by De Pontieu et al. (2004), where solar global acoustic oscillations (p-modes) drive short jets by leaking acoustic energy in the solar chromosphere and forming shocks in the presence of an expanding magnetic fluxtube. With observed quasi-periodic photospheric velocities at the vicinity of an active plage region, p-modes are fed in this stratified atmosphere model. Heggland et al. (2011) performed a series of self-consistent 2D MHD simulations to describe spicules and fibril structures in the context of wave propagation. With different orientations and strengths of imposed background magnetic fields, they showed when waves reach the transition regions, jets are formed with a maximum height of 5–6 Mm. At the location of weak vertical magnetic fields similar to the network and solar plages, jets are found with a dominant periodicity of 3 minutes in the chromospheric height. For expanding regions of the fluxtubes and plages near opposite polarity with strong, inclined fields, jet structures show 5 minutes of periodicity. The impact of coronal temperature on spicule properties was studied by Iijima & Yokoyama (2015), using 2D radiation Magnetohydrodynamics (rMHD) modeling. They performed simulations with different coronal temperatures ranging 0.4, 1.0 & 2.0 MK, analogous to solar coronal holes, Quiet Sun, and active regions, respectively. It was shown that under a cooler atmosphere, spicule height becomes longer, mainly due to the lack of gas pressure component in the plasma medium. This correlation was also reported from the coronal hole and plage observations (Pereira et al., 2012; Narang et al., 2016). However, the maximum height of the simulated spicule was 5 Mm, a factor of 2–3 smaller than its observed counterparts (Zhang et al., 2012; Pereira et al., 2014). With a 2.5 D rMHD modeling of large-scale magnetic arcade environment, Martínez-Sykora et al. (2017) demonstrated spicules with speeds up to 100 km/s can be triggered by the impulsive release of magnetic tension force, aided by the ambipolar diffusion. The notable differences between their model and previously reported MHD setups are the inclusion of Ambipolar diffusion and Hall diffusion as part of the generalized Ohm's law, non-local thermodynamic equilibrium (NLTE). Here the slippage effect between the stream of ions and neutral particles, ambipolar diffusion, plays the most crucial role in transporting the magnetic fields through the colder chromospheric regions and the sudden release of magnetic tension force like a "whiplash effect" on the plasma medium. With the help of additional diffusions and currents, jet structures and solar corona are further heated up to 40,000 K and 2 MK. It is found from their model

that incorporating generalized Ohm's law is the necessary condition to generate long spicules that can reach the maximum height of 10 Mm. In a two-fluid description of the partially ionized solar atmosphere (Wójcik et al., 2020), a large number of spicular jets are excited without the presence of shocks. The collision effect between the neutrals and ions prevents the generation of shocks in the chromospheric height. Time-distance analysis performed over the duration of 50 minutes further show spicular structures can reach a maximum of 5 Mm height. A 3D rMHD model of the solar atmosphere was reported by Iijima & Yokoyama (2017), where a large number of finer jet strands are triggered mainly by the Lorentz force and appear as clusters. A tall spicule of height 10–11 Mm was detected to be driven by inclined and twisted magnetic fields emerging from the chromosphere. At the same location, streamlines are also found twisted; therefore, a swirl exists but with a twist opposite to magnetic fields. This characteristic support the presence of an enormous number of upward-moving torsional Alfvén wave at the roots of jets. An analogous mechanism of jet formation is shown, starting from a perturbative approach to a simplistic analytical model (Oxley et al., 2020; Scalisi et al., 2021) and to subsequent improved versions of the solar atmosphere modeling (Scalisi et al., 2021, 2023). The principal idea is based on the presence of magnetic bright points (MBPs) at the intergranular lanes of the photosphere, which are perturbed locally by velocity and magnetic shear. Hence the induced Alfvén wave moves upward along the magnetic flux tube and uplifts dense jet material in the chromospheric region. Recently, Liu et al. (2019) observed the ubiquity of such Alfvénic pulses in the solar photosphere and found their chromospheric counterparts, which reached the upper atmosphere with the local Alfvén speed. The origin of the impulsive velocity of spicules, synthetic profile of them, effect of radiative cooling and the thermal conduction are studied in the force-free atmosphere model, without coupling the turbulent convection (Singh et al., 2022; Srivastava et al., 2023). By introducing strong velocity pulse in the vertical direction (68 km/s) or transverse velocity (50–90 km/s) as the driver at chromosphere, cool coherent jet structures are formed.

1.5 Fibrils

They are believed to be the disk counterparts of spicules and are located over the active regions or the vicinity of solar plages (Suematsu et al., 1995). The roots of these jet structures are mostly located at the magnetic flux concentration of the network regions. In line core images of the several chromospheric channels (Ca II H & K, Hα), they are spotted as highly inclined, fine scale jet structures, covering the atmosphere densely (van Noort & Rouppe van der Voort, 2006; Pietarila et al., 2009; De Pontieu et al., 2007c) (Fig. 1.7). As fibrils are curved features, the length and height of the jet could be very different. Fibrils display

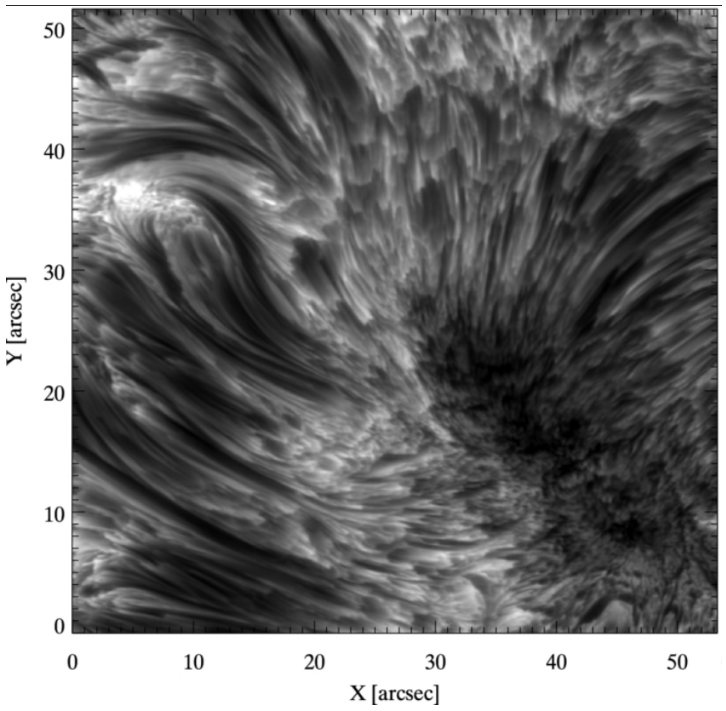

Fig. 1.7 Hα observation of fibrils at the vicinity of a pair of sunspots source:(Rouppe van der Voort & de la Cruz Rodríguez, 2013)

several features in the evolutionary phase analogous to spicules,e.g., rising and falling movement in the atmosphere (Hansteen et al., 2006), transverse oscillations due to Kink MHD modes (Mooroogen et al., 2017; Jafarzadeh et al., 2017), splitting, merging, and fading away from the field of view (Pietarila et al., 2009). Employing rMHD simulations with potential magnetic field in the background, it is reported that fibrils can originate from the impact of large amplitude perturbations of the global acoustic mode oscillation to the higher atmosphere and subsequently forming slow Magnetocacoustic shocks (Hansteen et al., 2006; De Pontieu et al., 2007c). In the presence of magnetic flux emergence from the convection zone of 3D rMHD model (Martínez-Sykora et al., 2009), synthetic fibrils show spatiotemporal properties similar to the observation counterparts. Regarding the horizontal or inclined morphology of fibrils, it is assumed that local magnetic field is the determining factor for such orientation of fibrils that connects plages with opposite polarity penumbra regions. In the lack of direct measurement of the chromospheric magnetic fields, De Pontieu et al. (2007c) investigated the same aspect by combining dark Hα fibril structure with the extrapolated potential magnetic fields. it is confirmed that most fibrils align with the inclined magnetic structures at the chromosphere, although there are some mismatches. Later, measurement of the chromospheric magnetic field using the Spectro-Polarimeter for Infrared and Optical Regions (Socas-Navarro et al., 2006) and and CRisp Imaging Spectro-Polarimeter (Scharmer, 2006) directly show fibrillar structures do

not always trace the magnetic field lines. It could be due to the time lag between the response of fibrils and highly dynamic magnetic fields or the effect of the decoupling of neutral atoms from the magnetic field in a partially ionized chromosphere.

1.6 Outline of the thesis

In Chapter 1, we first present an overview of the sun, its internal structure, and different layer of the outer atmosphere. This builds the foundation to investigate solar spicules. Next, we introduce spicules from the observational perspective and elaborately review the development of analytical and numerical models of it. Despite of immense advancement in the understanding of solar spicules, still, there are a series of open questions. The lack of a unified formation mechanism of spicules, difficulty in describing several dynamical features, lack of numerical models that can match observed ubiquity, and tall jet structures are a few of them. Hence it motivates us to delve into this conundrum. For the thesis, our aim is to understand the genesis and dynamics of the solar spicule forest in the light of simulations and laboratory experiments. In Chapter 2, we establish our numerical radiative Magnetohydrodynamics (rMHD) model, the primary tool to study the forest of solar spicules in this thesis. All governing equations, implementation of numerical schemes, and incorporated physical processes specific to the solar plasma are described comprehensively. In Chapter 3, we study the formation mechanism of the forest of jet components, starting from a simple forcing rMHD model. Then we gain illuminating insights by executing systematic analyses of laboratory fluid experiments. As a next step to the realistic solar model, we perform rMHD simulations with the convection process and show remarkable agreement between the simulated and observed properties. In Chapter 4, we focus on the morphology and intricate dynamics of spicules by combining a three-dimensional rMHD model and high-resolution solar observations. A new perspective on the three-dimensional structure of the spicule is portrayed. We describe the observed rapid spinning motion of spicules by invoking a novel mechanism. Estimation of mass and energy fluxes are provided in the realm of the mass budget of the solar wind and solar coronal heating, respectively. In Chapter 5, we compare our model with two publicly available rMHD models. We briefly discuss the similarities and differences among different data sets. In Chapter 6, we summarize all pivotal results gained from numerical studies, laboratory experiments, and solar observations. Finally, a future direction is drawn for further understanding of the broad impact of spicules on the solar wind.

2

Governing equations of radiative-Magnetohydrodynamics

2.1 Introduction

The simplest approach to investigate the solar atmospheric plasma and its interaction with electric and magnetic fields is the Magnetohydrodynamics (MHD) approximation, also known as the single-fluid approximation. The theory of MHD combines the equations of hydrodynamics with Maxwell's equations of electromagnetism. The validity of this formalism depends on two criteria of the system. The number of particles inside the Debye volume has to be much larger than unity and the time scale of consideration has to be greater than the inverse of the characteristic frequency of the system (plasma frequency, collisional frequency, and gyrofrequency). These criteria hold good in the internal region of the Sun, but at the outermost part of the atmosphere, at the corona, MHD approximation starts to fail due to a sharp fall in the particle density. Additionally, we need to consider the optically thick radiation field in the sub-photospheric domain and its transition to an optically thin regime at the higher atmosphere for setting up the solar atmospheric model. This formalism is known as the radiative-Magnetohydrodynamics (rMHD). For the past several decades, rMHD simulations

have been quite successful in understanding the solar surface convection (Nordlund, 1982; Stein & Nordlund, 1998; Vögler & Schüssler, 2003; Kitiashvili et al., 2011) along with various observed solar atmospheric features (Hansteen et al., 2006; Heggland et al., 2011; Martínez-Sykora et al., 2009; Kitiashvili et al., 2012; Bourdin et al., 2013; Chatterjee et al., 2016). In our rMHD model of the solar atmosphere, we self-consistently solve coupled mass, momentum, energy, and magnetic field evolution equations numerically for compressible plasma medium. To consider the radiation field, we solve the detailed radiative transfer equation simultaneously. For performing 2D and 3D numerical experiments, we opt for the Pencil Code (Pencil Code Collaboration et al., 2021) framework, a versatile, highly modular, higher-order finite difference platform, suitable for rMHD simulations. Incorporating several non-ideal physics e.g., viscous diffusion, Ohmic diffusion, shock dissipation, and non-adiabatic effects e.g., thermal conductivity, and radiative cooling, we aim to model the numerical setup realistically for comparing synthetic observables with state-of-the-art solar observations. The base of our 3D numerical domain is located at the sub-photospheric convection zone, 5 Mm depth from the photosphere, and the domain reaches 32 Mm height at the lower corona. We solve all dynamical equations following the non-conservative prescription and achieve the desired accuracy by considering higher-order finite difference schemes. Additionally, we can effectively attain large Reynolds number conditions or operate in highly turbulent regimes by using hyper-diffusivity to suppress numerical instabilities on the grid scale. All the building blocks of our model are described comprehensively in this chapter. After setting up, we thoroughly explore a wide range of parameter space in subsequent chapters to understand the overall behavior and coherency among different key components.

2.2 Mass and momentum conservation equation

We write the continuity equation for the logarithmic plasma density ($\ln\rho$) in the Lagrangian framework. For the numerical solution of all dynamical equations, we follow the Eulerian formalism. It is also noteworthy to mention that we evolve $\ln\rho$ instead of ρ to avoid any numerical artifact of encountering negative density.

$$\frac{D\ln\rho}{Dt} = -\boldsymbol{\nabla}\cdot\mathbf{U} + \boldsymbol{\nabla}\cdot(D\boldsymbol{\nabla}\ln\rho) + \boldsymbol{\nabla}\cdot\left(\zeta^{D}\boldsymbol{\nabla}\ln\rho\right) \tag{2.1}$$

Where $\mathbf{U}$ is the plasma flow field, $D/Dt = \partial/\partial t + \mathbf{U}\cdot\boldsymbol{\nabla}$ is the Lagrangian derivative, D is mass diffusion and ζ^{D} is mass diffusion at shock fronts. We will discuss the physics of shock diffusion elaborately in Section 2.10.

We solve the velocity field equation, incorporating the Lorentz force exerted by the magnetic

field (**B**), non-ideal momentum diffusion coefficient (ν), shock diffusion ($\zeta^{\rm shock}$), and the correction term ($\mathbf{F}^{\rm corr}$) due to semi-relativistic Boris correction (Chatterjee, 2020). We will describe the semi-relativistic Boris correction separately in Section 2.11. In the absence of magnetic fields (hydrodynamics), this equation becomes the Navier-Stokes equation. It is highly non-linear in nature under the large Reynolds number (ratio of inertial acceleration and viscous diffusion) limit. For the solar environment, the Reynold number is extremely large ($\approx 10^{12}$), owing to the enormous physical scales and expeditious motion of the plasma. By considering the Lorentz force for the magnetized plasma, the flow field retains non-linear characteristics and also transfers the same feature to other variables due to the coupling among them.

$$\rho\frac{D\mathbf{U}}{Dt} = -\boldsymbol{\nabla}p + \rho\mathbf{g} + \mathbf{j}\times\mathbf{B} + \boldsymbol{\nabla}\cdot(2\rho\nu\mathbf{S}) + \boldsymbol{\nabla}\left(\rho\zeta^{\rm shock}\boldsymbol{\nabla}\cdot\mathbf{U}\right) + \mathbf{F}^{\rm corr} \tag{2.2}$$

Where p is the gas pressure, $\mathbf{j}$ is the current density, $\mathbf{g}$ is the constant solar gravity, and $\mathbf{S}$ is the rate of strain tensor for compressible plasma medium.

$$\mathrm{S}_{ij} = \frac{1}{2}\left(\frac{\partial \mathrm{U}_i}{\partial x_j} + \frac{\partial \mathrm{U}_j}{\partial x_i} - \frac{2}{3}\delta_{ij}\left(\nabla.\mathbf{U}\right)\right) \tag{2.3}$$

For momentum diffusion, we only consider kinematic viscosity (ν) as the bulk viscosity is exactly zero for a plasma medium, made of monoatomic elements. We will describe the nature of these transport coefficients, and their dependency on plasma properties in Section 2.14. In our model, we neglect the contribution of the Coriolis force, since the Rossby number at the solar surface is expected to be very large.

2.3 Induction equation

Magnetic fields are an inherent part of the plasma medium, which evolves following the magnetic induction equation. The magnetic induction equation is derived by combining Faraday's law and Ohm's law of Electrodynamics. For our numerical setup, we solve magnetic vector potentials (**A**) following the non-ideal Induction equation instead of magnetic fields **B**, one of the unique properties of the Pencil Code. This approach ensures the divergence-free constraint or solenoidal nature of the magnetic field at the level of machine accuracy. This is a major computational advantage over the induction equation of magnetic fields where additional divergence cleaning schemes (Powell, 1994; Dedner et al., 2002) have to be employed to avoid

any numerical inconsistency.

$$\frac{\partial \mathbf{A}}{\partial t} = (\mathbf{U} \times \mathbf{B}) - \eta \mu_0 \mathbf{j} + \boldsymbol{\nabla} \Phi \tag{2.4}$$

The dynamics of the magnetic fields have two major components, (a) inductive term, $(\mathbf{U} \times \mathbf{B})$ (b) dissipation term due to Ohmic resistivity of the plasma, $\eta \mu_0 \mathbf{j}$. Here η is the Ohmic diffusion coefficient, μ_0 is the permeability of the free space. Apart from these two terms, Φ is the scaler function. It appears as part of the gauge invariance. We choose the Weyl gauge, where Φ becomes zero. Here we decompose the total magnetic field ($\mathbf{B}$) in the imposed, constant in space and time part ($\mathbf{B}_0$) and the non-uniform time varying part ($\boldsymbol{\nabla} \times \mathbf{A}$),

$$\mathbf{B} = \mathbf{B}_0 + \nabla \times \mathbf{A}$$

The imposed field structure represents the average solar poloidal magnetic fields, which dominate near the poles during the declining phase of the 11-year solar cycle. During the rising phase of the cycle, these open field structure regions, also known as coronal hole regions, can be observed anywhere over the solar disk. To reach the observed field strength (10–100 G) in different sets of models, we slowly increase the uniform imposed field from zero to final value ($B_{\rm imp}$) in 5–6 convective granulation time scales ($t_{\rm fin}$).

$$B_0 = B_{\rm imp} \sin^2(\pi t / 2 t_{\rm fin}) \tag{2.5}$$

Within this time scale, convective motion becomes stable as indicated by the saturated root mean square (rms) value of the velocity field at the photospheric height.

2.4 Energy conservation equation

As part of the energy conservation, we solve the temperature (T) evolution equation of the plasma blobs by taking into account various non-ideal heating (e.g., viscous, Ohmic, shock heating), radiative cooling ($\rho^2 \Lambda(T)$), turbulent conductivity (χ_t), thermal ($q_{\rm cond}$) and radiative conductivities ($q_{\rm rad}$). Viscous heating proportional to S^2 is the inherent part of the non-ideal fluids and plasma mediums, whereas the ohmic heating proportional to j^2 occurs due to the magnetized plasma flows. The explicit shock heating is also part of the viscous heating, but the amount of heating is modified by the large shock diffusion coefficient ($\zeta_{\rm shock}$) at the localized shock fronts. In this model, turbulent diffusion (χ_t) is present only in the convection zone region. Here $c_{\rm v}$ is the specific heat capacity for constant volume, γ is the adiabatic gas constant. We will describe radiative heat flux and cooling mechanism, conductive heat flux elaborately in

Section (2.9) and (2.13) respectively.

$$\begin{aligned}\rho c_v T \frac{D\ln T}{Dt} = &-\rho c_v T\,(\gamma-1)\,\boldsymbol{\nabla}\cdot\mathbf{U} + \boldsymbol{\nabla}\cdot(q_{\rm rad}+q_{\rm cond}) + \boldsymbol{\nabla}\cdot(\rho T \chi_t \boldsymbol{\nabla}\ln T)\\ &+ 2\rho\nu\mathbf{S}^2 + \rho\,\zeta_{\rm shock}(\boldsymbol{\nabla}\cdot\mathbf{U})^2 + \mu_0\eta\mathbf{j}^2 - \rho^2\Lambda(T)\end{aligned} \tag{2.6}$$

2.5 The equation of state

The equation of state defines a relation among thermodynamic variables (p,ρ,T) of the system. Here we consider constituent elements of the plasma as ionized, neutral hydrogen and fixed abundance of Helium atoms for the solar atmosphere. Using the Saha-Ionization equation, we compute the ionization fraction of hydrogen atoms under the Local Thermodynamic Equilibrium (LTE) approximation. Although in the chromospheric region (500 – 2000 km from the visible surface), this approximation does not hold well due to the stringent fall of plasma density compared to the solar photosphere. Therefore the mean free path becomes much larger compared to the temperature scale height and statistical equilibrium breaks down in the absence of matter–radiation coupling. Here we express the plasma pressure (p) as,

$$p = (n_{\rm HI} + n_{\rm HII} + n_{\rm e} + n_{\rm He}) k_{\rm B} T. \tag{2.7}$$

Where $n_{\rm HI}$, $n_{\rm HII}$, $n_{\rm e}$ and $n_{\rm He}$ are the number density of atomic hydrogen, ionized hydrogen, electrons and Helium atoms. $k_{\rm B}$ is the Boltzmann constant. Now it is convenient to normalize each number densities with the total number of atomic and ionized hydrogen counterpart, $n_{\rm Htot} \equiv n_{\rm HI} + n_{\rm HII}$, where we define $x_{\rm e} \equiv n_{\rm e}/n_{\rm Htot}$ and $x_{\rm He} \equiv n_{\rm He}/n_{\rm Htot}$. Now, we rewrite the equation 2.7

$$p = (1 + x_{\rm e} + x_{\rm He}) n_{\rm Htot} k_{\rm B} T. \tag{2.8}$$

Neglecting the mass contribution of electrons, plasma density (ρ) follows

$$\begin{aligned}\rho &\approx (n_{\rm HI} + n_{\rm HII} + 4n_{\rm He})\, m_u\\ &\approx (1 + 4x_{\rm He})\, n_{\rm Htot} m_u\end{aligned} \tag{2.9}$$

Where $m_u = 1$ amu. Now we substitute the density expression into the equation 2.5,

$$p = \frac{\rho R T}{\mu\,(T)} \tag{2.10}$$

Here R is the gas constant and μ is the effective atomic mass. In our model, we consider a constant relative abundance of Helium, $x_{\rm He} = 0.089$. The explicit temperature dependency in

the atomic mass arises due to the ionization fraction of hydrogen (x_e).

$$\mu(T) = \frac{1+4x_{\rm He}}{1+x_{\rm e}(T)+x_{\rm He}}$$

Now x_e is computed at each time step following the Saha Ionization equation,

$$\frac{x_{\rm e}^2}{1-x_{\rm e}} = q$$

where

$$q = \frac{\rho_{\rm e}}{\rho}\left(\frac{\chi_{\rm H}}{k_B T}\right)^{-3/2} \exp(-\chi_H/k_B T)$$

and

$$\rho_e = (1+4x_{\rm He})m_u\left(\frac{2\pi m_e \chi_{\rm H}}{h^2}\right)^{3/2}.$$

The solution of the quadratic equation in ionization fraction follows (Bhat & Brandenburg, 2016)

$$y_{\rm H} = \frac{2\sqrt{q}}{\sqrt{q}+\sqrt{4+q}}, \tag{2.11}$$

2.6 Numerical scheme

To achieve highly accurate solutions of the non-conservative form of governing equations, we use sixth-order accurate finite difference scheme for spatial differentiation on our uniform, static, cartesian numerical mesh.

$$f_i' = \frac{-f_{i-3}+9f_{i-2}-45f_{i-1}+45f_{i+1}-9f_{i+2}+f_{i+3}}{60\delta x} + \mathscr{O}(\delta x^6) \tag{2.12}$$

$$f_i'' = \frac{2f_{i-3}-27f_{i-2}+270f_{i-1}-490f_i+270f_{i+1}-27f_{i+2}+2f_{i+3}}{180\delta x^2} + \mathscr{O}(\delta x^6), \tag{2.13}$$

Here f_i, f_i, f_i'' are the functional value, first and second derivatives at the i th point of the mesh, respectively. δx is the grid resolution in the x direction and $\mathscr{O}$ represents the order of the error associated with the scheme. In order to determine the Lorentz force from the magnetic vector potential, physical diffusion terms, we need to compute second and higher-order differentiation operations frequently. Therefore to operate within sixth-order truncation error, we always use sixth-order accurate higher-order differentiation schemes.

2.7 Initial Condition

Here we describe the initial conditions for all primitive variables of our model.

- velocity components (U_x, U_y, U_z) : random velocity fluctuations from a Gaussian distribution to break symmetry in the horizontal directions
- magnetic vector potential components(A_x, A_y, A_z) : zero value. Therefore B_x, B_y, B_z are also zero.
- logarithmic temperature $(\ln T)$: temperature profile in the convective envelope is obtained from the model S (Christensen-Dalsgaard et al., 1996) and atmospheric variation is set from Vernazza et al. (1981) model (Fig. 2.1).
- logarithmic density $(\ln \rho)$: determined from the initial temperature profile and solving hydrostatic balance equation under Local Thermodynamic Equilibrium (LTE) approximation (Fig. 2.1).

To excite the solar convection, we perturb the system with the random velocity fields, which eventually break the initial hydrostatic equilibrium configuration and horizontal symmetry of the domain. With time, a convectively unstable region of the convection zone develops turbulent granular cells. Alongside, we gently increase the strength of the imposed magnetic field to the final value as described in Section 2.3.

2.8 Boundary Condition

Due to the sixth-order finite difference scheme, there is a total of six ghost zones at both ends of the physical boundary for every direction. Horizontal boundaries are set with periodic conditions for all physical variables, which means all fluxes that leave from one side of the boundary, again come back to the domain via the opposite side. Here we list the bottom and top boundary conditions for all primitive variables of our model.

Bottom boundary:

- U_x and U_y: Symmetric condition. Therefore $\partial U_x/\partial z$ and $\partial U_y/\partial z$ become zero at every horizontal grid point of the lower boundary.
- U_z: Anti-symmetric condition. U_z is set to zero. Therefore, no mass flux can enter or escape from the bottom boundary. Another known approach is to set an open boundary for inflows and outflows with a constraint of net zero mass flux (Fleck et al., 2022) over

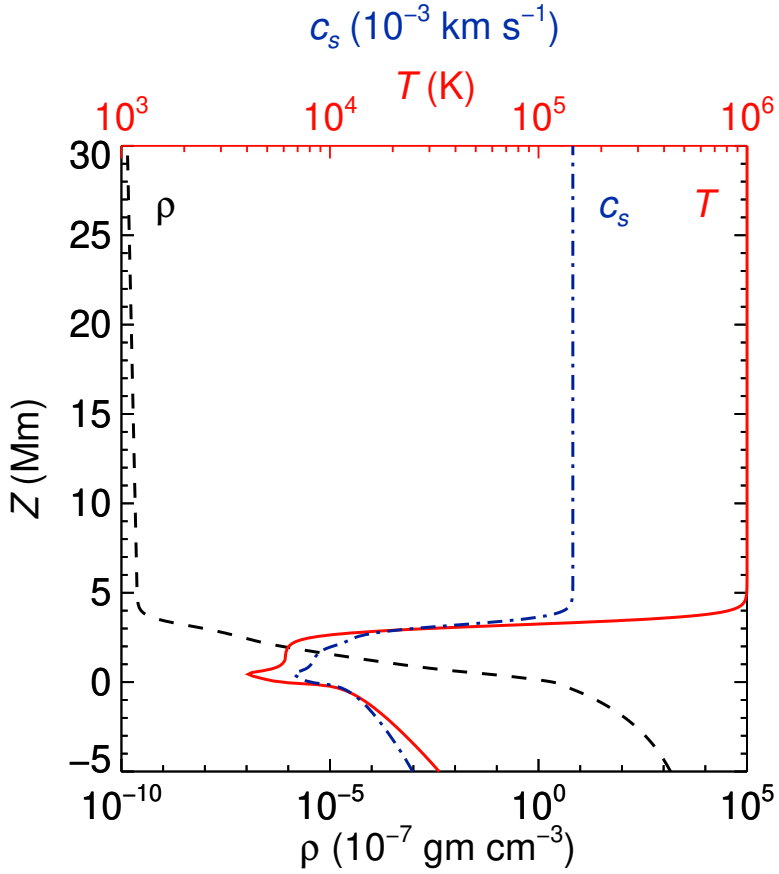

Fig. 2.1 Initial stratification profile of thermodynamics variables for constant solar gravity (274 cm s^{-2}): variation of (a) density (black-dash) (b) temperature (red-solid) (c) sound speed (blue-dash-dot) are shown as a function of height (z)

the horizontal extent. These conditions on all components of the velocity field fix a stress-free condition at the bottom boundary.

- A_x, A_y, A_z: symmetric boundary condition. Therefore B_x, B_y, B_z have non-zero values at the top boundary.
- $\ln T$: follows hydrostatic balance equation
- $\ln \rho$: follows hydrostatic balance equation

Top boundary:

- U_x and U_y: Anti symmetric condition. U_x and U_y become zero at the top boundary.
- U_z: Symmetric or mirror condition. It sets $\partial U_z/\partial z$ to zero, similar to an open boundary. A partially open boundary can also be set by opening the boundary for outgoing flows and closing for any incoming flows to the domain (Fleck et al., 2022).
- A_x, A_y, A_z: similar to bottom boundary. It is also possible to set only non-zero B_z components by setting symmetric, symmetric, and anti-symmetric conditions for A_x, A_y, A_z components respectively.
- $\ln T$: constant temperature at 10^6 K.
- $\ln \rho$: constant coronal density (1.33×10^{-17} gm cm^{-3})

Sponge layer as flux absorber: Flux reflection from finite boundaries (bottom or top) of the numerical model commonly creates unphysical artifacts and mitigates the validity of the overall result. The characteristic boundary condition (Engquist & Majda, 1977; Wu & Wang, 1987) is one solution with high accuracy and numerical stability compared to the extrapolated methods. But the implementation and time-dependent solution of such a scheme for all coupled equations are difficult and computationally expensive in the general scenario. In our models, we introduce a thick ($\approx$ 6 Mm) sponge layer at the top of the domain to absorb any incoming flux, which reduces the effect of reflection locally. For all sets of dynamic equations, a damping parameter ($\tau_{\rm damp}$) is multiplied to all source and sink terms, which smoothly becomes zero from the base of the sponge layer to the top of it. Therefore all physical quantities are almost dynamically frozen within it. At the base of the sponge layer, we hold the temperature around 1 million Kelvin (MK) in the slab to recreate a characteristic coronal condition. In the absence of strong nano flare heating (DC heating) or wave energy damping (AC heating) mechanisms, our models do not maintain the coronal plasma at the million-kelvin temperature self consistently.

Therefore this artificial slab helps to prevent collapsing of the atmosphere along with preventing reflection from the boundary.

2.9 Radiative transfer and cooling process

In our radiative-MHD models, the radiative transfer equation 2.14 is solved for frequency integrated specific intensity (I) at every timestep under the plane parallel, grey-atmosphere approximation. It has two components, (a) the emission term (S), which follows the frequency-integrated plank function, $(\sigma_{\rm SB}/\pi)T^4$, for the optically thick region. Here σ_{SB} is the Stefan-Boltzmann constant. For the transition of optically thick to thin environment, this source function goes to zero smoothly in our model at $z = 2.0$ Mm. (b) the absorption component (α) is determined by various physical processes among atoms and photons, e.g., bound-free transition, free-free transitions due to Bremsstrahlung absorption, H^- absorption, and electron conductivity. The bound-bound absorption process is neglected as it is negligible compared to the bound-free and free-free contribution. The bound-bound absorption process can be neglected due to their narrow band response across discrete frequencies of absorption.

$$\frac{dI}{d\tau} = S - I \tag{2.14}$$

where,

$$d\tau = \alpha dl = \kappa_{\rm tot}\rho dl$$

Here τ is the optical depth, α is the absorption coefficient, l is the distance along the ray propagation direction, $\kappa_{\rm tot}$ is the total opacity due to several absorption mechanisms as discussed above. The transfer equation is integrated along six rays which are both parallel and antiparallel to three mutually orthogonal axes. We ultimately compute the divergence of the radiative flux ($q_{\rm rad}$) as follows to add their contribution in the energy equation 3.16,

$$\nabla \cdot \mathbf{q}_{\rm rad} = -\kappa_{\rm tot}\rho \oint_{4\pi} (I - S)\mathrm{d}\Omega .$$

Here Ω represents the solid angle covering all ray directions. The numerical solution of the transfer equation is obtained following the long characteristic method (Heinemann et al., 2006). It is a non-diffusive approach where photons can propagate along straight lines ($\nabla \cdot \mathbf{q}_{\rm rad}$) Although in this method, efficient parallelism can only be implemented for a maximum of 26 ray directions in the 3D domain, where rays pass through exactly on grid points (Leenaarts, 2020). The other method to integrate the Radiative transfer equation is the short characteristic method, which is computationally less expensive. It requires higher-order interpolation to

compute fluxes at exact grid points and introduces diffusion in the photon path. A recent comparative study using both methods shed light on the scattering polarization signals of the solar atmosphere (de Vicente et al., 2021).

We model opacity functions with frequency-integrated Rosseland mean instead of the tabulated opacity tables, e.g., OPAL table (Iglesias & Rogers, 1996). Here, we consider hydrogen mass fraction, $X = 0.7381$ and metal mass fraction, $Z = 0.0134$ for the solar case. Bound-free and free-free opacities are represented in Kramers power law format,

$$\kappa_{\mathrm{bf+ff}} \sim 4 \times 10^{25} Z(X+1)\rho T^{-7/2} \mathrm{cm}^2 \mathrm{g}^{-1},$$

The H^- opacity is expressed as,

$$\kappa_{\mathrm{H^-}} \sim 1.25 \times 10^{-29} Z \rho^{1/2} T^9 \mathrm{cm}^2 \mathrm{g}^{-1}.$$

The conductive opacity (κ_{c}) for the electron diffusion is estimated from the Fick's law of diffusion (Hansen & Kawaler, 1994), which follows

$$\kappa_{\mathrm{c}} = 2.6 \times 10^{-7} \frac{T^2}{\rho} \mathrm{cm}^2 \mathrm{g}^{-1}.$$

The total opacity follows a relation similar to the effective resistivity of a parallel circuit. Therefore the smaller opacity profile determines the total profile.

$$\frac{1}{\kappa_{\mathrm{tot}}} = \frac{1}{\kappa_{\mathrm{bf+ff}}} + \frac{1}{\kappa_{\mathrm{H^-}}} + \frac{1}{\kappa_c},$$

We compare the horizontally averaged profile of each component of opacity with the total opacity (κ_{tot}) as a function of height (Fig. 2.2). Near the solar photosphere, the absorption of H^- atoms governs the behavior of total opacity. This is because of the low electron affinity of the H^- atom, 0.75 ev. From the Blackbody radiation of the Sun, which has a maximum energy density at 500 nm (2.48 ev), there are enough photons with sufficient energy to provide energy to disassociate H^- to neutral hydrogen atoms and free electrons. Therefore the total number of particles increases or the photon mean free path $(1/\kappa_{\mathrm{tot}}\rho)$ decreases due to scattering with atoms. This makes the near sub-photospheric region opaque. The conductive opacity value is very large compared to the other components in the atmosphere, making it irrelevant to the total profile. In the chromosphere, the effective opacity is mostly sensitive to the bound–free and free–free opacity and it falls rapidly with increasing height.

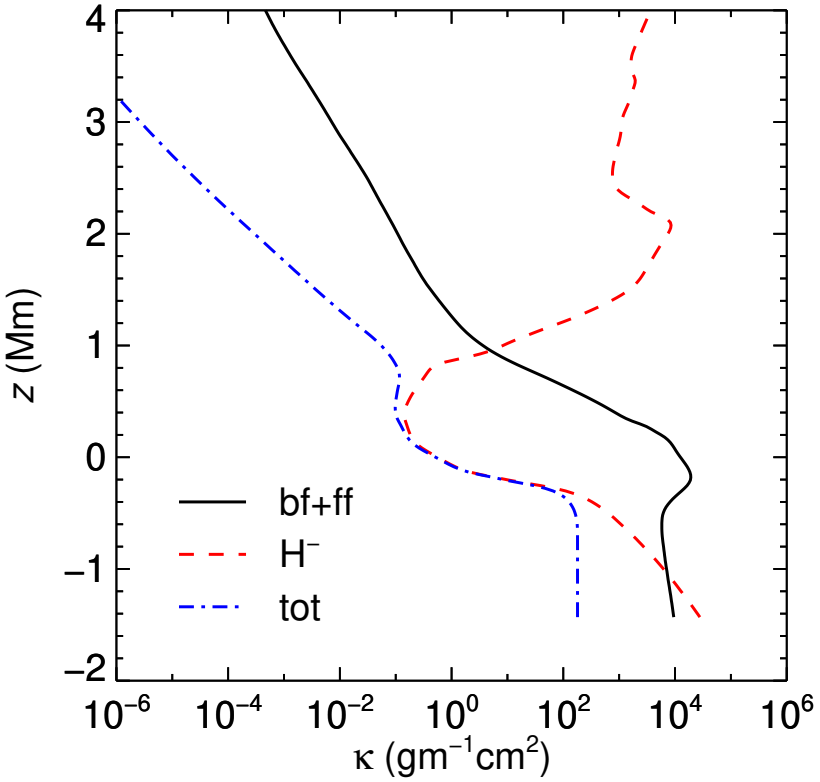

Fig. 2.2 Variation of horizontally averaged opacity profile κ of the solar atmosphere with height (z): (i) opacity for bound-free and free-free emission (black-solid) (ii) H^- ions (red dashed) (iii) effective total opacity, $\kappa_{\rm tot}$ (blue-dot-dashed)

2.9.1 Radiative cooling in solar corona

The solar corona is an optically thin region for almost the entire spectrum of electromagnetic radiation except for the radio frequency range. It means the bound-bound and bound-free transitions are less probable due to rare interactions between the plasma medium and photons. However, the interactions among ions, electrons, and atoms are frequent by the collisional excitation process followed by spontaneous de-excitations. Through this mechanism, photons can escape gaining energy from the thermal reservoir of plasma and contribute to the radiative cooling process (Carlsson & Leenaarts, 2012; Leenaarts, 2020). In the coronal condition, emitted photos are not absorbed further and the probability of collisional de-excitation is small enough. This is referred to as coronal approximation. We include the radiative cooling process to our energy equation 3.16, $Q_{\rm thin} = y_{\rm H} n_{\rm H}^2 \Lambda(T)$. $y_{\rm H}$ is the ionization fraction of Hydrogen, and $n_{\rm H}$ is the number density of the element Hydrogen. $\Lambda(T)$ is the radiative loss function of

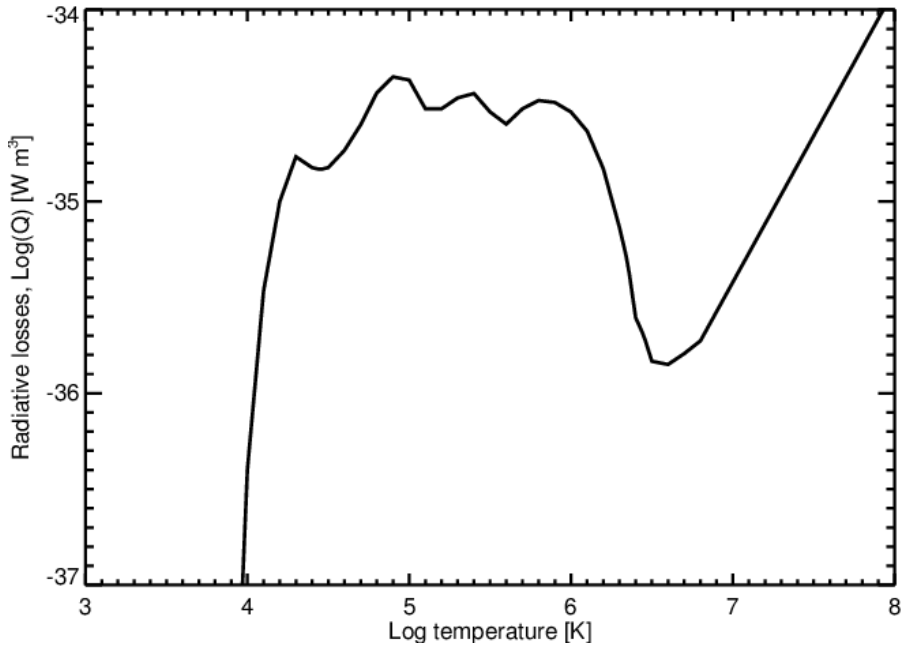

Fig. 2.3 Behaviour of the radiative loss function for the optically thin medium with the plasma temperature. Image credit to van Wettum (2013)

temperature in units of W m^3. The variation of $\Lambda(T)$ is available in tabulated form, computed from the atomic data set (Cook et al., 1989). The loss function considers statistical equilibrium approximation where emission from the higher (j) to lower (i) energy state is defined in terms of Einstein coefficient (A_{ji}) and the population density as,

$$\begin{aligned} Q_{ij} &= h\nu_{ij} \frac{A_{ji}}{n_e} \frac{n_{j,m}}{n_m} \frac{n_m}{n_X} \frac{n_X}{n_{\rm H}} n_{\rm e} n_{\rm H} \\ &\approx G(n_{\rm e}, T) n_{\rm e} n_{\rm H} \end{aligned} \tag{2.15}$$

Here we define contribution function $G(n_{\rm e}, T)$, in terms of the fraction of ions in ionization state m of energy level j ($n_{j,m}/n_m$), the fraction of element X in ionization state m (n_m/n_X), and the relative abundance of element X compared to hydrogen atoms ($n_X/n_{\rm H}$). Finally, the radiative cooling function is computed by summing Q_{ij} over energy levels of all ionization states of every constituent element. Although the contribution function weakly depends on the electron density of the plasma medium (Landi & Landini, 1999). Therefore in our numerical model, we only consider the temperature variation of the radiative loss function (Fig. 2.3). Here we take into account the coronal abundance of solar elements (e.g., C, O, Si, Fe, Mg, S), with different stages of ionization (Meyer, 1985). Compared to their photospheric counterparts, they are a minimum of 3-4 orders of magnitude depleted, although the radiative loss is dominated by a factor of 3–4 times (Feldman et al., 1992; Grevesse & Sauval, 1998) in between the temperature

range of 2×10^5 K to 10^7 K. Fe plays a vital role in the large radiative losses at the higher side of plasma temperature (2×10^5 – 10^6 K), whereas below (2×10^5 K), C and O are responsible for strong radiative cooling of solar plasma. The radiation escaping outward contributes to the cooling of the solar plasma. At the same time, an equal part of the optically thin radiative flux is emitted radially inward and is absorbed in the chromosphere. There it contributes to radiative heating instead of cooling (Carlsson & Leenaarts, 2012). To calculate this heating at every time step in a 3-dimensional simulation is non-trivial, therefore we approximate $Q_{\rm thin} \rightarrow 0$ smoothly for $T > 30000$ K. A similar hard limit on temperature (20,000 K) is also used in the MURaM code (Rempel, 2016) to exclude the radiative cooling contribution from the optically thick region. In the BIFROST code (Gudiksen et al., 2011), they use a smooth multiplication factor $\exp(-p/p_0)$ as a function of plasma pressure (p) with height and its typical chromospheric value (p_0).

2.10 Shock diffusivity

Shocks are one of the ubiquitous features in solar observations where plasma flows faster than the characteristic speed of the medium, e.g., sound or Alfvén speed. It can emanate from the intergranular boundary of two horizontally diverging granules, MHD waves in the highly stratified atmosphere, and different exploding transient events, e.g., coronal mass ejections and magnetic reconnection regions. We detect shock fronts in our numerical models with the help of their intrinsic property which is strong density compression due to converging flows. This approach was successfully tested and used by several authors Lehmann et al. (2016); Lyra et al. (2017); Wang et al. (2021) across different domains of Astrophysics. In collisional fluids, the thickness of the shock front is of the order of mean free path (Zel'dovich & Raizer, 1967) while it becomes even several orders smaller for collisionless plasma (Petschek, 1958; Buneman, 1964). Under the MHD approximation, resolving such a small scale is impossible. Extensive studies on shocks demonstrate that the thickness of the front depends on the viscous diffusion (Orta et al., 2003). By introducing enhanced diffusion locally ($\zeta_{\rm shock}$) with explicit shock viscosity, the thickness of the front increases (Ballai et al., 2007). Therefore it becomes possible to locate them within the MHD approximation. This shock viscosity acts only in the localized region of highly compressed flows denoted by positive values of $-(\boldsymbol{\nabla} \cdot \mathbf{U})$. For the numerical treatment, we first compute the running maximum value of $[(-\boldsymbol{\nabla} \cdot \mathbf{U})_+]$ over three neighboring grid points along each spatial dimension and then a running mean $\langle \mathrm{Max}_3 \, [(-\boldsymbol{\nabla} \cdot \mathbf{U})_+] \rangle$ over the same points for smoothing the profile. Now the shock diffusion,

ζ_{shock} is defined as

$$\zeta_{\text{shock}} = c_{\text{shock}} \langle \text{Max}_3 \left[(-\boldsymbol{\nabla} \cdot \mathbf{U})_+ \right] \rangle \min \left(\text{dx}^2, \text{dy}^2, \text{dz}^2 \right) \tag{2.16}$$

where c_{shock} is the dimensionless diffusion strength parameter, dx, dy, and dz are grid resolutions in each direction. Besides increasing the front thickness, explicit shock viscosity reduces the numerical oscillations across the front. We consider this increased diffusion due to shocks in the mass, momentum, induction and energy equations to maintain self-consistency among numerical solutions.

2.11 Semirelativistic Boris correction

The study of the stellar interior is well suited to a non-relativistic MHD framework, where the displacement current (j_d) in Ampére's Law is ignored as the speed of the plasma parcels remains negligible than the speed of light. But there are low-density coronal regions above strong magnetic structures, where the Alfvén speed can reach the relativistic limit (Chatterjee & Fan, 2013; Rempel, 2016). With such a propagation speed, displacement current can not be neglected anymore. Therefore we consider the displacement current contribution to the Lorentz force but treat the other terms of the velocity field and coupled equations non-relativistically, therefore known as Semi-relativistic Boris correction.

$$\mathbf{j} \times \mathbf{B} = \frac{1}{\mu_0} (\boldsymbol{\nabla} \times \mathbf{B}) \times \mathbf{B} - \frac{1}{\mu_0 c^2} \frac{\partial \mathbf{E}}{\partial t} \times \mathbf{B} \tag{2.17}$$

As the displacement current is proportional to the $\partial \mathbf{E}/\partial t$, the equilibrium solution of the MHD equation does not alter due to this approximation. Here we adapt artificially reducing the speed of light method and avoid extremely small Alfvén wave crossing time steps, one of the major bottlenecks of performing long-term evolution of solar coronal models. The numerical implementation of this correction term is followed from the primitive variable approach for the non-conservative velocity field equation (Gombosi et al., 2002). Now combining Faraday's law and Induction equation, we get additional terms of the acceleration equation as,

$$\frac{1}{\mu_0 c^2} \mathbf{B} \times \frac{\partial \mathbf{E}}{\partial t} = \rho \left(-\frac{v_A^2}{c^2} \mathbf{I} + \frac{v_A^2}{c^2} \mathbf{bb} \right) \cdot \frac{\partial \mathbf{U}}{\partial t} + \left[\frac{(\boldsymbol{\nabla} \times \mathbf{E}) \times \mathbf{U}}{\mu_0 \rho c^2} \right] \times \mathbf{B} \tag{2.18}$$

Here $\mathbf{I}$ is the identity matrix,v_A is the Alfvén speed, and $\mathbf{b}$ are components of the unit vector along the magnetic field. Now after adding the modified Lorentz force, the dynamics of the

velocity field equation is determined by

$$\left[\mathbf{I}+\frac{v_A^2}{c^2}\left(\mathbf{I}-\mathbf{bb}\right)\right]\cdot\frac{\partial \mathbf{U}}{\partial t}=-\left(\mathbf{U}\cdot\boldsymbol{\nabla}\right)\mathbf{U}-\frac{\boldsymbol{\nabla} p}{\rho}+\mathbf{g}+\left[\frac{\left(\boldsymbol{\nabla}\times\mathbf{B}\right)}{\mu_0\rho}+\frac{\left(\boldsymbol{\nabla}\times\mathbf{E}\right)\times\mathbf{U}}{\mu_0\rho c^2}\right]\times\mathbf{B}. \tag{2.19}$$

This new matrix on the left-hand side of equation 2.19 introduces enhanced inertia in the plasma motion perpendicular to the magnetic field, albeit the propagation along the magnetic field is unchanged. Now we compare two terms within the square braces of the right-hand side and find their ratio of the order of $(|\mathbf{U}|/c)^2$. It can be safely dropped as it is the second-order term in $|\mathbf{U}|/c$.

$$\frac{|(\boldsymbol{\nabla}\times\mathbf{E})\times\mathbf{U}|}{c^2|\boldsymbol{\nabla}\times\mathbf{B}|}\sim\frac{|\mathbf{U}|^2}{c^2}\ll 1. \tag{2.20}$$

Now we invert the inertia matrix and present it as the sum of the identity matrix and additional term due to the correction. Here, we define $\beta_A^2=v_A^2/c^2$

$$\begin{aligned}\left[\mathbf{I}+\beta_A^2\left(\mathbf{I}-\mathbf{bb}\right)\right]^{-1}=&\frac{1}{1+\beta_A^2}\left[\mathbf{I}+\frac{\beta_A^2}{1+\beta_A^2}\mathbf{bb}\right]\\ =&\mathbf{I}-\frac{\beta_A^2}{1+\beta_A^2}\left[\mathbf{I}-\frac{\mathbf{bb}}{1+\beta_A^2}\right].\end{aligned} \tag{2.21}$$

This identity matrix restores the standard source terms of the acceleration equation in the absence of the correction. Therefore the sum of these extra sources (F^{corr}) in the acceleration equation becomes

$$\mathbf{F}^{\text{corr}}=\frac{\beta_A^2}{1+\beta_A^2}\left[\mathbf{I}-\frac{\mathbf{bb}}{1+\beta_A^2}\right]\left[\mathbf{U}\cdot\boldsymbol{\nabla}\mathbf{U}+\frac{\boldsymbol{\nabla} p}{\rho}-\mathbf{g}-\frac{\left(\boldsymbol{\nabla}\times\mathbf{B}\right)\times\mathbf{B}}{\mu_0\rho}\right]. \tag{2.22}$$

In the limit of $v_A << c$, applicable to the solar convective or photospheric regions, F_{corr} becomes zero and we preserve the original form the acceleration equation without the semi-relativistic effect. If in certain cases, $v_A < c$ or numerically $v_A \geq c$, higher up in the solar corona, the correction term becomes large to contribute to the plasma motion. The characteristic speed of the Alfvén wave modifies non-trivially in such case, but we set it as $v_A/\sqrt{1+\beta_A^2}$. Now if we artificially reduce the speed of light in the solar atmosphere to $c=\max[c_s, 5|U|_{\max}]$, where c_s is the sound speed. In that case, β_A becomes larger than unity and the correction term ($\mathbf{F}^{\text{corr}}$) starts to affect the plasma motion. With reduced light speed, the effective Alfvén speed becomes smaller than the original speed. Therefore it allows us to take large time steps to integrate the equation of motion. We find stable solutions for our 2D and 3D models With this approximation. Another crucial characteristic of this method is the less diffusion nature. Hence relatively coarse grid models can give stable solutions (Tóth et al., 2011).

2.12 Hyperdiffusion as numerical filter

Hyperdiffusion is an artificial type of diffusion that acts at the smallest grid scales to suppress numerical instabilities. We include hyperdiffusion coefficients along with explicit physical diffusion in all dynamical equations of our model. In general, we can express the continuity equation for any physical variable ψ with the current density ($\mathbf{J}$) as

$$\frac{\partial \psi}{\partial t} + \boldsymbol{\nabla} \cdot \mathbf{J} = 0 \tag{2.23}$$

From generalized Fick's diffusion equation, n-th order current density due to 2n-th order isotropic diffusion is defined as

$$\mathbf{J}^{(\mathrm{n})} = (-1)^{\mathrm{n}} D^{(\mathrm{n})} \boldsymbol{\nabla}^{2\mathrm{n}-1} \psi, \tag{2.24}$$

where $D^{(\mathrm{n})}$ is the strength of the 2n th order diffusion coefficient. If we choose n$=$ 1, we get the ordinary diffusion equation, which has a second-order spatial derivative. For n=3, the sixth-order hyperdiffusion equation becomes,

$$\frac{\partial \psi}{\partial t} = D^{(3)} \nabla^6 \psi \tag{2.25}$$

where the rate of change of ψ becomes proportional to ∇^6 in the physical space or k^6 in the Fourier space. Therefore, the hyperdiffusion becomes most effective at larger k or in the smallest physical scales to smear out any sharp gradients in the physical quantities. Theoretically, one can use any arbitrarily higher-order hyperdiffusion, but in practical implementation, the stencil size of the numerical domain sets the upper limit. In the manual of the Pencil Code (Brandenburg et al., 2020), there is a comparative analysis of the spectrum for the sixth-order hyperdiffusion with second-order physical diffusion.

2.12.1 Linear and Angular momentum conservative schemes

When we apply hyperdiffusion in the velocity field evolution equation, we need to confirm that the conservation of linear and angular momentum is still intact. The viscous acceleration or deceleration (f_{visc}) of the plasma depends on the rate of strain tensor (S) by the following relation,

$$f_{\mathrm{visc}} = \rho^{-1} \boldsymbol{\nabla} \cdot (2\rho\nu\mathbf{S}). \tag{2.26}$$

For the hyperdiffusion counterpart, we can write a general high-order version of the rate-of-strain tensor ($\mathbf{S}^{(\mathrm{n})}$) which explicitly conserves both linear and angular momentum (Lyra et al.,

2017). Here $\nu_{\rm n}$ is the 2n th order hyperdiffusion coefficient.

$$f_{\rm visc}^{\rm (hyper)} = \rho^{-1}\boldsymbol{\nabla}\cdot\left(2\rho\nu_{\rm n}\mathbf{S}^{\rm (n)}\right) \tag{2.27}$$

Where the n$^{\rm th}$-order rate-of-strain tensor ($\mathbf{S}^{\rm (n)}$) takes the form as

$$\mathbf{S}^{\rm (n)} = (-\nabla^2)^{\rm n-1}\mathbf{S}. \tag{2.28}$$

For the n= 3, it becomes

$$\mathrm{S}_{ij}^{(3)} = \frac{1}{2}\left(\frac{\partial^5 \mathrm{U}_j}{\partial x_i^5} + \frac{\partial^4}{\partial x_i^4}\left(\frac{\partial \mathrm{U}_i}{\partial x_j}\right) - \frac{1}{3}\frac{\partial^4}{\partial x_i^4}\left(\boldsymbol{\nabla}\cdot\mathbf{U}\right)\right). \tag{2.29}$$

For the constant sixth order hyperdiffusive kinematic viscosity (ν_3), hyperdiffusion acceleration follows,

$$\mathbf{f}_{\rm visc}^{\rm (hyper)} = \nu_3\left(\nabla^6\mathbf{U} + \frac{1}{3}\nabla^4(\boldsymbol{\nabla}(\boldsymbol{\nabla}\cdot\mathbf{U})) + 2\mathbf{S}^{(3)}\cdot\boldsymbol{\nabla}\ln\rho.\right) \tag{2.30}$$

where

$$\nabla^6 \equiv \nabla^2\left(\nabla^2\left(\nabla^2\right)\right)$$

In the Cartesian coordinate, we compute numerically expensive cross-derivative terms of the ∇^6 operator and consider the symmetric component of $\mathrm{S}_{ij}^{(3)}$ to conserve both the linear and angular momentum of the system.

$$\begin{aligned}\nabla^6 =& \frac{\partial^6}{\partial x^6} + \frac{\partial^6}{\partial y^6} + \frac{\partial^6}{\partial z^6} + 3\left(\frac{\partial^4}{\partial x^4}\frac{\partial^2}{\partial y^2} + \frac{\partial^4}{\partial x^4}\frac{\partial^2}{\partial z^2} + \frac{\partial^4}{\partial y^4}\frac{\partial^2}{\partial x^2} + \frac{\partial^4}{\partial y^4}\frac{\partial^2}{\partial z^2} + \frac{\partial^4}{\partial z^4}\frac{\partial^2}{\partial x^2} + \frac{\partial^4}{\partial z^4}\frac{\partial^2}{\partial y^2}\right)\\ &+ 6\frac{\partial^2}{\partial x^2}\frac{\partial^2}{\partial y^2}\frac{\partial^2}{\partial z^2}\end{aligned} \tag{2.31}$$

For the magnetic induction equation, the same expensive scheme is used to compute $\nabla^6 A$ for better approximation in magnetic flux conservation.

2.13 Anisotropic thermal conductivity

Transient energetic events, e.g., Solar flares and associated CMEs, magnetic reconnections, dump enormous magnetic energies into the solar corona. A part of such energy is redistributed in the plasma as internal energy via an efficient thermal conduction process. It is the key mechanism through which solar corona lose energy and the chromospheric heating is sustained.

Thermal conduction in the atmosphere is highly structured due to the presence of magnetic fields. In a plasma environment, thermal heat flux predominately propagates along the magnetic fields due to large thermal conduction compared to the perpendicular direction, where heat flux can reach only up to the scale of the Larmor radius (Braginskii, 1965; Priest, 2014). The strength of the thermal conduction parallel to the magnetic field ($k_{\parallel}$) is modeled by Spitzer (Spitzer, 1962), which is proportional to the $T^{5/2}$.

$$k_{\parallel} = k_0 T^{5/2} \left[\frac{\text{erg}}{\text{cm} \cdot \text{s} \cdot \text{K}^{7/2}} \right] \tag{2.32}$$

Here $k_0 = 10^{-6}$. The ratio of the perpendicular ($k_{\perp}$) to parallel ($k_{\parallel}$) component of the Spitzer conductivity with respect to the magnetic field follows (Priest, 2014),

$$\frac{k_{\perp}}{k_{\parallel}} = 2 \times 10^{-45} \frac{n^2}{\text{B}^2 T^3} \tag{2.33}$$

Where number density (n), magnetic field (B), and temperature (T) are represented in cgs unit. The typical plasma temperature in the solar corona is as high as 10^6 K, and the number density in the tenuous plasma medium is as low as 10^8 cm^{-3}. Therefore the thermal diffusion parallel to the magnetic field becomes enormous in such coronal conditions. Accordingly, the associated diffusion time scale, which is inversely proportional to the coefficient, becomes extremely small there. To avoid the constraint of tiny thermal diffusion time scale on the overall dynamics of the system, there are several formalisms, e.g., time sub-stepping, implicit treatment of the conduction, and hyperbolic transport equation. Here we adopt the hyperbolic or non-fickian transport equation for heat flux, which is used in several solar coronal models (Rempel, 2016; Fan, 2017; Chatterjee, 2020; Warnecke & Bingert, 2020). To demonstrate the hyperbolic nature of the transport equation (Rempel, 2016) compared to the standard parabolic diffusion equation, we describe a one-dimensional model with a constant diffusion k' and a free parameter τ.

$$\tau \frac{\partial q}{\partial t} + q = -k' \frac{\partial T}{\partial x} \tag{2.34}$$

and

$$\frac{\partial T}{\partial t} = -\frac{\partial q}{\partial x} \tag{2.35}$$

For $\tau = 0$ condition, we recover the standard parabolic heat diffusion equation. With non zero τ, we take the time derivative of the equation 2.35, use equation 2.34 for substitution and find

the hyperbolic transport equation,

$$\frac{\partial^2 T}{\partial t^2} + \frac{1}{\tau}\frac{\partial T}{\partial t} - c^2 \frac{\partial^2 T}{\partial x^2} = 0 \tag{2.36}$$

where

$$c = \sqrt{\frac{k'}{\tau}}$$

Here c represents the characteristic speed of the heat wave equation, τ sets the time within which the hyperbolic solution matches with the parabolic solution. We fix the τ value to 0.01s in our model. The other intrinsic advantage of using hyperbolic formalism is the linear dependency of time steps with grid spacing ($dt_{\text{cond}} = dx\sqrt{\tau}/\sqrt{k'}$) against the quadratic dependency for the Spitzer heat conduction ($dt_{\text{Spitzer}} = dx^2/k'$).
Now we rewrite the heat flux evolution equation 2.34 for the multi-dimensional case with considering hyperdiffusion corrections,

$$\frac{\partial q_{\text{cond}}}{\partial t} = -\frac{q_{\text{cond}} - q_{\text{sp}}}{\tau} + \beta(\mathrm{d}r\cdot\boldsymbol{\nabla})^6 q_{\text{cond}}, \tag{2.37}$$

where,

$$q_{\text{sp}} = k_0 T^{5/2}\hat{b}(\hat{b}\cdot\boldsymbol{\nabla}T),$$

We explicitly solve equation 2.37 for every timestep along with other coupled equations of MHD. Here q_{cond} is the conductive flux and q_{sp} is the Spitzer heat flux, $\hat{b}$ is the unit vector along the magnetic field, β is the hyperdiffusion parameter that is fixed at 1s^{-1}, dr=[dx, dy, dz]. We also limit the Spitzer diffusion speed (u_{sp}) by the $f_{\text{sp}} = 0.1$ factor of the actual speed of light (c_0) for locations,

$$u_{\text{sp}} = \frac{k_0 T^{5/2}}{\rho c_V \delta x} > f_{\text{sp}} c_0,$$

Where δx is the largest grid spacing of the numerical mesh. Adapting this hyperbolic transport equation, we can safely take 100 times larger temporal resolution compared to the standard parabolic heat transfer approach.

2.14 Transport coefficients

We take into account several transport coefficients, e.g., kinematic viscosity, thermal conductivity and Ohmic resistivity in our non-ideal rMHD models. Hence we expect better agreement of simulation results with observations. Each of the coefficients sets its own physics-specific length and time scales, which controls momentum, thermal and magnetic flux transfer rate

locally. Viscosity and resistivity are also responsible for the plasma heating process by converting the kinetic and magnetic energy to the thermal energy of the plasma medium.
In the equation of mass continuity, there is no explicit mass diffusion parameter. But in the numerical modeling, we use explicit mass diffusivity(n = 1) following Fick's diffusion (equation 2.23) law for better control of the numerical stability.
For the evolution of velocity fields, kinematic viscosity is the transport coefficient that links the rate of strain of plasma with the viscous stress. In general, transport coefficients can be estimated by taking care of collisional physics (Spitzer, 1962; Leake et al., 2013; Ni et al., 2020) among the constituent elements of the plasma, e.g., electrons, ions, and neutrals. In the context of MHD, we only consider contributions from electrons and ions and therefore define the collisional frequency among them as $\omega_{\rm ei}$,

$$\omega_{\rm ei} = \frac{4}{3} n_i \sigma_{\rm ei} \sqrt{\frac{2K_{\rm B}T_{\rm ei}}{\pi m_{\rm ei}}} \tag{2.38}$$

where $\sigma_{\rm ei}$ is the collisional-cross section between electron and ion, $\sigma_{\rm ei} = \ln\Lambda \pi r_d^2$, $\ln\Lambda$ is Coulomb logarithm, $r_d = e^2/(4\pi\varepsilon_0 K_B T_e)$, effective mass, $m_{\rm ei} = m_{\rm e} m_{\rm n}/(m_{\rm e} + m_{\rm n})$ and effective plasma temperature $T_{\rm ei} = (T_{\rm e} + T_{\rm i})/2$. Under MHD approximation, the number density of electrons ($n_{\rm e}$) and ions ($n_{\rm i}$) follows $n_{\rm e} = n_{\rm i} = n$ due to charge neutrality condition and temperature of electron ($T_{\rm e}$), ions ($T_{\rm e}$) have the common temperature (T), $T_{\rm e} = T_{\rm i} = T$. The total kinematic viscosity (ν) for electrons and ions follows

$$\nu = \nu_{\rm e} + \nu_{\rm i}$$

where

$$\nu_{\rm i} = n_{\rm i} K_B T_{\rm i}/\omega_{\rm ii}$$

Hence the kinematic viscosity increases with plasma temperature as $T^{5/2}$. Similarly, we write the relationship between the collisional frequency and the magnetic diffusivity (η) as

$$\eta = \frac{m_e \omega_{ei}}{e^2 n_e \mu_0}$$

So the magnetic diffusivity decreases with temperature profile as $T^{(-3/2)}$. To reduce the computational overhead, we opt for only a vertical variation (z) of these coefficients instead of a function of highly inhomogeneous and anisotropic temperatures. We model them as a single-step function considering the sharp rise in temperature above the solar transition region.

$$\nu/\nu_0 = 1 + f(1 + \tanh\{(z - z_1)/w\}) \tag{2.39}$$

with, $f = 3 \times 10^2$, $z_1 = 1.5$ Mm, $w = 0.2$ Mm, $\nu_0 = 2.5 \times 10^7$ cm^2 s^{-1}. Here z_1 denotes approximately the height of the sharp temperature increment so for the kinematic viscosity. Although theoretically, magnetic diffusion decreases as the temperature increases in the solar atmosphere, there could be numerical instability during implementation in the model. This is because reaching an extremely large magnetic Reynolds number (R_m), 10^{11}, requires a highly resolved numerical mesh. Therefore, we take a similar step function profile (equation 2.39) for magnetic diffusion but with one magnitude small variation in f, compared to the kinematic viscosity. With this approximation, we still expect the physics of the solar corona to be intact as the magnetic Prandtl ($P_m = \nu/\eta$) no is large (≈ 20) compared to the unity value, due to large kinematic viscosity. In the mixing length theory of solar convection, the turbulent viscosity profile is modeled similarly to step functions (Chatterjee et al., 2004). Although the transport coefficients we have discussed so far, are the molecular diffusion coefficients. They have much smaller values ($\approx 10^7$ cm^{2}s^{-1}) compared to turbulent diffusion ($\approx 10^{12}$ cm^{2}s^{-1}) near the solar photosphere

2.15 Characteristic non-dimensional numbers

In the domain of hydrodynamics and magnetohydrodynamics, we study a set of equations that are intricate enough to understand mainly due to the coupling amongst them and their inherent non-linear nature. One of the easiest ways to qualitatively predict the nature of the solution is by comparing different source terms or the non-dimensional numbers associated with the governing equations. In the Astrophysical context, we estimate these parameters simply by large-scale observational evidence, without considering the complicated microphysics. Even with state-of-the-art computational resources, reaching all estimated numbers is impossible due to the inherent multiscale nature of the problem. However, synthetic outputs from numerical models are quite successful in describing high-resolution solar observations. Here is a set of non-dimensional numbers from our model. For all estimations, we use grid resolution (δx) as the characteristic length scale. Therefore all values are the most conservative ones from our setup.

- Reynolds no (R): ratio of inertial acceleration term and viscous acceleration/deceleration term ($|\mathbf{U}|\delta x/(\nu + k^4\nu^3)$). Here we also consider the hyperviscosity effect (ν^3) for a conservative estimation. It ranges from 500 at the convection zone (4 Mm depth from the photosphere) to 200 in the corona (20 Mm height from the photosphere).

- Prandtl no (Pr): The ratio of the momentum diffusion to the thermal diffusion coefficient. In terms of the time scale, it is the ratio of the thermal to the momentum diffusion time scales.
- Magnetic Reynolds no ($R_{\rm m}$): The ratio of the generation or advection of the magnetic field and dissipation of the magnetic field ($|\mathbf{U}|\delta x/\eta$). It varies the same as fluid Reynolds no for $\mathrm{Pr_m} = 1$ case.
- Magnetic Prandtl no ($\mathrm{Pr_m}$): The ratio of the momentum diffusion to the Ohmic diffusion coefficient. In terms of the time scale, it is the inverse one. We have performed a set of simulations with $\mathrm{Pr_m} = 1$ over the entire height range. For another set, we tested $\mathrm{Pr_m} = 0.2$ in the convection zone and 20.0 in the coronal height.
- Plasma-β: It is the ratio of the gas and magnetic pressure ($p_{\rm g}/p_{\rm m}$). In the convection zone, it reaches as high as 10^7. In the corona, the ratio becomes 10^{-1}.

2.16 Various physical time scales and time integration method

In dynamic numerical modeling, one of the key components is the effective time scale of the configuration to evolve the model stably. There are various time scales associated with different physical mechanisms in our model. Here is a list of the smallest time scales associated with different phenomena, measured over the entire numerical domain,

- Sound wave travel time ($\delta x/c_s$): 0.24 s
- Alfvén wave crossing time ($\delta x/\mathbf{U}_A$): 0.03 s
- Momentum diffusion time ($\delta x^2/(\nu + k^4\nu^3)$): 460 s
- Ohmic diffusion time ($\delta x^2/(\eta + k^4\eta^3)$): 460 s
- Photon travel time duration before getting absorbed ($c_{\rm v}/4\kappa\sigma T^3$): 0.7 ms

Now the effective time step to resolve all physical processes is the smallest time scale corresponding to the fastest mechanism (Brandenburg et al., 2020). We adapt a dynamically effective time step approach against the fixed time one for better numerical stability.

$$\delta t = \min\left(c_{\delta t}\frac{\delta x_{\rm min}}{U_{\rm max}}, c_{\delta t,{\rm U}}\frac{\delta x_{\rm min}^2}{D_{\rm max}}, c_{\delta t,{\rm s}}\frac{1}{H_{\rm max}}\right), \tag{2.40}$$

$$U_{\rm max} \equiv \max\left(|u| + \sqrt{c_s^2 + v_{\rm A}^2}\right), \tag{2.41}$$

$$D_{\max} = \max(\nu, \gamma\chi, \eta, D), \tag{2.42}$$

$$H_{\max} = \max\left(\frac{2\nu\mathbf{S}^2 + \zeta_{\text{shock}}(\boldsymbol{\nabla}\cdot u)^2 + ...}{c_v T}\right), \tag{2.43}$$

Here $c_{\delta t}, c_{\delta t,\text{U}}, c_{\delta t,\text{s}}$ are Courant–Friedrichs–Lewy (CFL) coefficients associated with advection, diffusion and heating or cooling processes. They have a typical range of between $0.10 - 0.25$. $D_{\max}$ corresponds to the maximum diffusion coefficients among various diffusion mechanisms. In our numerical domain, the photon crossing time for the average mean free path in the convection zone is the smallest due to the strong photon-matter coupling. Therefore all dynamical equations are integrated in time following the photon crossing time scale.

For integration, we choose 3rd–order explicit Runge–Kutta method considering internal sub–steps. With such a higher-order scheme, it is possible to reduce numerical errors in the amplitude and phase part of the solution. Other common approaches are to use super time steps and implicit algorithms, but they do not guarantee the convergence of the solution. Although such schemes are memory expensive. Here we use the memory-effective $2N$ schemes that ask for only two sets of variables to be kept in memory (Williamson, 1980).

3

Genesis of Solar spicule forest: from MHD simulations and laboratory experiments

Spicular jets are highly elongated [4000 – 12000 km in length, 300 – 1100 km in width] features which are believed to transport momentum to the solar wind and non-thermal energy to heat the atmosphere (Beckers, 1972; Sterling, 2000; Tsiropoula et al., 2012). Several mechanisms have been proposed to account for the formation of solar spicules, including granular squeezing (Roberts, 1979), shocks and pulses (Hollweg, 1982; Suematsu et al., 1982; Iijima & Yokoyama, 2015), solar global acoustic waves (De Pontieu et al., 2004; Heggland et al., 2007; Heggland et al., 2011). So far, models based on these drivers have not been able to quantitatively match both the heights and abundance of the observed solar spicules. This is one of the reasons why the focus in the community has shifted to other mechanisms e.g., Alfvén waves (Haerendel, 1992; Liu et al., 2019), magnetic reconnection (Sterling et al., 1991; Shibata et al., 2007; Samanta et al., 2019), magnetic tension release aided by ion-neutral coupling (Martínez-Sykora et al., 2017), and the Lorentz force (Iijima & Yokoyama, 2017) to produce a few jets whose heights agree better with observations.

3.1 Similarity between plasma jets and polymeric fluid jets

A visually similar jetting behaviour is also seen at the free surface of a fluid layer when vertically oscillated in what is known as Faraday excitation (Faraday, 1831). Resonant mode coupling (Rajchenbach et al., 2013) in such systems lead to horizontal pattern formation. Beyond a threshold excitation amplitude, droplets or jet ejections occur by subsequent focusing of surface gravity-capillary waves in Newtonian fluids (Goodridge et al., 1996) as well as polymeric solutions (Wagner et al., 1999; Cabeza & Rosen, 2007). These table-top experiments of jets in a buffeted polymeric fluid motivates the question: would not such a mechanism also assemble a forest of spicules in a solar simulation, where the anisotropic magnetized solar plasma is analogously buffeted by convection and global modes. Physically, the interaction of magnetic fields with the plasma turbulence is analogous to that between long-chain polymers and thermal fluctuations in a viscoelastic fluid (Longcope et al., 2003). This parallel has been shown to exist in a shearing geometry (i.e., Couette flow) as the viscoelastic stresses in dilute polymeric fluids which follow the Oldroyd-B model and the Maxwell's stresses in magnetohydrodynamics (MHD) have mathematically similar off-diagonal terms (Ogilvie & Proctor, 2003) that physically manifest as anisotropy in the respective mediums. We extend the analogy between Oldroyd-B model and MHD to elongational stresses, σ_{ij}, where the magnetic field in the plasma plays a role analogous to polymeric fluid properties dependent on concentration . In a nutshell, we can compare the diagonal term or σ_{zz} in the stress tensor due to uniaxial elongational stresses, in both systems, as

$$\frac{B_x^2 + B_z^2}{2\mu_0} \leftrightarrow \frac{2\mathrm{Tr}(c)\eta_p(c)\dot{\epsilon}}{3}.$$

Here, μ_0 is the permeability, B_x, B_z are magnetic field components along the x and z-directions, respectively. The Trouton ratio which is a function of polymer concentration is denoted $\mathrm{Tr}(c)$, the viscosity of the polymeric solution at no applied shear is $\eta_p(c)$, and $\dot{\epsilon}$ is the strain rate [see §1 of Supplementary Information for details]. In this work, we provide evidence of how this similarity can be utilized to arrive at the common conditions for the formation of a forest of jets in both the systems by subjecting the solar-like atmosphere to harmonic oscillations similar to Faraday excitation in fluids. The term "forest" is used here for several jets taller than a threshold height seen in both scenarios. The ejection locations do not have a strong relation to the shape of the container or the spatial pattern of the driver. It also refers to spicules obtained in a range of heights commensurate with solar observations. By implementing harmonic vibrations self-consistently generated by subsurface solar-like convection, we identify a model that is able to capture the features of the forest of solar spicules.

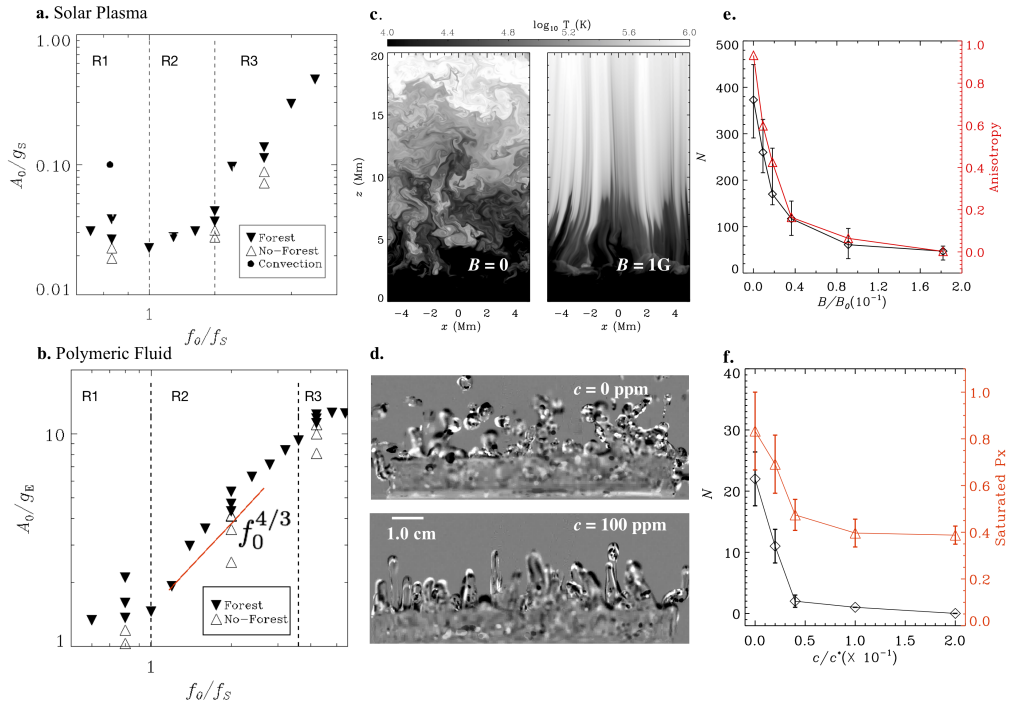

Fig. 3.1 **Large acceleration and anisotropy**: (a) An A_0 versus f_0 phase plot to determine the threshold acceleration, $A_{\min}$, at which the forest of jets criteria is satisfied. Each data point represents an independent simulation run, in the A_0/g_S versus f_0/f_s space with $f_s = 4$ mHz, for the solar atmosphere subjected to a harmonic driving at frequency f_0. Any simulation with given A_0 and f_0 either produces a forest of jets (filled triangle) when above a threshold or it does not (open triangle) when below. The dashed vertical lines are used to mark the regions R1, R2, and R3. The filled circle denotes the position of the 2D run with solar convection in this phase space. (b) Same as (a) but for polymeric fluid (500 ppm PEO) with $f_s = 25$ Hz and acceleration scaled by gravity, g_E. Here, also, each triangle denotes an independent experimental run. The red guiding line denotes the expected dimensional dependence $f_0^{4/3}$ for fluids. (c) Snapshots of the simulation with a harmonic forcing of amplitude 3.7 times larger than the threshold at 3.3 mHz without and with an imposed magnetic field $B_{\text{imp}} = 1$ G, respectively, as indicated. (d) Difference images for water and PEO (100 ppm), respectively at a driving frequency $f_0 = 30$ Hz and peak acceleration of 10 g_E. (e) Effect of B_{imp} on the average number of vortices detected over five snapshots equally sampled within a 5 min oscillation time period by Automated Swirl Detection Algorithm (see Methods), where the equipartition field at $z = 1.05$ Mm is $B_0 = 5.5$ G, for the same forcing as used in (c) (open diamond). Anisotropy in the images (open triangle) derived from distribution of the eigenvalues of the anisotropy gradient matrix. (f) Effect of polymer concentration, scaled by $c^* = 500$ ppm on number of droplet ejections (open diamond) and a measure of turbulence by counting saturated pixels or reflections (open triangle) obtained by averaging the maximum number of droplets/saturated pixels per cycle (18 frames) over five vibration time periods. The error bars denote the standard deviation within the same image frames mentioned in (e) and (f), respectively.

Phenomenological parallels

To begin with, we perform an ensemble of 2-dimensional numerical experiments on the solar atmosphere using the Pencil code (see Methods), wherein a harmonic forcing is applied just below the photosphere. Curiously, this mimicking of the naturally occurring solar global oscillations generates a forest of spicules, in the presence of a vertically imposed magnetic field. The threshold photospheric acceleration, $A_{\rm min}$, above which jets satisfying a set of criteria are formed, is shown in Fig. 3.1a, varying with the driving frequency, f_0 (scaled to approximate minimum $f_s = 4$ milli Hertz, mHz). Similar protocols have been applied to arrive at the threshold value of acceleration for the harmonic driving experiments with plasma as well as the polymeric fluids in the relevant domain sizes, namely: i) at least 4 jets in ten cycles reaching a height ≥ 7 Mm from photosphere (plasma) and ≥ 0.5 cm above the static level (fluid) should be seen after the nonlinear development phase described later, and ii) the jets must have an aspect ratio (width:height) lower than 0.5. The chromospheric plasma experiences a much larger acceleration due to lower density. It may be noted that the region R2, around f_s, is also where the solar global oscillation power spectrum exhibits a peak (García et al., 2005). We also demonstrate spicule formation for a case with a quasi-periodic forcing instead of a perfectly harmonic driver in Supplementary Video 1 of (Dey et al., 2022). These findings suggest that the vertical bobbing of the photosphere is the significant driver of spicule formation (Uchida, 1961; Suematsu et al., 1982; De Pontieu et al., 2004). For comparison, we conduct a series of table-top experiments on a dilute polymeric solution of polyethylene oxide (PEO) excited using a speaker at low audio frequencies. For forced vertical acceleration with a time dependence, $A_0 \sin(2\pi f_0 t)$, the $A_{\rm min}$ at each f_0, where the above forest of jets criteria is satisfied, is arrived at by carrying out a series of individual experiments by sampling the amplitude, A_0, corresponding to each f_0. This process, as an example, is visualized by indicative data points represented by filled and open symbols about the threshold in both the Figs. 3.1a-b (also see Methods for the protocol and §4 of Supplementary Information for an example). At other frequencies, we represent the lowest acceleration amongst those runs where the forest condition is satisfied. The behaviour of the $A_{\rm min} - f_0$ curve in region R2 (see Fig. 3.1b) is similar in both cases. In the fluid, for low driving frequencies (i.e. $< f_s = 25$ Hz or region R1), the acceleration threshold for jets shows a flattening *w.r.t.* f_0. This behavior agrees well with the existence of a cut-off forcing amplitude, obtained by solving the Mathieu equation, only above which nonlinear mode coupling is permissible (Rajchenbach et al., 2013). Likewise, an increase (shown in region R1 of Fig. 3.1 a) in threshold acceleration with decreasing frequency is also seen upon reducing $f_0 < 4$ mHz likely due to the existence of the solar acoustic cut-off frequency in the lower solar atmosphere (~ 3.3 mHz). In the driving frequency range of 30–90 Hz (region,

R2), the $f_0^{4/3}$ dependence obtained for jets by dimensional arguments for a fluid under Faraday excitation (Goodridge et al., 1997) is also shown for comparison.

The importance of long polymeric chains becomes evident at higher frequencies, where we note a change in slope at larger driving frequencies ($f_0 > 90$ Hz or region R3). This indicates the region in $A_0 - f_0$ phase space where the jet, as a result of dispersion relation of the surface gravity-capillary waves (see Methods), becomes thin enough for anisotropic elastic effects to dominate the dynamics also referred to as elasto-capillary regime (Dinic & Sharma, 2019). At higher frequencies (R3) the behaviour of the polymeric solution is different from that of the solar plasma (Fig. 3.1a). In contrast, a non-polymeric fluid (55% glycerine solution with comparable viscosity as 1000 ppm PEO solution) presents only droplet ejections and no coherent jets at these high frequencies (also see Supplementary Video 3.2a of (Dey et al., 2022)). The role of anisotropy in the jet formation process is further illustrated by comparing the effect of the same excitation on water and a dilute PEO solution in Fig. 3.1d. The consistent and sharp decrease in the number of droplets observed, even at low polymer concentrations is shown in Fig 3.1f. The droplets are formed by pinching of jets by parasitic capillary waves via the Plateau-Rayleigh Instability (Plateau, 1873; Rayleigh, 1892). The measured fluid turbulence (see Methods) points to increasing energy absorption by the uncoiling of the polymer chains and also correlates quite well with the droplet count. This stretching of the polymer chains along the jets may be imaged using a crossed polarizer setup (Fig. 3.2 with iodinated Poly vinyl alcohol (PVA) as the polymeric solution instead of PEO). The list of the solar plasma runs and polymeric fluid experiments is provided in Table 3.2.

To investigate the role of magnetic field in the vertically oscillated solar plasma, we set the magnetic field to zero in the simulations. We then observe only small-scale Kelvin-Helmholtz (KH) vortex plumes instead of jets, as shown in Fig. 3.1c. Interestingly, anisotropy created in an artificial manner by introducing a horizontal velocity damping at zero field also results in the reappearance of jets in the undamped vertical direction (see also Fig. 3.3). It may therefore be concluded that the magnetic field provides this anisotropy by collimating the rising plasma to form jet-like structures via the Maxwell's stress tensor, thereby suppressing the KH instability of the rising plumes. The effect of imposing even a weak magnetic field, say $B_{\rm imp} \sim 1$ G, in the plasma is analogous to addition of a low concentration (50 ppm) of polymer in a low viscosity solvent (Fig. 3.1e, f); both provide anisotropy, key to vertical jetting behaviour in the presence of large quasi-periodic forcing (also see §2 & 3 of Supplementary Information for an explanation of the existence of critical anisotropy measures beyond which KH and Plateau-Rayleigh instabilities are inhibited, respectively). The phenomenological parallels also extend to a few non-dimensional quantities (e.g. aspect ratio, Froude number, etc.; see Table 3.2) as well as the nonlinear dynamic evolution from the start of the vertical

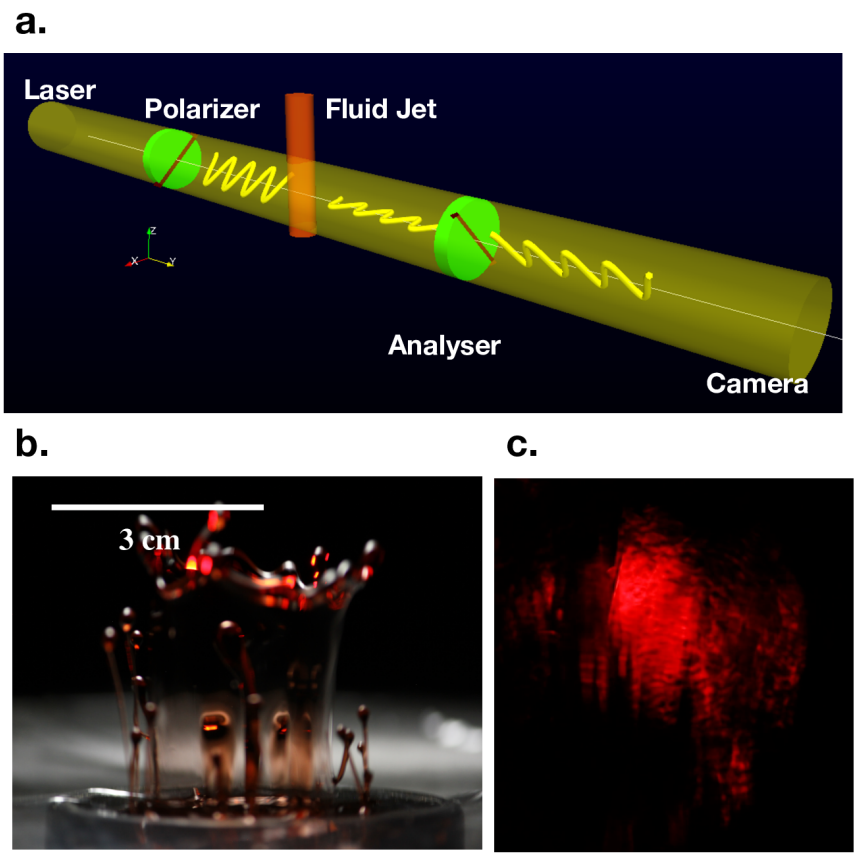

Fig. 3.2 **Signature of polymer stretching** (a) The set up for the polarization experiment for detecting polymeric stretching in 2% Poly Vinyl Alcohol. He-Ne laser light passes through a polarizer and then through the sample region of interest probing the jets, to be collected after an analyzer by an imaging device. By varying the angle of the polarizer-analyzer combination at right angles to each other, the polarization state of the jets can be determined (see Methods). (b) Jets of iodinated 2% aqueous PVA by Faraday excitation at 30 Hz. (c) Similar to (b) but seen through the polarizer set-up in (a) to highlight stretching of polymer threads.

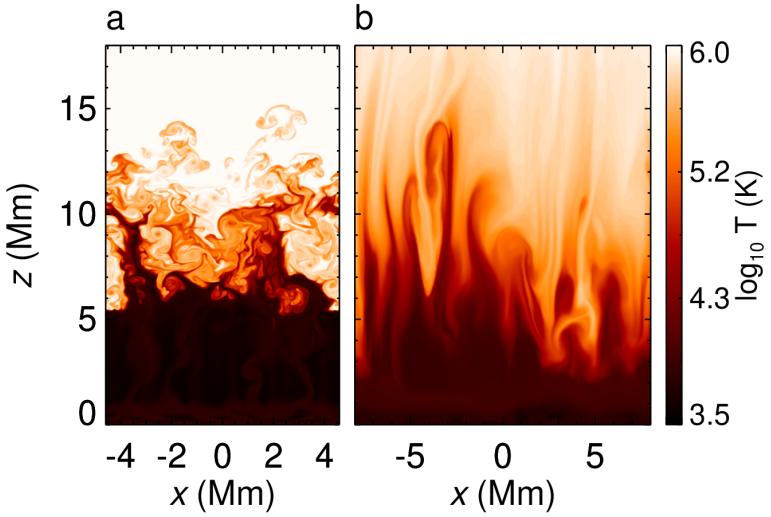

Fig. 3.3 **Kelvin-Helmholtz instability and magnetic field** (a) Contours of temperature in the simulation domain with zero imposed magnetic field shows turbulence generated by the Kelvin-Helmholtz instability. (b) Same as (a) with the addition of a damping term in the horizontal velocity equation to mimic suppression of turbulence in the horizontal direction.

Table 3.1 List of non-dimensional parameters with respect to which the two systems can be considered dynamically similar. Here, d and L are the typical width and length of the jets, whereas, U is the typical velocity scale. The Froude number indicates the importance of gravity in the dynamics. The expression for Froude number is different for two different scenarios - one for a continuum stratified solar atmosphere and the other for a fluid-air interface (polymeric fluid). The density scale height in the solar chromosphere is denoted, $H_\rho \sim 150$ km. The peak acceleration of the Faraday excitation (fluid) and chromospheric plasma acceleration, in terms of the local gravity, is given by a/g. In the fluid, the frequency of driving is $f_0 = 30$ Hz and τ is the typical lifetime of the jets. The fluids are 2% and 3% PVA solution.

Jet	d	L	U	Aspect ratio d/L	Froude number	a/g	$f_0\tau$
Plasma	0.5–1 Mm	7–20 Mm	30–50 km s^{-1}	0.05–0.15	$U\sqrt{\frac{H_\rho}{g_\odot d^2}}$ $\sim$ 0.7–2.3	4–20	1.0–1.8
Fluid	0.2–0.42 cm	1.5–4.0 cm	0.25–0.4 m s^{-1}	0.07–0.21	$U/\sqrt{g_E d}$ $\sim$ 1.2–2.2	3–15	2.0–3.0

excitation of the solar plasma in a 3-dimensional box unlike a 2-dimensional domain used previously (see Methods for details of harmonic forcing) and in the polymeric 2% PVA solution (see Supplementary Video 3.3 of (Dey et al., 2022)). The solar plasma in the 3D numerical experiment follows the spatial dependence of the forcing for a few periods before breaking up

into a crispate (or corrugated) structure. Whilst in the case of the Faraday-excited fluid, initially contra-propagating axisymmetric wave crests travel to-and-fro forming an inertial-focusing driven central jet (Zeff et al., 2000). Several jets are then formed from the circular wave crests which now resemble a crispate structure. Afterwards, we see the appearance of sub-harmonic surface distortions resembling polygonal cells. Jets are usually ejected from regions where the surface convolutions induced by Faraday excitation become focused due to the collision of ridges of neighboring polygonal cells (see Supplementary Video 3.4 of (Dey et al., 2022)). A similar forest of PVA jets also forms when instead of a purely harmonic excitation, an accelerated quasi-periodic solar acoustic excitation is used (p-modes, also Supplementary Video 5 of (Dey et al., 2022)).

Solar spicule forest with convection

In order to demonstrate the utility of this model for solar spicules, we introduce a solar-like convective layer below the photosphere. The computational results from one representative simulation run performed in a 2D box is visualized using synthetic emission from the plasma at a temperature of 80000 K (Fig. 3.4b, also see Supplementary Video 3.6 of (Dey et al., 2022)), which portrays the upper chromosphere, and using the temperature response function of the 17.1 nm filter of the Solar Dynamics Observatory's Atmospheric Imaging Assembly (Lemen et al., 2012) (SDO/AIA), which maps the lower solar corona (Fig. 3.4c). A typical forest of observed jets is shown in Si IV 140 nm (plasma temperature $\sim$ 80000 K) images sampled at the solar limb by the Interface Region Imaging Spectrograph–IRIS (De Pontieu et al., 2014) (see Fig. 3.4a where an example spicule is denoted by the arrow labelled 'S1' and Fig. 3.5a for a wider field of view). The simulated forest of spicules (panel b) qualitatively agrees well with the spicule forest from observations (panel a). The simulated spicule heights, as measured by synthetic emission peaked at a temperature of 15000 K (see Fig. 3.5d), vary between $6-24.6$ megameters (Mm) with an average of 12.6 Mm and maximum upward velocities between $30-85$ km s^{-1}, quantitatively agreeing with the statistics of observed spicules (Tsiropoula et al., 2012; Pereira et al., 2014) (Fig. 3.5b). The time-distance maps in the right panels highlight the parabolic nature of the observed (Anan et al., 2010) and simulated spicules, as well as fluid jets in acrylic paint (also, Supplementary Video 3.7 of (Dey et al., 2022)). The measured deceleration is consistently higher for polymeric jets as compared to non-polymeric ones. To illustrate this, we use five isolated and vertical representative jets in 1000 ppm PEO solution (29.5 ± 4.4 m s^{-2}) as well as glycerine solutions (15.8 ± 1.6 m s^{-2}) as compared to ejected droplets (9.5 ± 0.7 m s^{-2}) (see Supplementary Video 3.2b at 30 Hz for few exemplary cases). This may indicate the additional tension forces exerted by the uncoiled polymer chains in

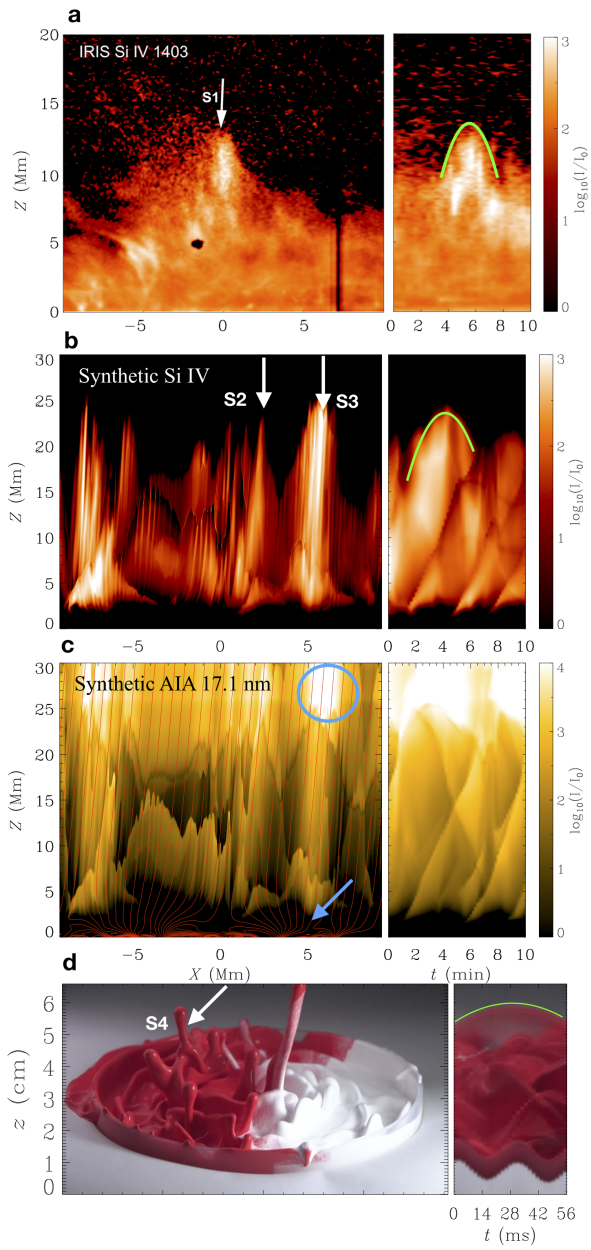

Fig. 3.4 **Comparison of 2D simulation with observation and laboratory experiment.** Left panels: (a) Spicules seen at the solar limb with the Si IV filter of IRIS. (b) Shaded contours of synthetic intensity for plasma at $T = 8 \times 10^4$ K (using Eq. 3.2), for the 2D simulation run with $B_{\rm imp} = 74$ G and solar-like convection at time, $t = 152.50$ min from the start are shown in the $[x, z]$–plane. (c) Same as (b) but for the synthetic intensity of the AIA 17.1 nm spectral line. The blue circle denote the region of increased emission intensity in extreme ultraviolet 17.1 nm line above the spicule captured by the slit, S3. The blue arrow points to the magnetic reconnection occurring below and the solid red lines represent the magnetic field. The intensities are scaled by their horizontal average denoted $I_0(z)$ at every height.
(d) Jets of acrylic paint for Faraday excitation at 30 Hz with an amplitude of $7g_{\rm E}$. Right panels: (a)–(d) corresponding time-distance plots for the slits S1–S4 indicated. The green curves in (a), (b) and (d) are the parabolic fit to the time-distance plots for isolated jets S1, S2 and S4.

PEO for polymeric jets in contrast to glycerine solution of similar viscosity. We now show that this model of solar spicule generation brings out the following insights into the origin and the structure of observed spicules. Using the technique of Lagrangian tracking, it is clear that inside a spicular structure the plasma at the photospheric and low chromospheric heights does not rise all the way to corona (see Supplementary Video 3.8a of (Dey et al., 2022)). All the plasma that rises to coronal heights (> 6 Mm) comes from above 2 Mm. The disparity in the heights reached by plasma originating from separate layers potentially explains the varying lengths of spicules in different observational channelsPereira et al. (2014). The numerical experiment finds that even if the upward acceleration measured in the chromosphere is only $\sim 4g_S$, in terms of the gravity at the solar surface but reaching as large as $12g_S$ in some regions between 1–2 Mm, the plasma is energized to speeds above $30\,\mathrm{km\,s^{-1}}$ (Fig. 3.6d) by an acceleration front propagating ahead and upwards at the speed of sound (Fig. 3.7, and Fig. 3.8a). Because of this front, the entire plasma inside the synthetic solar spicule does not rise and fall in unison. Usually, the plasma inside the front is still speeding upwards even while the plasma below the front is either slowing its rise or is falling down (Supplementary Video 3.8b–c of (Dey et al., 2022)). Obviously, the acceleration front communicates the dominant photospheric acoustic forcing to the rest of the atmosphere and is also the region of large compression or shock. This front exhibits steepening as it propagates into the region of decreasing density from the lower chromosphere to the corona. The heating inside this front is dominated by compression of the shocked plasma rather than dissipation due to viscosity or Ohmic currents as evident from the Fig. 3.8a–c. The technique of Lagrangian tracking brings to the fore the fine structure of the flows inside the spicules; the detection of such flows within spicules may be possible using the ultra-high resolution observations of the solar chromosphere that will be revealed by the next generation of solar telescopes. We report a continuously decaying distribution of spicule heights in our simulation as well as fluid jets in the experiment with shorter being dominant in number than longer jets (see Fig. 3.9a, b). Note the slightly enhanced abundance at the tall end of the height distribution. The p-value from the Kolmogorov-Smirnov statistical test on the cumulative distributions is 0.41 (Fig. 3.9c), indicating that the null hypothesis of both distributions being similar cannot be rejected. At least two classes of spicules have also been reported in observations (Beckers, 1972; De Pontieu et al., 2007a). In this context, our findings are summarized below. *Short spicules*, in our simulations, form above the convective down-flow regions where the magnetic field opens up as a funnel. The formation of a convective plume squeezes the magnetic flux tube and, therefore, forces the plasma trapped inside to shoot upwards along the field lines into the upper atmosphere (Fig. 3.6b). The convergence speed at the photosphere is around $1\,\mathrm{km\,s^{-1}}$ as estimated (Roberts, 1979). Additionally, we also report an event where a collapsing granule between two convective plumes (P1 and P2)

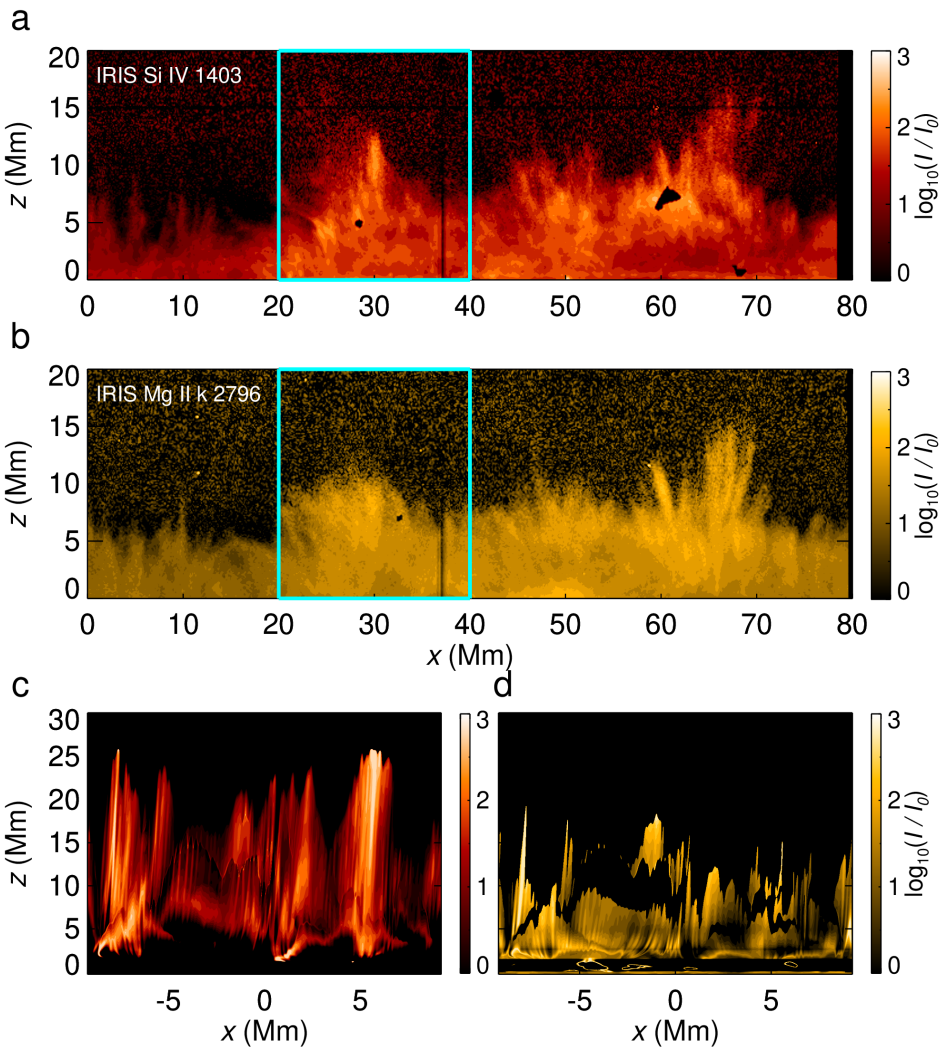

Fig. 3.5 **Observed and simulated spicules seen in Si IV and Mg II emission lines** (a) Spicules seen at the solar limb with the Si IV filter of IRIS. (b) Same as (a) but for IRIS Mg II k filter. (c) Shaded contours of synthetic intensity of Si IV emission synthesized using the CHIANTI package available in the FoMo code, for the simulation run with imposed vertical magnetic field $B_{\rm imp} = 74$ G at time, $t = 152.50$ min from the start are shown in the $[x,z]$-plane. (d) Same as (c) but for emission at Mg II k also using CHIANTI. The cyan rectangle in panels (a) and (b) indicates the same extent as the simulation domain shown in (c)-(d).

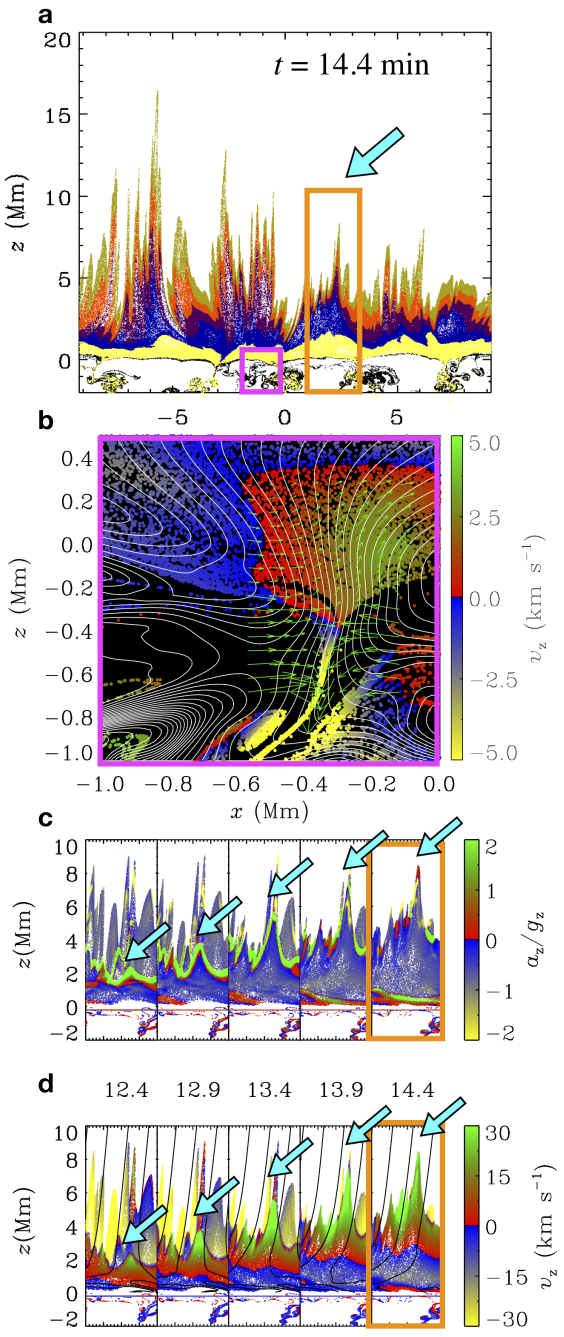

Fig. 3.6 **Origin of forest of spicular plasma in the 2D simulation with convection**: (a) Position of 540000 Lagrangian tracking particles initially arranged in six different vertical layers (indicated by different colors) at 14.4 min from the time the particles were first introduced. (b) Magnetic field lines (white) and tracking particles (colored by vertical velocity) in the region of convective downdraft shown by the magenta box in panel (a). The green arrows indicate the velocity field in the region where formation of the plume squeezes the magnetic flux tube. (c) A temporal sequence of the tracking particles along a rising spicule indicated by the turquoise arrow and bounded by the orange box in (a) (in a sub domain with $1 < x < 3$ Mm) are shown with the particles shaded by the acceleration experienced relative to the solar surface gravity, 274 m s^{-2}. (d) Same as (c) except now the shading is by vertical velocity (in km s^{-1}). The time stamp of each plot between 12.4–14.4 min since the start of tracking is indicated. The solid (black) lines correspond to the magnetic field lines in the domain. The turquoise arrows in (b) and (c) follow evolution of a particular spicule.

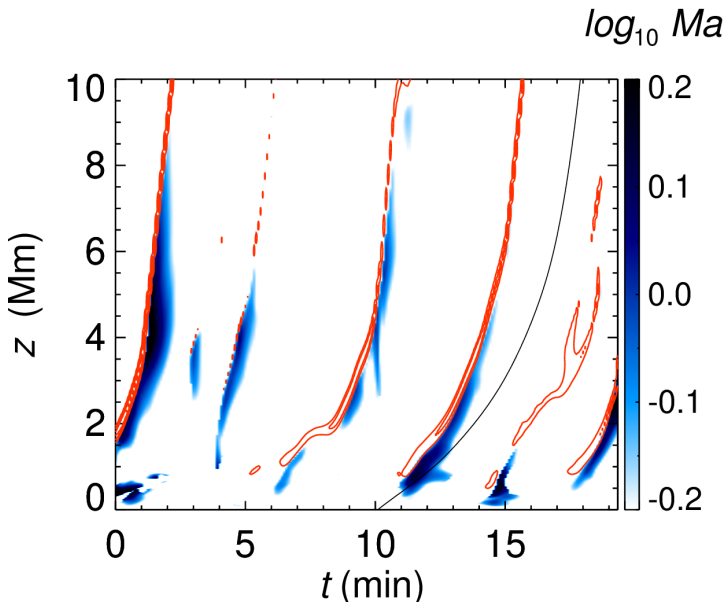

Fig. 3.7 **Propagation of shock compression and hyper-sonic regions** (a) Time-distance map of the Mach number, Ma (blue shaded), and shock compression (red contour lines) for a vertical slit at $x = 2.5$ Mm of panel (a). The regions of plasma compression, $\nabla \cdot \mathbf{V} < 0$, are found to coincide with acceleration fronts, shown in Fig. 3.6c, where the spicular plasma is energised to hypersonic speeds. The characteristic curve for acoustic waves is denoted by the solid black line.

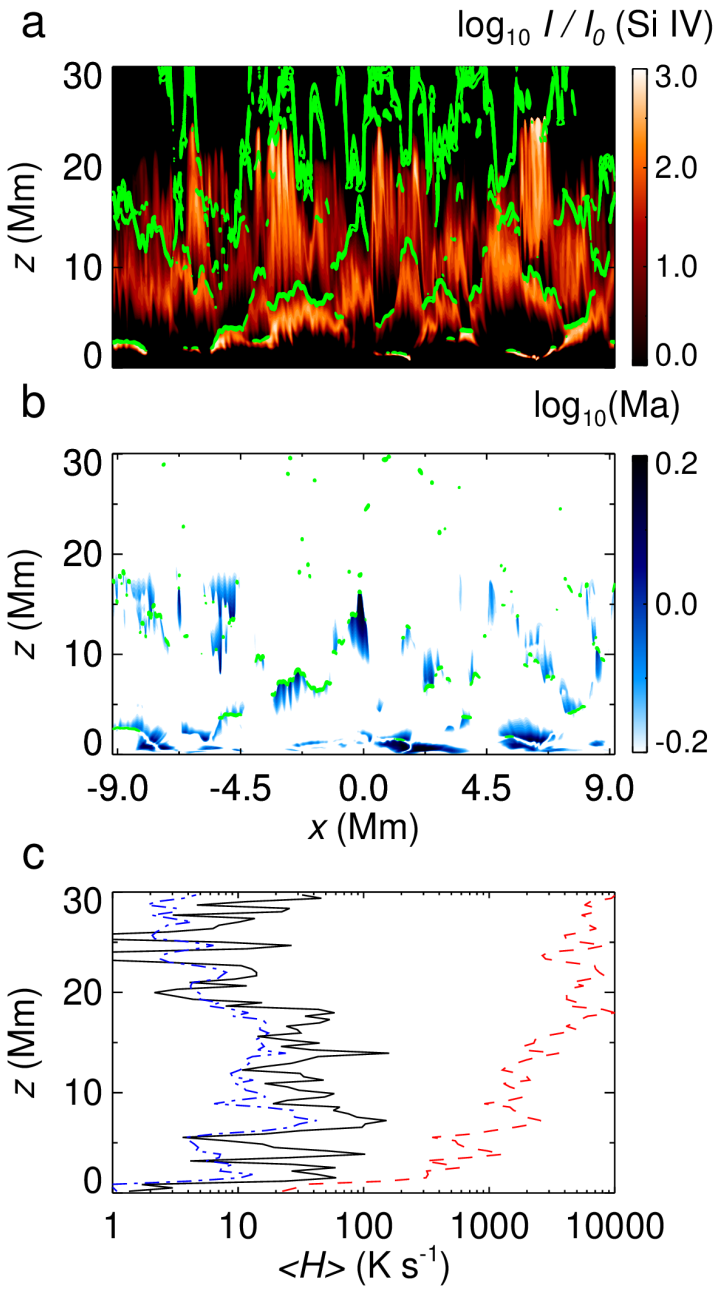

Fig. 3.8 **Plasma heating processes** (a) Synthetic Si IV emission from the simulated spicule forest similar to Fig. 3.5c calculated using CHIANTI. The green contours denote the locations of plasma heating above 10^3 K s^{-1} only due to the local compression of plasma, $-(\gamma-1)T\nabla\cdot\mathbf{V}$, where T and $\mathbf{V}$ are the plasma temperature and velocity, respectively. The ratio of specific heats denoted, $\gamma = c_P/c_V$, has been calculated using the equation of state for a partially ionized ideal gas. (b) Regions of Mach number, $Ma > 1$, are indicated by shaded blue contours. Here, the green contours show heating above 10^3 K s^{-1} only due to dissipation inside the shocks by $\zeta_{\rm shock}(\nabla\cdot\mathbf{V})^2/c_V$, where $\zeta_{\rm shock}$ is the shock viscosity. (c) Strength of various heating sources as function of height in the atmosphere. Horizontally averaged heating profiles, $\langle H\rangle(z)$, due to local plasma compression (red-dashed), shock dissipation (black-solid), and Ohmic heating (blue dot-dashed).

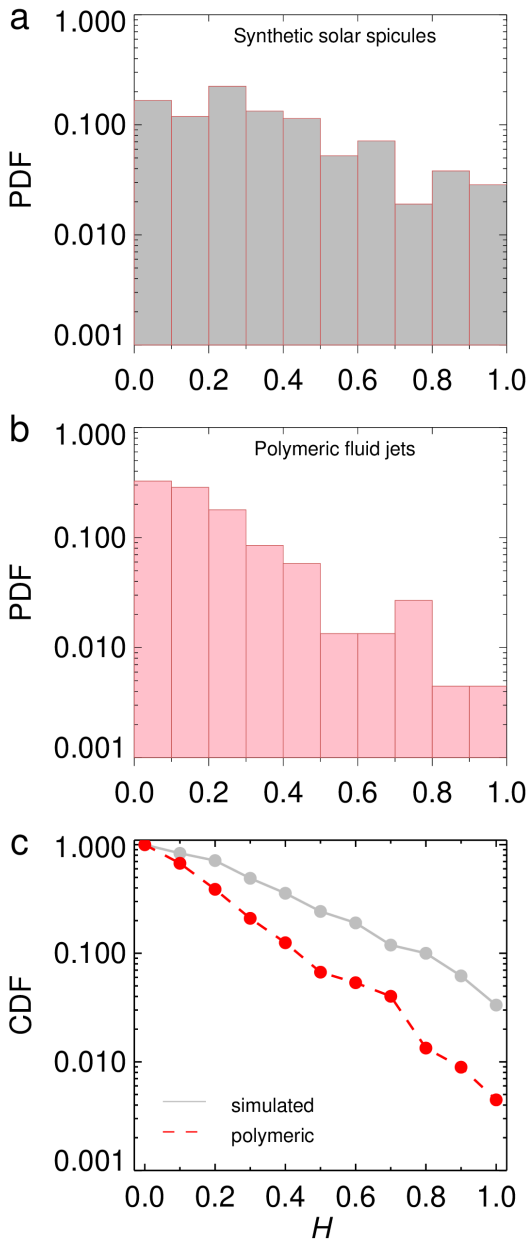

Fig. 3.9 **Comparing height distribution of solar spicules and fluid jets** (a) Histogram for distribution of $H = (h - h_{\min})/(h_{\max} - h_{\min})$, where h is the maximum height reached by a spicule and $h_{\min}$, $h_{\max}$ are the minimum and maximum heights of a sample of unique spicules (sample size 210 and counted during 40 min of solar time), respectively, as seen in synthetic emission at $T = 15,000$ K from the simulation shown in Fig. 3.5b. (b) The distribution of H from a sample of unique fluid jets (sample size 224 and counted during 10 excitation periods post the central jet ejection) in an experiment with iodinated 2% PVA. Note that only spicules such that $6 < h < 24.9$ Mm and fluid jets such that $0.5 < h < 4.5$ cm have been included in the distribution. The lower limit in the simulation is chosen because individual spicules cannot be discerned if they are below 6 Mm, whereas, in the experiment the lower end is set by the container height of 0.5 cm. The upper limits are the maximum heights obtained in the experiments.(c) The cumulative distribution function (CDF) to indicate the number of jets above $h > h_{\min}$ for both plasma and polymeric fluid.

causes these plumes to collide and eject a spicule (see Supplementary Video 3.8d of (Dey et al., 2022)). *Long spicules* form in regions above the convective granules where the magnetic field is organized in the form of low-lying loops. The sub-surface convection excites motions whose power spectrum is peaked at about 3.3 mHz (solar global oscillations) causing the solar surface, represented by the boundary of the convective granules, to rise and fall quasi-periodically. This leads to formation of a stronger acceleration front than those above the squeezing sites as shown in the phase plots of vertical components of acceleration and velocity, namely, a_z vs v_z in Fig. 3.10b as compared to panel (d). It has been argued that the power of the solar global oscillations reaching the atmosphere is usually higher over a granule than above an inter-granular lane (Hansteen et al., 2006; De Pontieu et al., 2007a). In the chromosphere, the resultant plasma motions push oppositely directed magnetic field lines together causing magnetic reconnection between the open field lines and the low lying loops. This process aids the plasma to escape along the newly opened field lines leading to the generation of faster, and longer spicules as shown in Figs. 3.6c–d (also see Supplementary Video 3.8e of (Dey et al., 2022)). Additionally, long spicules display bright tips when the AIA 17.1 nm intensity is synthesised, (blue circles over-laid on Fig. 3.4c, also Supplementary Video 3.6 of (Dey et al., 2022)), consistent with observations Pereira et al. (2014); Henriques et al. (2016); Samanta et al. (2019). The enhanced emission can be further seen in the time-distance maps of both observed and simulated spicules (Fig. 3.4a–c) whereas the shorter spicules do not have discernible emission at the tip. In either case, the vertical acceleration due to the Lorentz force does not appear to play a major role in accelerating the plasma here (Fig. 3.10c and f).

In terms of underlining physics of jetting phenomena in the two systems, the commonalities are: i) a large amplitude quasi-periodic forcing leads to nonlinear steepening of outward propagating acceleration fronts (in compressible and stratified plasma) or focusing of surface gravity-capillary wave crests (incompressible fluid); ii) anisotropic stresses in the solar atmosphere collimate the plasma and suppress the Kelvin-Helmholtz (KH) instability while the same in a buffeted polymeric fluid suppress the Plateau-Rayleigh instability; iii) the apex height of the jets vary as a parabolic function of time; and, finally iv) a decaying distribution of heights exists for both the plasma and fluid jets. Despite the behavioural similarities significant differences between the two systems exist, compressibility and the relevant nature of tension being noteworthy. For the compressible solar plasma, the dominant power is in a narrow band around 5-min acoustic p-mode whereas the polymeric fluid does not have such modes at 30-120 Hz driving frequencies. However, the fluid system can still respond to an oscillatory driver by means of surface gravity-capillary waves.

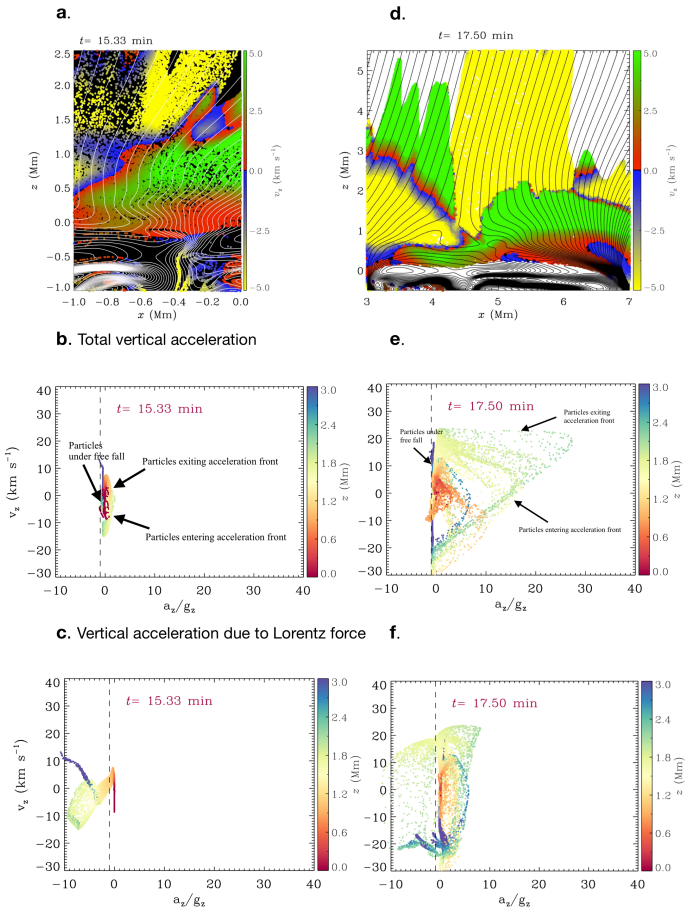

Fig. 3.10 **Phase plot of vertical component of velocity, v_z versus acceleration, a_z.** (a) The region around a shorter spicule above an inter granular lane squeezing site used for the calculation at $t = 15.33$ min from the start of tracking. Each dot denotes a Lagrangian particle colored by its instantaneous vertical velocity, v_z. The yellow contours are magnetic field lines. (b) v_z versus a_z. (c) v_z versus the vertical acceleration only due to the Lorentz force. Note that the particles considered, initially at $t = 0$ lie in layers $0 < z < 3$ Mm. Every dots denotes a particle and colored by its instantaneous vertical position. (d) The region where a longer spicule takes birth just above a granule at $t = 17.50$ min. The magnetic field lines are shown by black contours. (e) and (f) are same as (b) and (c), respectively, but, for the case of the longer spicule shown in (d).

Insights into the spicule forest

In the context of solar spicules, we now report the following results, compared to previous works (Iijima & Yokoyama, 2015; Martínez-Sykora et al., 2017; Iijima & Yokoyama, 2017). Namely, a forest of spicules are formed in our simulations with heights ranging between 6–25 Mm, bearing significantly closer resemblance to clusters of jets observed in the solar atmosphere. The plasma from the chromosphere, in contrast to the heavier photospheric plasma, can be readily energised by acceleration fronts to form taller as well as shorter spicules. The acceleration fronts are themselves generated by several mechanisms including e.g. i) squeezing by granular buffeting (Roberts, 1979), ii) collapse of granules (Martínez-Sykora et al., 2009) and, iii) solar global modes (De Pontieu et al., 2004), aided by magnetic reconnection, each ultimately induced by the same agent: convection. Are other mechanisms important? Specific mechanisms may be relevant for some kinds of spicules though (ambipolar diffusion (Martínez-Sykora et al., 2017), Lorentz force (Iijima & Yokoyama, 2017), Alfven pulses (Haerendel, 1992; Liu et al., 2019; Sakaue & Shibata, 2020), magnetic reconnection (Sterling et al., 1991; Shibata et al., 2007) etc). A question to explore would be whether these other mechanisms on their own are able to account for the abundance of the rapid and tall spicules as seen in this study, as well as in the Hinode (De Pontieu et al., 2007a) and BBSO data (Samanta et al., 2019). In addition to the forest feature of spicules, our model also captures their main characteristics in spite of not including chromospheric microphysics of ambipolar diffusion and non-local thermodynamic equilibrium of the partially ionized plasma (Martínez-Sykora et al., 2017). The phenomenological and mathematical similarities between the fluid and plasma despite the lack of charge-related effects (e.g., Hall term, ion-neutral collision) as well as specific thermodynamic considerations in the fluid point to an even more fundamental cause behind the generation of a forest of spicules. The insight provided by the polymeric fluid experiments when combined with the commonalities with the numerical solar MHD simulations is that four basic ingredients - a fluid medium, gravity, large amplitude quasi-periodic driving, and anisotropy of the medium - are sufficient to assemble a forest of spicules on the Sun by nonlinear development.

3.2 Methods

3.2.1 The radiative MHD set-up:

In this work, we model the solar plasma using the single fluid MHD approximation, where the magnetic field, **B** in the lab frame is generated due to the plasma moving at non-relativistic velocity, **v**. Following the Ohm's law the electric field, **E** can be related to the current density,

$\mathbf{J}$ as: $\mu_0 \eta \mathbf{J} = \mathbf{E} + \mathbf{v} \times \mathbf{B}$, where, η is the resistivity of the plasma and μ_0 is the magnetic permeability in vacuum. Our simulation set-up couples the sub-surface convection to the solar corona using (a) an equation of state with ionization fraction calculated from the Saha ionization formula assuming local thermodynamic equilibrium (LTE), (b) detailed radiative transfer equation which is solved by the method of long characteristics. We assume the grey approximation with the source function given by the Planck's black body function, integrated over all frequencies. Further, we use a Rosseland mean of bound-free, free-free opacities (in Kramer's law form) and H^- opacity in the chromosphere (Chatterjee, 2020). An optically thin radiative cooling (Cook et al., 1989) obtained by using a linear piecewise interpolation in $\log T$ is also used in the corona, (c) large anisotropic thermal conduction along magnetic field lines, and (d) semi-relativistic Boris correction to the Lorentz force. The use of Boris correction to the Lorentz force allows us to work with a time-step, $\delta t > dx/v_A$, where, dx denotes the grid size and, v_A is the local Alfvén speed (Chatterjee, 2020). In the domain, we impose a constant vertical magnetic field, $B_{\rm imp}$ at all times so that the net magnetic flux out of the photosphere is positive. The role of $B_{\rm imp}$ is to emulate the large-scale dynamo generated poloidal magnetic field of the Sun which cannot be produced self-consistently in a box-shaped model with a shallow convection region and without any shear. The convection acts on this imposed magnetic field to generate the small-scale magnetic flux at the photosphere. The grid size is 16 km which is sufficient to resolve the thin transition region of the solar atmosphere. The top 12 Mm of the vertical extent consists of a "sponge" layer, the purpose of which is to absorb the outgoing waves without letting them reflect back into the domain. Right at the base of this sponge layer lies a "hot plate" which maintains the temperature at $T_{\rm SL}$. The base of the sponge layer is located at $z = 32$ Mm where the temperature is maintained at $T_{\rm SL} = 1$ million K. Since we do not have any explicit heat source in the corona, this method also prevents the corona from cooling during the time scales required for the convection to reach steady-state at $t \approx 60$ min.

For quantitative comparisons with the fluid experiments, we use a 2-dimensional domain of width, $L = 9,$ Mm and extending vertically from -0.4 Mm$< z <$ 44 Mm, with $z = 0$ representing the photosphere. The initial stratification of temperature is obtained by collating the Model S (Christensen-Dalsgaard et al., 1996) for the interior and an atmospheric model (Vernazza et al., 1981). The initial density corresponding to this temperature is obtained by solving the hydrostatic balance subjected to the ionized ideal gas equation of state with ionization fraction given by the Saha-ionization formula (Chatterjee, 2020). We fix the temperature and density at the bottom boundary ($z = -0.4$ Mm) to values taken from the Model S. The flow at the bottom boundary is stress free and the top boundary is open to flows. At the start of the simulation, $B_{\rm imp} = 0$ and is increased to 12 G over a duration of $t_{\rm fin} = 10$ min solar time in the manner

$B_{\rm imp} = B^0_{\rm imp} \sin^2(\pi t/2t_{\rm fin})$. This is so that the atmosphere remains in quasi magneto-hydrostatic equilibrium throughout. Thereafter, we drive this set-up with a periodic membrane forcing velocity of the form $V_0 \sin(2\pi f_0 t)\cos(n\pi x/L)$ within a subsurface layer, $-100 < z < 0$ km, to investigate the role of artificial harmonic forcing. Here, n is the number of crests of the membrane forcing that fits into length L of the box (see Table 3.2 for values used for different runs). Below this layer, the velocities are set to zero. The amplitude of the corresponding acceleration is $A_0 = 2\pi f_0 V_0$. We have followed the above protocol to make sure that the excitation amplitude, uncontaminated by convective motions, can be clearly determined for the A_0 vs f_0 phase space. The horizontal wave number of five is chosen to agree with a typical solar granulation scale of 2 Mm. To generate Fig. 3.1a, the code is first run for 25 cycle periods $(1/f_0)$, after the start of the wave driving, to check for nonlinear development. In the case when we observe several spicules close together formed by crispation (*like of a compound leaf*) of the wave front, we continue to run it for another 10 cycle periods to further check for the height and aspect ratio criteria. But, if we do not observe any such nonlinear development during the first 25 cycles, we discard the run and change the amplitude of driving suitably before conducting a new run.

A three-dimensional box is used for comparison with the fluid set-up to show the parallels in nonlinear development. A very shallow sub-surface layer is used here as well (300 km) but, with a grid size of 24 km. A slightly different method compared to the 2D runs of Fig. 3.1 has been followed in order to match the time to formation of forest of jets with that of the polymeric solution (in terms of $1/f_0$). Here, the membrane forcing is of the form $V_0 \sin(2\pi f_0 t)\cos(\pi x/L)\cos(\pi y/L)$, with $f_0 = 3.3$ mHz and $V_0 = 1.32$ km s^{-1}, and only applied within a layer, -100 km $< z < 0$ km. In the 3D box, we do not set the velocities to zero below that layer (unlike in Fig. 3.1), forcefully. Therefore, we had to verify that if the membrane forcing is not applied, jets do not form within the duration of the animation (25 min solar time). The root mean square (rms) velocity reached in this shallow layer at the end of 25 min, in absence of additional harmonic forcing, is ~ 0.4 km s^{-1} which does not drive jets in this set-up.

For comparison with solar observations, we use a two-dimensional model with a deeper (5 Mm) statistically relaxed convective layer, so that the vertical extent is now -5 Mm$< z <$ 44 Mm. We follow the same steps as above to arrive at the initial stratification of temperature and density. However, now the slopes, $d\ln\rho/dz$ and $d\ln T/dz$, in the ghost zones are set to values expected from hydrostatic balance at the vertical boundaries. The $B_{\rm imp}$ is increased as described previously from zero to 74 G over a duration of 60 min solar time, after which the convection is allowed to relax for another 60 min. The final magnetic field value of 74 G has been chosen to agree with recent observations (Kriginsky et al., 2020). The temperature, density and vertical velocity structure in the $[x,z]$-plane of the 2D run shown in Fig. 3.6 at

Data Table 3.2 List of numerical and table top runs along with the figures and videos where they have been referenced. All the solar MHD simulations are performed with a sponge layer temperature, $T_{SL} = 10^6$ K. The driving velocity amplitude is V_0 at the driving frequency, f_0. The wave number $k = n\pi/L$, where n is the number of crests in the horizontal domain of length, L. For the polymeric fluid experiments, A_0 denotes the peak acceleration amplitude, c is the polymer concentration expressed either as parts-per-million (ppm) or as weight percentage, ν_p is the measured kinematic viscosity.

	Solar plasma, $T_{SL} = 10^6$ K				
Dimension	*Forcing*	V_0 (km s^{-1})	f_0(mHz)	n	B_{imp} (G)
2D	wave driving	0.45–2.50	3.0–9.0	5.0	12
	wave driving	1.32	3.3	5.0	0–1
	wave driving	1.0	mixed	5.0	12
	convection				74
	wave driving	1.32	3.3	5.0	0
3D	wave driving	1.32	3.3	1.0	10
	Polymeric fluid				
Type	*Solution*	A_0/g_E	f_0 (Hz)	c (ppm)	ν_p (10^{-7} m^2 s^{-1})
Polymeric	PEO	1.0–10.1	15–120	50, 500	9.8±0.1,20.0±1.0
	PEO	10.0	30	10-100	9.8 ± 0.1
	PEO	4.9,13.2	30,120	1000	55.0 ± 2.0
	Iod. 2% PVA	10.1	30	2% wt.	320.0±20.0
	Iod. 2% PVA	5.0	mixed	2% wt.	320.0±20.0
	Iod. 3% PVA	10.1	30	3% wt	570.0± 20.0
	Acrylic Paint	7.0	30		
Newtonian	Water	10.0	30	0	9.8±0.1
	Glycerine	1.0–10.1	15–120	55% wt.	55.0±2.0
	Glycerine	10.1	30	76 % wt.	400.0±20.0

$t = 85$ min from the start of the simulation, and also at the moment when Lagrangian particles are introduced is shown in the Fig. 3.11a–c. The convective granules are found to have sizes in the range 1–3 Mm with lifetimes of the order 4–7 min. A steady state rms convective vertical velocity obtained at the end of 120 min is ~ 1.54 km s^{-1} at the photosphere agreeing with observations (Keil & Canfield, 1978). Beyond this, the code is run for an additional solar time of 50 min during which the results are analysed. The imposed vertical magnetic field across the domain keeps the acceleration fronts more or less intact. In reality, spicules on the surface of the

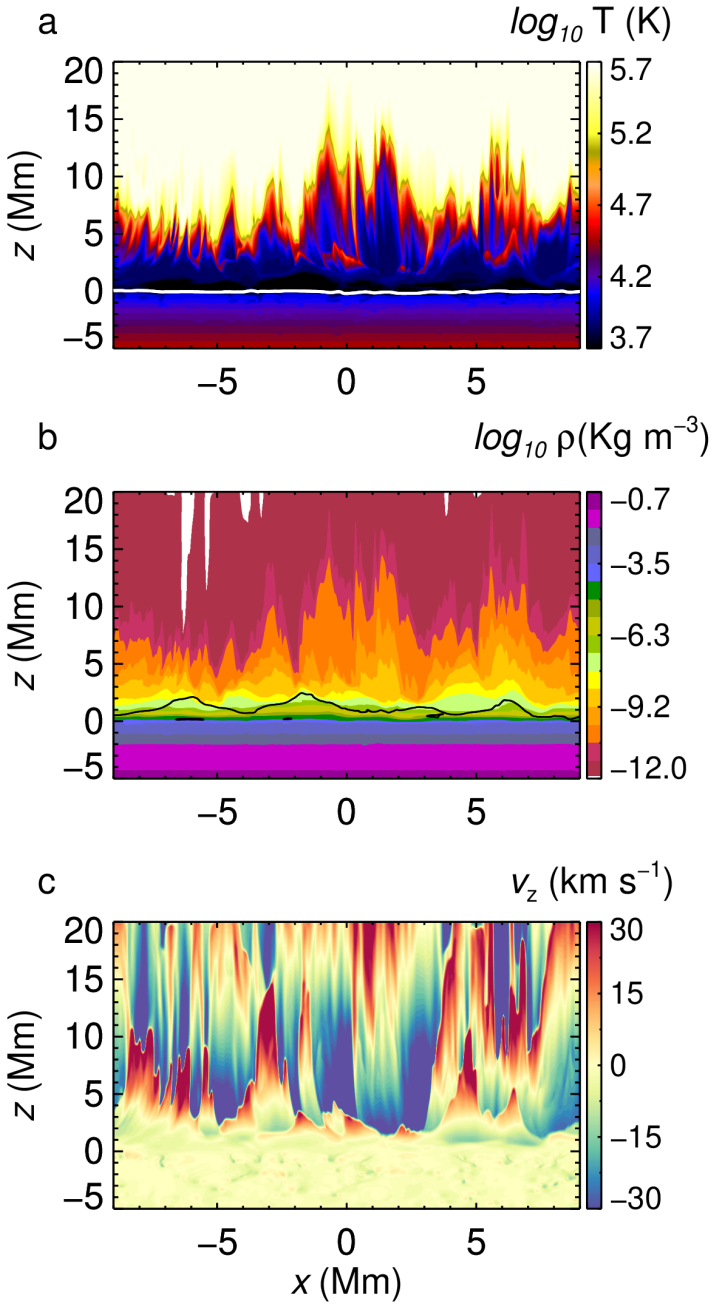

Fig. 3.11 **Solar atmospheric stratification with convection** (a) Temperature structure at the time of introduction of Lagrangian particles in the domain for the same run shown in Fig. 3.6a. The white solid line is the optical depth, $\tau = 0.1$ surface. (b) The density at the same instant as (a). The plasma $\beta = 1$ surface is denoted by the black solid line. (c) The vertical velocity, v_z corresponding to panels (a) and (b).

Sun are more prevalent in the super-granular lanes. In the 2D set-up used here, we may consider the x-axis to be aligned along such a super-granular lane. In the real Sun, this coherence is broken by the presence of horizontal magnetic fields (existing over longer horizontal scales 20–30 Mm) e.g., in inter network regions. This set-up with convection was found to generate a forest of spicules for a range of parameters, with $B_{\rm imp}$ varying from 12 G–74 G and $T_{\rm SL}$ in the range 0.6–1.8 million K (six independent simulation runs). The Pencil code set-up of the solar convection-driven simulations is available at https://doi.org/10.5281/zenodo.5807020 upon request (Chatterjee & Dey, 2022).

3.2.2 Measure of anisotropy in the plasma

We employ two separate techniques to study the effect of imposing a vertical magnetic field on the instabilities and turbulence generated in the numerical experiments. The first one is following a popular method called anisotropy invariant maps (Lumley & Newman, 1977), where calculation of a 2×2 anisotropy gradient matrix is carried out at each pixel defined as

$$a_{xz} = \frac{\partial_x \chi \partial_z \chi}{(\partial_x \chi)^2 + (\partial_z \chi)^2}. \tag{3.1}$$

Here, $\chi = \log T$. However, in a general case, it can also be defined as the intensity of each pixel of an image whose anisotropy we wish to quantify. Let the two complex eigenvalues of this matrix be λ_1 and λ_2 using which we can define two real quantities, $\xi = \lambda_1^2 + \lambda_1\lambda_2 + \lambda_2^2$ and $\zeta = -\lambda_1\lambda_2(\lambda_1 + \lambda_2)$. In our case, the distribution (PDF) of ξ over all pixels (and over all ζ values) in the domain shows an obvious trend with increasing $B_{\rm imp}$ when plotted in the $\zeta - \xi$ plane. The cumulative fraction of points, f_B, enclosed by the PDF such that the PDF> 0.1 has been used as a measure of anisotropy. We have scaled this with the cumulative fraction of points, $f_{\rm ran}$, for a case when the entire image is made up of only uniformly random numbers creating a homogenous and isotropic pattern. The curve plotted in Fig. 3.1e is $(1 - f_B)/(1 - f_{\rm ran})$ versus $B_{\rm imp}/B_0$, where B_0 is the magnetic field at the chromospheric heights ~ 1 Mm in equipartition with the kinetic energy of the harmonic driving. We perform this analysis on an image at the end of the 25 min (solar time) since the start of the harmonic driving with a time period of 5 min.

The second method followed is detecting and counting of vortex patterns in the snapshots of velocity vectors employing the technique of Automated Swirl Detection Algorithm (ASDA (Liu et al., 2019)) using its default parameters except that the lower boundary of the peak, $|\Gamma_1|$ value, (see Eq. 1 in Ref[(Liu et al., 2019)]) of a vortex is defined as 0.71. This allows us to detect all vortex candidates with an average rotating speed greater than their average expanding/shrinking

speed. The average number of such vortices detected in six frames sampled during a 5 min duration are plotted.

3.2.3 Synthetic plasma emission:

The synthetic intensity for an upper chromospheric or transition region line may be given by,

$$I_\lambda = \int G_\lambda(\rho, T)\varphi(T)dT. \tag{3.2}$$

This expression for DEM is valid (Landi & Chiuderi Drago, 2008) for temperatures between 10^4–10^8 K, where,

$$G_\lambda(\rho, T) = \exp\left[-(\log(T/T_\lambda)/w)^2\right]$$

is the "contribution" function for the line with $T_\lambda = 15000$ K (comparison with Mg II k) and 80000 K (comparison with Si IV), and $w = \log 1.8$ and $\varphi(T) = (\rho/\overline{\rho})^2 ds/dT$ is the differential emission measure scaled with the square of the horizontally averaged density, $\overline{\rho}(z)$. Similar expressions have been used (Rempel, 2016; Iijima & Yokoyama, 2017) for depicting synthetic coronal and chromospheric jets, respectively. Normally, the integration is performed along the line-of-sight (LOS), the infinitesimal element along which is ds. However, for two-dimensional runs, the integration is irrelevant as there is only one grid point along the LOS. For the visualization of the 3D run, we use the volume rendering of the quantity dI_λ/ds for $T_\lambda = 15000$ K. In order to validate the simple analytical expression for G_λ, we have further made use of the FoMo code (Van Doorsselaere et al., 2016) to obtain synthetic intensity images for Mg II 279.6 nm and Si IV 140.2 nm lines as diagnostic tools of solar chromosphere and transition regions. This code utilizes realistic contribution function $G_\lambda(\rho, T)$ from the CHIANTI database (Dere et al., 1997) by considering collisional excitation and spontaneous de-excitation processes in optically thin plasmas. We would like to caution that the forward modelled Mg II intensity profiles using these methods will not be accurate because it is not exactly in the optically thin regime and the Saha-ionisation equilibrium is an approximation in that case.

Finally, the SDO/AIA 17.1 nm emission is synthesized using the contribution function, $G_\lambda(T)$ available from the solarsoft library at `https://www.lmsal.com/solarsoft/`.

Observational data

We used a series of spicule image sequences obtained with the IRIS (Interface Region Imaging Spectrograph) at 11:24:46, on February 21, 2014 Pereira et al. (2014). The investigated area is located in the south pole of the Sun with the center solar coordinates of $x_S = 7''$and

$y_S = 969''$with a field-of-view (FOV) of $119'' \times 119''$. For our work, we analysed spicules observed with the transition region Si IV 140.0 nm (at T≈80000 K) and the chromospheric Mg II k 279.6 nm (at T≈15000 K) slit-jaw filtergrams Skogsrud et al. (2015) with a 19 s cadence. The data extracted is for a duration of 20 min from 11:24:46 UT.

In Fig. 3.4a (for Si IV) and Data Fig. 3.5b (for Mg II k), with the images in $[x,z]$–plane, we focus on an area of $80 \times 20\,\mathrm{Mm}^2$ from the slit-jaw filtergram data that were taken at 11:34:16, on February 21, 2014. The blue rectangle highlights an area with the same extent as the simulation box. To reveal the hot tip of some of the spicules, first, we determine the horizontally averaged intensity, I_0, for each pixel in the z-direction. Next, we construct an intensity map scaled by I_0 for each pixel De Pontieu et al. (2007a). To visualise the evolution of a spicule (denoted by a white arrow, S1) in the Si IV and Mg II k images of Fig. 3.4 and Data Fig. 3.5, respectively, time-distance plots were constructed.

3.2.4 Lagrangian Tracking

To decipher the plasma flow inside the simulated spicules after their formation sets in, we introduce massless particles into the computational domain for Lagrangian tracking in six separate layers between $-0.5 < z < 6$ Mm, each layer 1 Mm thick (except the bottom which is 0.5 Mm thick), represented by a different color. We observe that the particles initially within the layer $-0.5 < z < 1$ Mm never rise above a height of 2 Mm during the 19.5 min duration of tracking, as shown in Fig. 3.6a. However, the particles placed within the next $1 < z < 2$ Mm layer reach up to 6 Mm height in the form of elongated and dense spicules.

3.2.5 Polymeric fluid experimental set-up.

Extensive studies have been carried out by subjecting Newtonian and polymeric fluids to vertical harmonic vibrations of the container or Faraday excitation (Goodridge et al., 1996, 1999; Wagner et al., 1999) of the form $a(t) = A \sin \omega_0 t$, where A is the amplitude of the external excitation. Faraday waves are parametrically driven standing surface waves whose dispersion relation is given by, $\omega^2 = \tanh(kh)\left[g_{\mathrm{E}}k + \sigma k^3/\rho\right]$, with angular frequency, ω, wavenumber, k, fluid depth, h, surface tension, σ and g_{E} is the local acceleration due to gravity. The nature of the wave has a transition from surface gravity to capillary at $k' = \sqrt{g_{\mathrm{E}}\rho/\sigma}$ and corresponding frequency, $\omega' = (4g_{\mathrm{E}}^3\rho/\sigma)^{1/4}$, which define low-frequency gravity waves ($\omega < \omega'$) and high-frequency capillary waves ($\omega > \omega'$). For the first sub-harmonic Faraday waves, $\omega = \omega_0/2$ in the above dispersion relation. When the amplitude of excitation exceeds a certain threshold value of peak acceleration, A_{min}, jet or droplet ejection occurs from the surface.

For our experiments, we use polyethylene oxide (PEO), iodinated polyvinyl alcohol (PVA) and glycerine solutions of varying viscosities. PEO solutions of 1000 ppm concentration by weight were prepared by carefully dispersing a long-chain polymer (Alfa Aesar $>$ 5,000,000 M.W.) in powder form into deionized water to avoid clumping and stirred at low rpm along with occasional gentle shaking for three hours at room temperature ($\sim$ 300 K). Successive dilutions (20–500 ppm) were obtained from the above master solution using deionized water and stirred similarly for about a half-hour. Polyvinyl alcohol solutions were made from commercial grade PVA (degree of hydrolysis 85–89, Thermo-Fisher Inc.). Suitable mass percentages without any further purification were slowly added to deionized water at the beginning while stirring continued for 3 hours at a temperature of 318 K. Iodination of the solution was carried out immediately by the addition of I_2 (1 mmol l^{-1}) and KI (4 mmol l^{-1}) simultaneously to the solution and stirring for a further 3 hr at the elevated temperature. In both the cases, losses were made up and stirred further to achieve a single-phase solution. All the prepared solutions were allowed to sit at ambient temperature for 12 (PEO) and 24 (PVA) hr and stirred for about 15 min before the excitation, polarization, or rheometry experiments were performed. PEO solutions were used within 48 hr, and PVA within 120 hr, of preparation to prevent degradation.

Parallels between plasma and polymeric solutions in a different context (Magnetorotational Instability versus Elastorotational Instability in cylindrical Couette geometry) have been explored using PEO solutions previously (Boldyrev et al., 2009; Bai et al., 2015). The PEO solutions used here were found to have the following physical characteristics at 300 K (concentration: $c = 20, 50$ and 100 ppm, density: 995 kg m^{-3}, kinematic viscosity: $\nu = 9.8 \pm 0.1 \times 10^{-7}$ $m^2 s^{-1}$ and for $c = 500$ ppm, $\nu = 2.0 \pm 0.1 \times 10^{-6}$ $m^2 s^{-1}$ whereas for $c = 1000$ ppm, $\nu = 5.5 \pm 0.2 \times 10^{-6}$ $m^2 s^{-1}$). The viscosity measurements were carried out using an MCR 302 rheometer from Anton Paar with shear rates varying between 1–200 Hz. The concentration, c^*, at which the chain-chain interaction in PEO solution cannot be neglected occurs when the solution viscosity is almost twice the solvent viscosity, is about 500 ppm. The physical parameters for Iodinated 2% PVA solution were found be (density: 995 kg m^{-3}, kinematic viscosity: $\nu = 3.2 \pm 0.2 \times 10^{-5}$ $m^2 s^{-1}$ and, surface tension, σ: 0.052 N m^{-1}). Iodinated 3% PVA solution yielded similar values of density ($\rho = 982$ kg m^{-3}) and $\sigma = 0.053$ N m^{-1} but $\nu = 5.7 \pm 0.2 \times 10^{-5}$ $m^2 s^{-1}$. A 76% solution of glycerine (99.5% Sigma Aldrich) was prepared by diluting with appropriate amount of deionized water and stirred at 300 K for 20 min (ρ: 1195 kg m^{-3}, viscosity: $4.0 \pm 0.2 \times 10^{-5}$ $m^2 s^{-1}$, surface tension: 0.064 N m^{-1}).

Measurements of jet heights were performed during an interval of ten excitation periods after the ejection of the geometric central jet and prior to bubble formation. Observation of the forest of jets and related nonlinear effects are robust over a range of geometry, types of fluid, viscosity, and forcing amplitude investigated by us.

3.2.6 Excitation experiments

The excitation experiments were performed on a subwoofer speaker (12 inch 4 Ohms 200 W R1S4-12 Rockford Fosgate), powered by a 100 W audio bass amplifier. The power fed to the speaker never exceeded 60 W (fused) to allow for a linear electrical response, also to allow it to act as a Faraday shaker. Geometrical effects were not found to be significant as similar behaviour was observed on a smaller speaker with identical electrical characteristics. A levelled shallow cylindrical vessel of 0.1 m diameter was firmly anchored to the centre of the driver cap of the speaker and a fluid volume of 30 ml was added. Provision was made to measure the acceleration using a calibrated MPU 9250 (TDK Invensense) accelerometer as well as from high speed imaging with or without loading. All the experiments have been performed at 300 ± 1 K. Our peak accelerations are in the range $3 - 15 g_{\mathrm{E}}$ and we find a sub-harmonic response of the surface in all cases, even though the pattern changes over the number of periods depend on the forcing.

3.2.7 Polymer stretching on excitation

The vertical stretching of polymer chains under large excitation was observed using the same set-up. The region of interest above the vessel was shone using an enlarged cross-section He-Ne laser beam (632.8 nm) with the region of interest placed between two crossed polarizers. We use two different configurations of the crossed polarizers (Fig. 3.2a): i) 0°-90° (dark mode) in which the axis of the polarizer is aligned with the vertically polarised source and that of the analyzer is perpendicular, ii) 45°-135° (bright mode) where the polarizer-analyzer configuration is rotated by 45° to the vertical. Because of absorption by Iodine in the stretched polymer chains (Fig. 3.2b), the beam suffers extinction in the first configuration, thus resulting in a dark field both in the presence or absence of the jets. On the other hand, when the polarizer axis is turned by 45°, with the analyzer turned 135° (Fig. 3.2c), illumination is observed only in the presence of jets that offer a polarizing medium at 45° to both the polarizer and the analyzer.

The various non-dimensional numbers related to jetting in our experiments are as follows. The Ohnesorge number, $Oh = \nu\sqrt{\rho/\sigma d}$, where d is the typical jet diameter, comparing the visco-capilliary time scale, $t_v = \rho\nu d/\sigma$, to Rayleigh time scale for inviscid capillary break-up, $t_c = (\rho d^3/\sigma)^{1/2}$, takes the following values: 0.003 (water/PEO 10–100 ppm, surface tension: $\sigma \approx 0.070$ N m^{-1}), 0.005 (PEO 500 ppm), 0.098 (Iodinated PVA) and 0.12 (glycerine solutions) at 30 Hz and a forcing acceleration of $\sim 10 g_{\mathrm{E}}$. The Weber number, $We = \rho U^2 d/\sigma$, which is a measure of inertial forces to surface tension in multi-phase fluids, is in the range 4–6. In the frequency and forcing amplitude ranges covered in this study, we do not see any formation of neck or jet pinching in excitation experiments with PEO solutions of $c > 50$ ppm, in spite

of $Oh << 1$, in contrast to water (similar low viscosity). The typical strain rate experienced by polymer chains, during the rise time of the jets (~ 16 ms), is given by, $U_{\rm jet}/L_{\rm jet} \sim 13.3\,{\rm s}^{-1}$, where $U_{\rm jet}$ and $L_{\rm jet}$ are average velocity and maximum height reached by a long jet, respectively. In 2% PVA solution versus 76% glycerine solution experiments (similar but higher viscosity than PEO solutions), we observe neck formation and pinching. We note less jet breakage in PVA (23% PVA jets reaching heights above 1 cm break as compared to 53% in glycerine solution) indicating that uncoiling polymer chains may be suppressing Plateau-Rayleigh instability.

3.3 Supplementary material

3.3.1 Comparison of viscoelastic and Maxwell stresses

In a polymeric fluid, the polymer not just stretches in the flow direction but in the process also exerts a stress back on the fluid which acts to suppress the fluid turbulence. In order to quantify this back reaction, we can compare the strength of the two different terms in the Navier-Stokes equation, namely, the viscoelastic stress and the inertial stress on the fluid. Further, to motivate the polymeric fluid-MHD analogy we compare this ratio for a polymeric fluid with the corresponding ratio of the Maxwell's stress to inertial stress for the case of solar MHD. A similar exercise was carried out by (Ogilvie & Proctor, 2003) assuming the Oldroyd-B model (Oldroyd, 1950) of an incompressible viscoelastic fluid of uniform density, ρ, a polymer viscosity, η_p, and relaxation time, τ. The Oldroyd-B is a linear polymer model– viscosity $\propto$ strain rate– which is valid under two conditions, namely: i) dilute polymer solution i.e., concentrations at which polymer chain-chain interactions are negligible and; ii) the polymer chain is infinitely extensible. Even though we observe jetting behaviour in a wide range of polymer concentrations, some of which lie outside the strict validity of the Oldroyd-B, we shall consider only those experiments with Poly Ethylene Oxide (PEO) where the polymer concentration is dilute enough to enable a direct comparison in this section. A major difference with (Ogilvie & Proctor, 2003; Boldyrev et al., 2009; Bai et al., 2015) is that we use an elongational geometry applicable to jets rather than Couette flow geometry which is applicable to elasto-rotational instability (ERI). The stress tensor components in the case of uniaxial incompressible extensional flow (filamentary, Supplementary Fig.1) in 3-dimensions corresponding to the velocity field given by, $u_x = -x\dot{\varepsilon}/2$, $u_y = -y\dot{\varepsilon}/2$ and $u_z = z\dot{\varepsilon}$ can be written as (Chap 5 of (Barnes et al., 1989)),

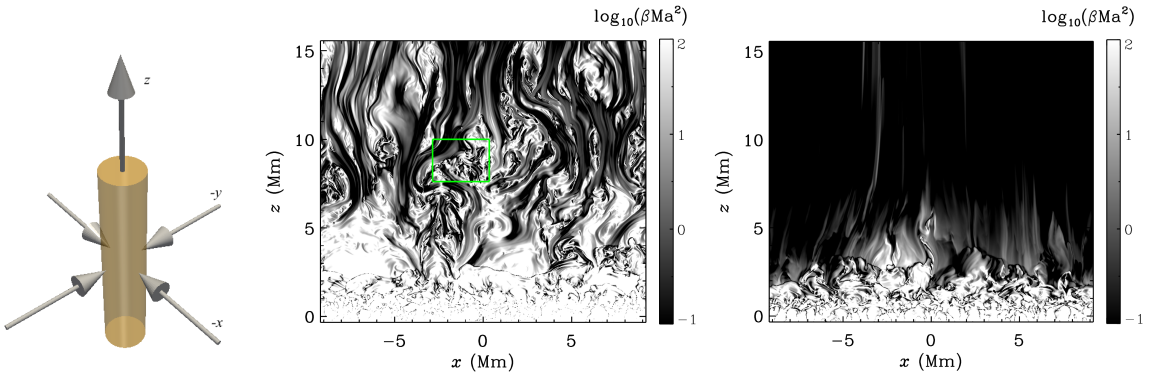

Supplementary Figure 3.12 *Left panel*: An example of a uniaxial extensional flow field. *Middle panel*: logarithm of the quantity $\beta \mathrm{Ma}^2$ for imposed vertical magnetic field $B_{\mathrm{imp}} = 0.1$ G. The green square shows the region for which the root-mean-square of velocities have been calculated in the text. *Right panel*: same as the middle panel but for $B_{\mathrm{imp}} = 1$ G.

$$\sigma_{xx} = \sigma_{yy} \tag{3.3}$$

$$\sigma_{zz} - \sigma_{xx} = \dot{\varepsilon}\eta_E(\dot{\varepsilon}) \tag{3.4}$$

$$\sigma_{xy} = \sigma_{yz} = \sigma_{xz} = 0 \tag{3.5}$$

where, $\dot{\varepsilon}$ is the strain rate and η_E is the uniaxial extensional viscosity. The traceless stress tensor, $[\sigma_{ij}]$, can then be given by,

$$\overleftrightarrow{\sigma} = \frac{\mathrm{Tr}\eta_p}{3}\begin{bmatrix} -\dot{\varepsilon} & 0 & 0 \\ 0 & -\dot{\varepsilon} & 0 \\ 0 & 0 & 2\dot{\varepsilon} \end{bmatrix} \tag{3.6}$$

where, Tr is the Trouton ratio defined as

$$\mathrm{Tr} = \frac{\eta_E(\dot{\varepsilon})}{\eta_p} \tag{3.7}$$

where, $\eta_p = \lim_{\dot{\varepsilon}\to 0}\eta_E(\dot{\varepsilon})$ is the viscosity of the polymer subjected to shearing flows as measured in our case by the Anton-Paar MCR 302 rheometer. For a Newtonian fluid, $\mathrm{Tr} = 3$, whereas for dilute aqueous polymers such as polyethylene oxide (PEO) this ratio can be as large as 10^4 depending on $\dot{\varepsilon}$. Even though in the case of Faraday excitation we have a periodic driver, yet in the absence of any detail knowledge of the functional form of the flow inside the

jet, we have made the drastic assumption that the flow is quasi-steady during the rise time of the jet, like in the case of the filamentary flow in a capillary breakup rheometry (CABER) set-up.

On the other hand the Maxwell's stress tensor is given by,

$$\mathscr{M}_{ij} = \frac{B_i B_j}{\mu_0} - \frac{B^2}{2\mu_0}\delta_{ij}. \tag{3.8}$$

In our case of a 2-dimensional set-up with $B_y = 0$, $\partial/\partial y \to 0$, and non-zero magnetic fields only in the $[x,z]$-plane, the stress tensor has a simple form given by,

$$\overleftrightarrow{\mathscr{M}} = \frac{1}{2\mu_0}\begin{bmatrix} B_x^2 - B_z^2 & 0 & 2B_xB_z \\ 0 & -B_x^2 - B_z^2 & 0 \\ 2B_xB_z & 0 & B_z^2 - B_x^2 \end{bmatrix}. \tag{3.9}$$

Since the y-coordinate is trivial, the trace of the reduced 2×2 matrix is $\mathscr{M}_{11} + \mathscr{M}_{33} = 0$. The 3×3 Maxwell's stress tensor has the following eigenvalues,

$$\lambda_{1,2} = -\frac{B_x^2 + B_z^2}{2\mu_0}, \lambda_3 = \frac{B_x^2 + B_z^2}{2\mu_0}. \tag{3.10}$$

Invoking the similarity of the equation of motion for a viscoelastic fluid and MHD *i.e.*, Eqs. 2.2 and 2.5 from (Ogilvie & Proctor, 2003), we can arrive at the following analogy between the anisotropic stress terms in either system. Namely, comparing Eqs. 3.6 and 3.10 we have,

$$\lambda_3 \leftrightarrow \sigma_{zz} \tag{3.11}$$

$$\text{Or, } \frac{B_x^2 + B_z^2}{2\mu_0} \leftrightarrow \frac{2\text{Tr}(c)\eta_p(c)\dot{\varepsilon}}{3}. \tag{3.12}$$

Note that $\eta_p = \rho\nu_p$, where, ν_p is the kinematic viscosity of the polymeric fluid and we expect it to be also a function of the concentration, c. Also, $\beta = c_s^2/v_A^2$, is the plasma-β and $Ma = u/c_s$, is the Mach number of the plasma flow. We scale the stress terms with the inertial stress represented approximately as the square of the fluid velocity in both cases and compare $\beta^{-1}Ma^{-2}$ (MHD) to $2\text{Tr}\nu_p/(3u_zL)$ (polymeric fluid). In Supplementary Figs. 3.12b, c, we show the variation of the quantify βMa^2 for $B_{\text{imp}} = 0.1, 1$ G, respectively. It is clear from comparing the two panels of this figure with panels of Fig. 1c in the main text that in regions where $\beta^{-1}Ma^{-2} > 1$ are the regions where formation of Kelvin-Helmholtz vortices are suppressed. Although, we do not have an idea of the exact value of Tr, but, intuitively it must depend on the concentration c and experimentally known to be in the range $3 < \text{Tr} < 10^4$ for polymers like PEO. For high molecular weight PEO solutions with $Oh > 1$, Trouton ratios of $\text{Tr} > 10^3$ are known to be realized (Dinic & Sharma, 2019). Let us use the

measured value of $\nu_p = 9.8 \pm 0.1 \times 10^{-7}$ m^2 s^{-1} for 100 ppm PEO solution, and $\dot{\varepsilon} \sim u_z/L$, where $u_z \sim 0.2$ m s^{-1} is the typical tip velocity of the jet and $L \sim 0.02$ m is the maximum height of the jet in Fig.1d. Using the above values the non-dimensional viscoelastic stress, $10^{-3} \ll 2\mathrm{Tr}(c)\nu_p(c)/(3u_zL) < 3$. Therefore, even though the two systems are widely different, and in spite of several approximations, it is surprising that the relative strengths of stresses seem comparable.

3.3.2 Threshold magnetic field for suppression of Kelvin-Helmholtz instability

The panel (e) of Fig. 1 shows an initial monotonic decrease of vortices detected with increasing the magnetic field, B_z, before the curve goes to saturation with no vortices detected. In the Methods section, we also indicate that the algorithm for detection of vortices assumes that the rotation velocity is larger than the expansion or contraction velocity or that circular vortices ($|v_x| \sim |v_z|$) are more likely to be detected. Analysis of the velocity components inside a small region denoted by the green rectangle in Fig. 3.12b gives a value of $|v_x| \sim 1.06|v_z|$ (for $B_{\rm imp} = 0.1$ G and numerous vortices) and $|v_x| \sim 0.11|v_z|$ (for $B_{\rm imp} = 1.0$ G and very few vortices). Also, note that in Fig. 2b, where the horizontal velocity is damped artificially in a 2D solar atmospheric set-up without any imposed vertical magnetic field, the KH vortices are suppressed and we obtain a forest of vertical jets. Let us assume that $|B_x| \sim |B_z|\delta$, with $\delta < 1$ for a dominant vertical field. Focussing on the contribution of the magnetic field, we can write the x-component of the velocity equation assuming only the Lorentz force in the right hand side as,

$$\frac{\partial v_x}{\partial t} = \frac{B_z^2 \tau}{\rho \mu_0} \nabla^2 v_x + \frac{v_x B_z \tau}{\mu_0 \rho} \nabla^2 B_z + \text{other terms of order } \delta. \tag{3.13}$$

To arrive at the above equation, we have additionally used the induction equation (integrated over a time scale τ) to rewrite terms involving $\partial B_x/\partial z$ and $\partial B_z/\partial x$. We note that the first term has the form of a diffusion term and serves to decrease v_x and, further, ignore the second term in Eq. 3.13 as an approximation. Let the shear rate (dv_z/dx) produced as a result of vertical wave driving at the edge of an initial vertical jet be $\sim v_z/d$, where, d is the width of the jet. We take τ also to be the inverse of the shear rate. The diffusion time for v_x must be shorter than the shearing time, for the vortices to elongate vertically from their circular cross section, and no longer be detected, *i.e.,* $|v_x| < |v_z|$. This implies,

$$\frac{B_z^2}{\rho \mu_0 v_z d} > \frac{v_z}{d} \tag{3.14}$$

Let the Alfvén velocity in the vertical direction be $v_{Az} = B_z/\sqrt{\mu_0\rho}$, the plasma beta, $\beta = c_s^2/v_{Az}^2$, and the Mach number, $Ma = v_z/c_s$. Then, Eq. 3.14 can be rearranged to show that in regions where $\beta Ma^2 < 1$, the vortex formation by the shear instability will be suppressed.

3.4 Threshold concentration for suppression of Plateau-Rayleigh instability

In analogy with panel (e) of Fig. 1, panel (f) also indicates that the number of droplets ejected in the experiments decrease with increasing polymer concentration and then goes to zero for concentrations above 50 ppm. This points to the existence of a threshold of polymer concentration beyond which the Plateau-Rayleigh instability (Plateau, 1873) is effectively arrested.

The physical model of the polymer chains in the fluid responding to a flow is as described by (Marciano & Brochard-Wyart, 1995), and Chap 20 of (Young, R.J., and Lovell, P.A, 2011). A rigorous analytical treatment (*i.e.*, by using Langevin dynamics) is non-trivial and depends on microscopic details of the forcing function induced by the flow on beads of a particular polymer chain, *e.g.*, uniform (non uniform) and steady (oscillatory) forcing along its partially coiled length. However, using the macroscopic description that the polymer chains are microscopic springs associated with a single spring constant, and embedded in the fluid responding to and reacting on the jetting flow, we can easily motivate the existence of a threshold concentration.

Without going into the exact spatial profile of the flow inside a jet and an associated mathematically exact analysis, we make certain approximations for calculating the threshold polymer concentration: i) the applied stress is almost constant during the rise phase of the jet; ii) the Maxwell's pot model where there are $\sim c$ springs and pots per unit volume of the fluid (a measure of polymer concentration) each of which can store an energy E_p. In an extensional flow, these elastic springs would absorb energy from the flow and during the relaxation, the energy would be dissipated in the pots. This spring constant depends on the molecular weight and structure of the chain. For a given Faraday amplitude and frequency, let the velocity of a vertical jet (of length, L, and width, d) ejected be v_0 for a non-polymeric fluid. In the presence of extensible polymeric coiled chains, let the corresponding jet velocity be denoted as v_1. And, $\dot{\varepsilon} =\sim v_1/L$ be the strain rate and τ is the rise time of the jet. The viscous dissipation due to the kinematic extensional viscosity, ν_E, is $\sim \rho\nu_E\dot{\varepsilon}^2\tau/2$. Then, we can write

$$cE_p = \rho\nu_E\frac{v_1}{L} \tag{3.15}$$

and,

$$\frac{\rho}{2}(v_0^2 - v_1^2) = \frac{\rho \nu_E}{2}\dot{\varepsilon}^2\tau. \tag{3.16}$$

In the absence of polymers, we expect the jet to have enough energy to overcome surface tension and produce at least a droplet. Therefore, $v_0^2 > 2n\gamma A/\rho V$, where A is the surface area of the droplet, n is the number of droplets the jet disintegrates into, V is the volume of the jet and γ is the surface tension. Upon addition of a small quantity of polymer, the jet no longer has the extra energy to produce even a single droplet. Thus, $v_1^2 < 2\gamma A/\rho V$. By using Eq. 3.16 along with the first inequality involving v_0 we have,

$$v_1^2 + \frac{2cE_p}{\rho} > \frac{2n\gamma A}{\rho V} \tag{3.17}$$

and after rearrangement, for a cylindrical jet, we find a threshold for the polymer concentration, c, given by,

$$c > \frac{\rho v_1^2}{2E_p}\left(\frac{8n\gamma}{\rho v_1^2 L} - 1\right) > 0. \tag{3.18}$$

Most jets in the Faraday experiment, performed at 30 Hz with water, break into $n > 2$ droplets. Using guiding values from the identical experiment with 100 ppm PEO solution prepared using PEO of molecular weight, $M_w[\text{PEO}] = 5000\,\text{kg mol}^{-1}$, we can further calculate, $c \sim 10^{19}$ chains m^{-3}. Substituting the typical measured values of $v_1 \sim 0.2\,\text{m s}^{-1}$, $\gamma = 0.07\,\text{N m}^{-1}$, $L = 0.02\,\text{m}$ in Eq. 3.18 leads to $E_p > 8 \times 10^{-19}\,\text{J}$, which is roughly the energy absorbed by each coiled polymer chain molecule. The typical size of a coiled polymer consisting of $N_p = M_w[\text{PEO}]/M_w[\text{C}_2\text{H}_4\text{O}] \sim 113000$ monomers is given by $R_g \sim 1.3\sqrt{N_p}$ Å~ 440 Å, where 1.3 Å is the size of $\text{C}_2\text{H}_4\text{O}$ – the PEO monomer. In addition to this, we can assume a spring constant of $k = 3k_BT/R_g^2$, with the Boltzmann constant denoted, k_B, and $T = 300\,\text{K}$. The extensional flow, during the rise phase of the jet, can uncoil the chain to $\sqrt{E_p/k} \sim 8$ times the coiled size R_g. There is of course a statistical distribution of energy and extension felt by the polymer molecules in the jet, but here we crudely assume that all polymer molecules absorb the same energy. Further, from Eq. 3.15, we obtain an estimate for the Trouton ratio, Tr, using the measured value for $\nu_p = 9.8 \times 10^{-7}\,\text{m}^2\,\text{s}^{-1}$, namely,

$$\text{Tr} = \frac{\nu_E}{\nu_p} > \frac{2v_1 L}{\nu_p}\left(\frac{8n\gamma}{\rho v_1^2 L} - 1\right) \sim 3200. \tag{3.19}$$

The above value lies in the range quoted at the end of §3.3.1. Using the above analysis along with experimentally observed properties, like threshold concentration, height, width and velocity of jets, we are able to derive some reasonable order-of-magnitude numbers regarding the behaviour of polymer chains in a typical jet formed by Faraday excitation (*i.e.*,

E_p, the energy absorbed by each chain, stretched chain length, Trouton number). This gives us confidence that some aspects of this highly non-linear system can still be understood from such a simple physics based approach.

3.4.1 Determination of $A_{\min}$

In this section, we provide a detailed explanation of the process followed to determine the threshold acceleration, $A_{\min}$ in Figs. 1a-b. We arrive at the plotted data points corresponding to minimum acceleration, $A_{\min}$, at any given frequency, denoted by filled triangles, by performing a sequence of independent runs sampling the vertical acceleration. An imaginary line connecting these filled triangles is the curve of $A_{\min}$ versus f_0 which is the approximate boundary in phase space where the forest of jets criteria starts to apply. In the range of discrete frequencies explored between 3-9 mHz (solar atmosphere) and 15-120 Hz (fluid), therefore the A_0–f_0 phase space is separated by the boundary defined by the data points into two regions–one in which a forest of jets are observed (at and above the data points denoted by filled symbols) and one where our forest of jet criteria is not satisfied (the data points denoted by open symbols). Therefore the transition from a forest to no forest lies somewhere in between the least acceleration filled and highest acceleration open triangles for these frequencies. This process is followed for all the frequencies but the vicinity of the transition is represented in the figure at three indicative frequencies, namely, 3.3, 5.5, and 7 mHz (Fig. 1a for solar atmosphere) and 20, 50, and 105 Hz (Fig. 1b for polymeric fluid) so as to sample the regions R1, R2 and R3. For an illustration of our method of arriving at data points used in Fig 1a, we provide at the 3.3 mHz driving frequency a Supplementary Video 9 of (Dey et al., 2022) of wave driving of the solar atmosphere. This driver corresponds to a vertical velocity amplitude of 0.50 km s^{-1} (panel a) and 0.35 km s^{-1} (panel b). Here, several jets, as characterized by synthetic Si IV emission using an analytical function (see Methods), reach heights ≥ 7 Mm during ten oscillation periods, after the nonlinear development phase, thereby satisfying the forest of jets criteria. Let us compare this to a driving amplitude of 0.25 km s^{-1} (panel c), where five jets, still strongly resembling the driving profile and therefore no nonlinear development, are also seen but reaching heights < 7 Mm during ten periods, thereby failing to satisfy the forest of jets criteria.

Likewise, for Fig 1b, we provide at the 50 Hz driving frequency a supplementary video 9 of (Dey et al., 2022). There, a Faraday excitation runs of 500 ppm PEO solution, corresponding to different vertical peak harmonic accelerations are performed. For a peak acceleration of $4.3g_{\mathrm{E}}$, four jets reach ≥ 0.5 cm length (1.3 cm mark on the scale in the Supplementary Video 9 of (Dey et al., 2022)) in ten oscillation periods, again after the onset of nonlinear development phase indicated by the central jet ejection, and this threshold data point is recorded. Next, with a reduced peak acceleration of both $3.6g_{\mathrm{E}}$ and $4.1g_{\mathrm{E}}$ yields no jet and two jets, respectively,

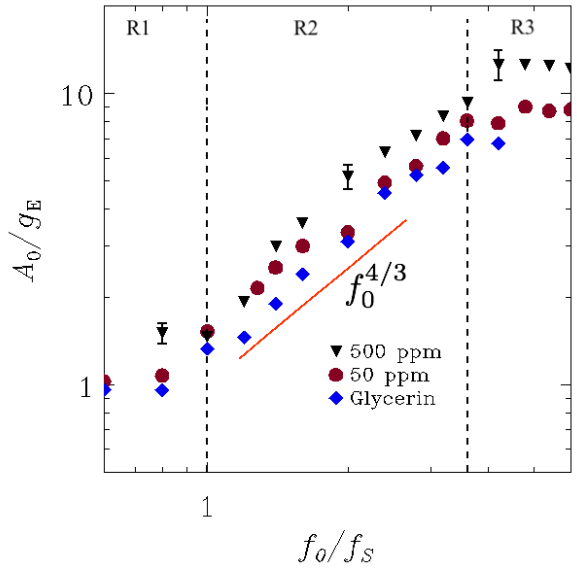

Supplementary Figure 3.13 The A_0–f_0 phase space to represent and compare the variation of threshold accelerations, $A_{\min}$ with driving frequency, f_0. Each filled symbol represents an independent experiment for different fluids, namely, 500 ppm (triangle), 50 ppm PEO (circle) solution and 55% glycerine (diamond). The error bars denote random variations obtained from repeated set of measurements at three different frequencies (20 Hz, 50 Hz and 105 Hz) for the 500 ppm PEO solution. The solid red line shows the $f_0^{4/3}$ dependence obtained for jets by dimensional arguments for a fluid under Faraday excitation (Goodridge et al., 1997).

in the same duration. Further, the variation in repeated measurement of threshold criteria, performed at different times and with different batches of solutions, at three representative frequencies (20 Hz, 50 Hz and 105 Hz for 500 PEO in fluid experiments) are denoted by error bars (9%, 11% and 12%) in the Supplementary Fig. 2. For comparison with experiments with 500 ppm PEO, we also represent data points performed using the same technique as Fig. 1b but for different fluids, namely, 50 ppm PEO (lower polymer concentration and lower viscosity similar to water) and 55% glycerine solution (non-polymeric high viscosity similar to 1000 ppm PEO).

Video 1 **Response of solar plasma to superposition of frequencies**: (a) Synthetic Si-IV emission according to the analytical expression given by Eq. 3.2 from a model driven by a velocity forcing of the form $v_z/V_0 = \sin(2\pi f_1 t)/4 + \sin(2\pi f_2 t)/2 + \sin(2\pi f_3 t)/4$ shown in panel (c), where $V_0 = 1.0\,\mathrm{km\,s^{-1}}$, $f_1 = 3.0\,\mathrm{mHz}$, $f_2 = 3.5\,\mathrm{mHz}$, and $f_3 = 4.0\,\mathrm{mHz}$. The above forcing has only been applied within a layer, $-50\,\mathrm{km} < z < 0\,\mathrm{km}$. (b) Same as (a) but for temperature (in Kelvin).

Video 3.2 Jet breaking in polymeric fluid (PEO, 1000ppm, viscoelastic) versus 55% glycerine solution (viscous) at two different frequencies (a) 120 Hz, and (b) 30 Hz with acceleration amplitudes in terms of local gravity indicated. (c) Polymeric fluids (iodinated 2% PVA, 23% jets reaching heights above 1 cm break) may resist droplet ejection by pinching of jets (due to Plateau-Rayleigh instability) as compared to Newtonian fluids (76% Glycerine solution, 53% jet-breakage above 1 cm) of similar viscosity and surface tension. Both fluids are subjected to similar peak forcing of $10.1 g_\mathrm{E}$ (30 ml fluid in cylindrical container).

Video 3.3 **Nonlinear development in numerical and table-top experiment**: volume rendering of synthetic emission at 15000 K for a three-dimensional numerical simulation of solar plasma forced at the lower boundary with a periodic forcing with a velocity amplitude of $1.32\,\mathrm{km\,s^{-1}}$ and an imposed magnetic field of 10 G (left panel). A polymeric fluid (iodinated 3% PVA solution) subjected to Faraday excitation at 30 Hz and a peak acceleration of $10.1 g_\mathrm{E}$ (right panel). Both the numerical and the table-top experiments show nonlinear development in about five oscillation periods.

Video 3.4 **Mechanism of formation of fluid jets**: View of the free surface of iodinated 3% PVA, as seen at an angle of 20° from the vertical, to show the mechanism for jet forest formation by collision of ridges of neighbouring polygonal cells formed due to interacting surface gravity waves (via nonlinear mode coupling).

Video 5 **Response of polymeric fluid to frequency scaled solar p-modes**: Iodinated 2% PVA (30 ml) placed in a circular container of 0.1 m diameter and responding to frequency-scaled quasi-periodic solar acoustic modes (p-modes from SOHO/MDI) such that the dominant FFT peak lies at 30 Hz. The peak acceleration reaches up to $5 g_\mathrm{E}$. Imaged at 500 fps.

Video 3.6 Synthetic emission at a temperature of 80000 K calculated using the analytical expression of Eq. 3.2 (top panel) and AIA 17.1 nm emission from our numerical simulation (bottom panel). Magnetic fields are shown by red curves.

Video 3.7 **Faraday excitation experiment with paint**: Initially separate red (15 ml) and white (15 ml) paint in a circular container of diameter 0.1 m responding to a 30 Hz harmonic Faraday excitation with a peak acceleration of $7 g_\mathrm{E}$ imaged at 1000 fps. We observe the abundant formation of jet forest, some of which exhibit rotation as visualized by twisted motion of the red and white threads of paint.

Video 3.8 **Lagrangian tracking of the plasma in the spicule forest**: (a) 540000 particles are initially distributed uniformly in six differently coloured layers, each with 1 Mm thickness except the bottom one which is 0.5 Mm thick, between $-0.5 < z < 5$ Mm. (b) and (c) Particles are tracked by local acceleration and vertical velocity to show acceleration fronts energizing the spicular plasma. Black curves in (b) show magnetic field lines whereas the black contours in (c) denote regions of shock. (d) Spicule formation driven by granular collapse in convective plumes, P1 and P2. (e) Spicule formation driven by solar global oscillations and magnetic reconnection (denoted by the white rectangle).

Video 3.9 **Determination of $A_{\min}$ in A_0 versus f_0 phase space**: Part I (solar atmosphere): Spicules formed in response to wave driving of the form $2\pi f_0 V_0 \sin(2\pi f_0 t)\cos(5\pi x/L)$, with (a) $V_0 = 0.5\,\mathrm{km\,s^{-1}}$, (b) $V_0 = 0.35$ and (c) $0.25\,\mathrm{km\,s^{-1}}$, respectively. The dashed line indicates the 7 Mm height. Note that the forest of jet criteria is satisfied for cases (a) and (b) only. Part II (Polymeric fluid): Jets formed in response to Faraday excitation with peak accelerations, A_0 as (a) $4.1g_{\mathrm{E}}$, (b) $3.6g_{\mathrm{E}}$, (c) $4.3g_{\mathrm{E}}$, and (d) $4.7g_{\mathrm{E}}$. The dotted line denotes the 1.3 cm mark on the scale. Only (c) and (d) satisfy the forest of jets criteria.

4

Dynamics of solar spicules in the presence of swirls

The dynamical complexity of solar spicules is one of the fascinating areas of research in connection with their potential contribution to the solar corona. In this direction, the advancement of high-resolution ground, space-based observation with extremely good temporal resolution opens new paths of exploration. During the rapid evolutionary phase of solar spicules, transverse oscillations of spicular strands relative to their axes (De Pontieu et al., 2007b, 2012; Kuridze et al., 2016; Bate et al., 2022), bulk spinning motions (Suematsu et al., 2008b; Antolin et al., 2018) motions are most prominent apart from the rising or falling motion in the solar atmosphere. The observed transverse swaying motion is interpreted as a manifestation of propagating nearly incompressible magnetohydrodynamics (MHD) kink waves and spicules act as wave guides to transfer these modes. While the spinning motion, though still debated, is believed to be either due to torsional Alfvén waves (Sekse et al., 2013; Antolin et al., 2018), or because of mini-filament eruption (Sterling et al., 2010b, 2020) or due to emerging new magnetic flux reconnecting over an active region (Danilovic, 2022). Apart from the solar limb images, the torsional motion of spicules is independently confirmed by the Doppler shift measurements, observed at the off-limb position. With instruments like CRISP, an imaging

SpectroPolarimeter of the Swedish Solar Telescope (SST), and Monte Carlo simulations (De Pontieu et al., 2007b), transverse and torsional speeds are separated out and quantified as 15–20 and 25–30 km/s (Sekse et al., 2013) respectively. By analyzing a sequence of data cubes at a high cadence of 2 s from a high spatial resolution rMHD simulation of the solar atmosphere, we detect several spinning clusters of spicules that are often reported in solar atmospheric images taken in the Ca II H line from the Broadband Filter Imager (BFI) instrument on-board the Hinode spacecraft (Rompolt, 1975; Pishkalo, 1994; Suematsu et al., 2008b; Zaqarashvili & Erdélyi, 2009).

The data from our three-dimensional radiative MHD simulations self-consistently mimic most of the observed dynamic features of spicules. The spike-like line-of-sight (LOS) integrated jets in our simulations have the characteristics of observed spicules since these coherent plasma features have a lifetime of 5-10 mins, vertical speeds of 20–70 $\mathrm{km\,s^{-1}}$, heights 6–16 Mm, widths 200–1500 km and their tips follow a parabolic path with time.We also find similar properties of the synthetic spicules in our 2-dimensional model (Chapter 4). This simulated forest of jets is excited in the presence of solar convection in a layer below the photosphere. With an imposed vertical magnetic field of $B_0 = 7.5$ G, reminiscent of the large scale polar field of the Sun, in a gravitationally stratified medium, photospheric magnetic fields are amplified to ~ 500 G by twisting and stretching motions of turbulent plasma blobs. Magnetic fields often form expanding flux-tube structures (Fig. 4.1 a), anchored at intergranular lanes of the photosphere. There are strong shear motions in these downflow lanes due to the relative motion of adjacent convective granules. Hence the fluxtubes are continuously perturbed by these turbulent motions and generate myriads of MHD waves in the atmosphere. When hot plasma blobs as granules emerge at the photosphere, magnetic fields are also advected with the plasma flow. The topology over the granules resembles the shed-like structure, due to the dominating horizontal component of the magnetic field as advected with rising hot granular cells (Fig. 4.1 b). Although the coronal magnetic field remains almost vertical and the strength remains close to the imposed vertical field. Such large-scale open magnetic environments resemble solar coronal holes and quiet sun regions. Apart from the imposed magnetic field, there is no additional flux emergence from the convection zone. Therefore the possibility of occurring magnetic reconnection in the solar atmosphere becomes unlikely.

4.1 Morphology of Spicules as warped plasma sheets.

We present a volume rendering of synthetic emission from plasma at 80000 K (Fig. 4.2 a–b), comparable to optically thin Si IV UV filter. This filter is mostly sensitive to the features of the solar transition region. The technique to present synthetic emissions of spicules in the 3D

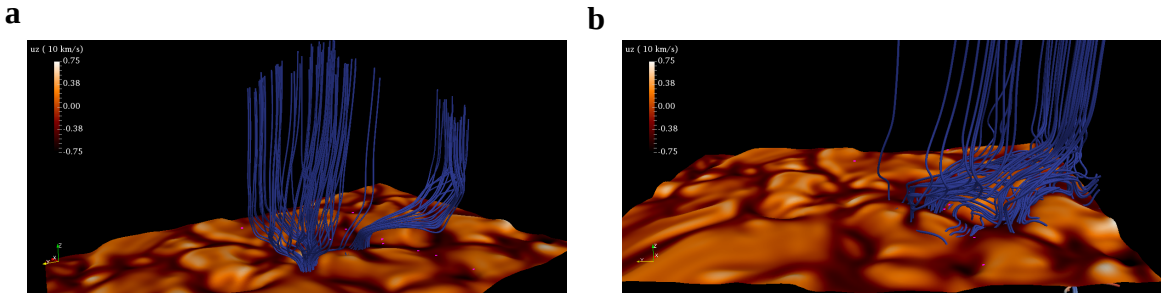

Fig. 4.1 Examples of various magnetic field topologies in the solar atmosphere. (a) expanding fluxtube structure is rooted at the intergranular lanes of the photosphere (shown using $\tau = 1$ isosurface) (b) dome-like morphology is present over the convective granules

model is exactly the same as their 2D counterpart, as discussed in Chapter 3. Here spicules appear as pleated drapery of compressible plasma, in contrast to a standard view of jets with tube-like geometry. To make the pleating visually clear, a subdomain of Fig. 4.2a sliced at $z = 10$ Mm is shown in panel (b). Laboratory fluid experiments discussed in the last chapter also point to such morphology of jets (Dey et al., 2022). A fluted sheet-like topology for spicules has been observationally conjectured (Judge et al., 2011, 2012; Lipartito et al., 2014), although the dense plasma sheets reported here are not tangential discontinuities due to the presence of current sheets. Similarly, a coronal veil hypothesis has also been put forward for overlying bright coronal loops above a simulated emerging active region (Malanushenko et al., 2022). Synthesized Hα animations of on-disk chromospheric fibrils from a similar rMHD simulation have the appearance of a crumpled veil (Danilovic, 2022) in the presence of rapid photospheric magnetic flux emergence. Therefore irrespective of the magnetic flux emergence, the morphology of spicules persists to be warped sheet structures.

Here one can also see that the compression fronts due to the slow MHD wave mode (iso-contours of Fig. 4.3) dominate above spicules and therefore accelerate the spicule plasma at successive layers to move upwards. Slow MHD waves can propagate along the magnetic fields and their amplitude ($\Omega_{\rm slow}$) is determined, following Khomenko et al. (2018).

$$\Omega_{\rm slow} = \mathbf{n}_{\parallel} \cdot \boldsymbol{\nabla} \left(\mathbf{n}_{\parallel} \cdot \mathbf{U} \right) \tag{4.1}$$

Here $\mathbf{n}_{\parallel}$ is the unit vector along the magnetic field. We find at further higher heights, these compression fronts become shock fronts with supersonic speed due to strong density stratification and they detach from spicules subsequently. We will discuss the nature of these shock fronts in Appendix .

We will now discuss another observational aspect of spicules, tip brightening (Pereira et al.,

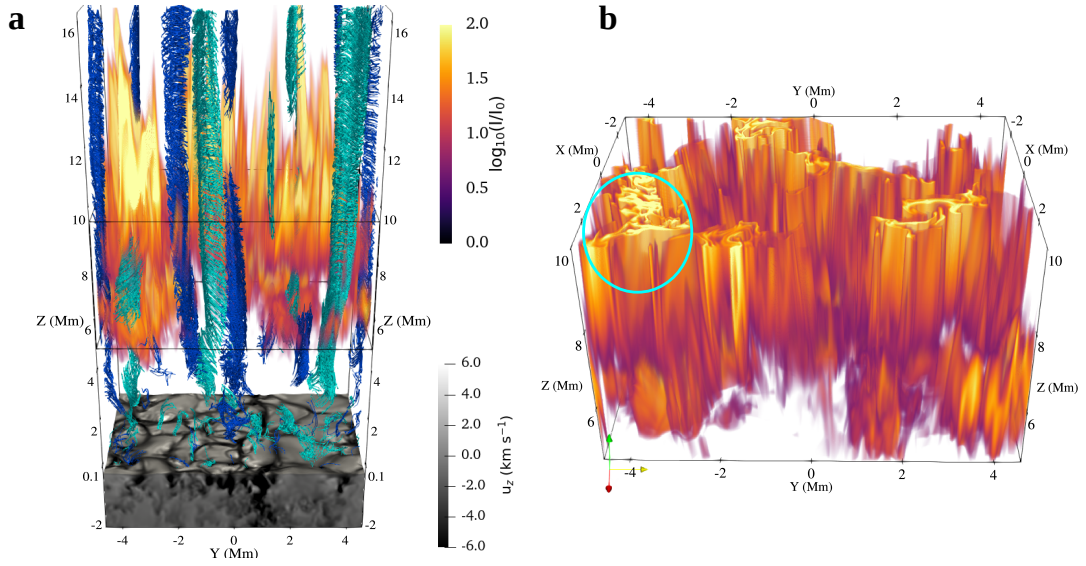

Fig. 4.2 Spinning cluster of solar spicules from simulation and observation. (a) Volume rendering of synthetic plasma emission at 80000 K (similar to Si IV channel) with orange iso-contours and streamlines of CoSCos with both clockwise (cyan) and anti-clockwise (blue) rotational sense. Part of the turbulent convection zone (up to the visible photosphere) is shown as a grey scale block, colour coded by vertical plasma velocity. (b) Same as panel (a) but with a smaller subvolume (black box of panel a), showing the pleated curtain like morphology of spicules. The ratio of intensity of the synthetic emission between the brightest and the dimmest region of the visible sheet is a factor of 10.

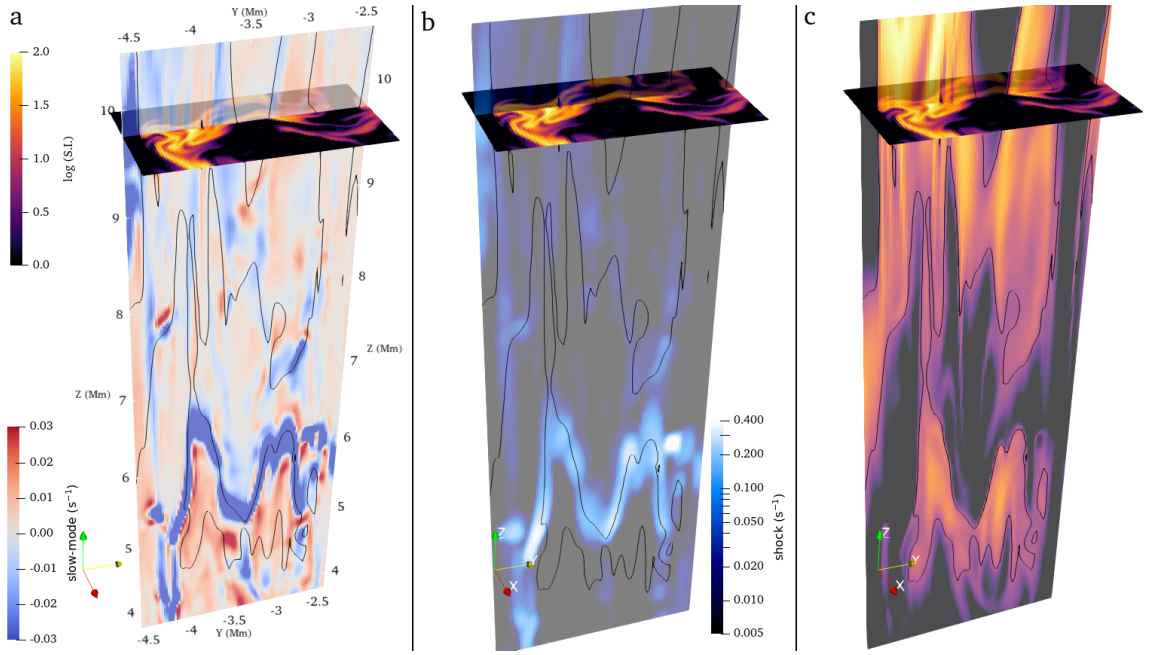

Fig. 4.3 Association of the slow MHD shock fronts with spicules. (a) Amplitude of the slow MHD mode is shown in the vertical plane and cross section of synthetic intensity of spicules at $z = 9.5$ Mm is shown in the horizontal plane. Black contours demarcate the boundary of synthetic spicules. (b) same as panel (a), except the shock compression profile ($-\nabla \cdot \mathbf{U}$) is represented in the same vertical plane instead of slow MHD mode (c) synthetic intensity of spicules is rendered in the vertical plane.

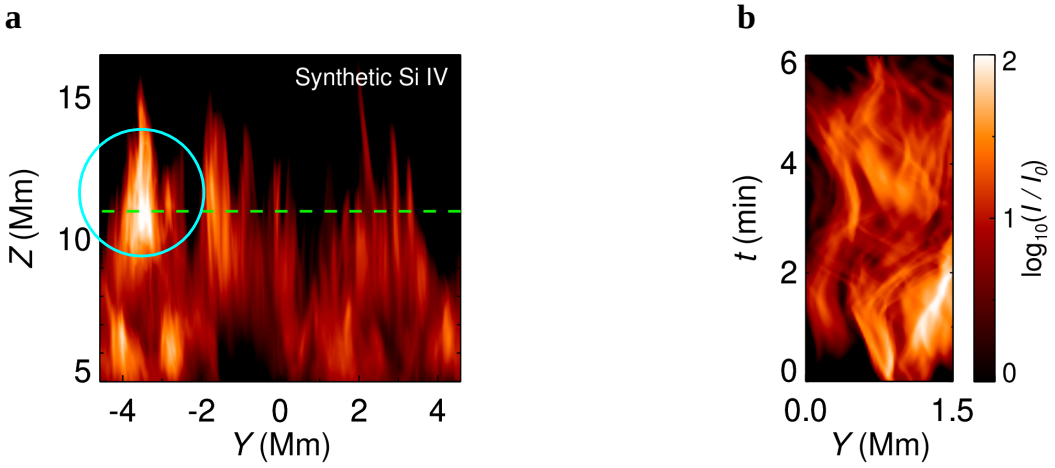

Fig. 4.4 (a) Line-of-sight integration realization of the same set of spicules, shown in Fig. 4.2(b). The bright region encircled by the cyan circle has been obtained by an LOS integration over the densely pleated region of the same panel, also indicated by a cyan circle. (b) Time-distance diagram of synthetic spicules at $z = 11$ Mm, using a horizontal slit (green-dashed line of panel a).

2014). Often the enhancement in the tip intensity, observed in chromospheric lines, is associated with spicule heating and their contribution to the heating of solar coronal. In our 3D rMHD model, we notice the brightness of this drapery of plasma structure is highly non-uniform as seen in synthetic Si IV/80000 K emission, particularly enhanced in the regions with several pleats of the spicular sheet. (encircled by ellipses in Fig. 4.2b). While the simulated spicules present a drapery-like morphology in 3D, the line-of-sight (LOS) integrated 2D profiles still provide the perception of spikes that appear brighter than ambient (panel a of Fig. 4.4). Since the line-of-sight integration takes into account several folds of drapery, we believe the enhancement in the intensity is due to the accumulation of plasma material there. For quantitative analysis, we further compute the relative density and temperature of spicules compared to the horizontal averaged density and temperature values in the same height of the atmosphere (Fig 4.5). It is clearly evident that spicule tips are mostly comprised of denser and simultaneously cooler plasma than the neighborhood. Hence the excess plasma emission from synthetic spicules is solely due to the enhancement in plasma density. In order to study the transverse spicular motion in the solar atmosphere, we view the LOS integrated synthetic intensity using a horizontal slit as shown in Fig. 4.4a. The appearance of braid-like features in the time-distance domain (panel b of Fig. 4.4), is a clear signature of multiple threads of spicules crossing each other. The crossing can either be due to two neighboring threads, each undergoing an independent transverse kink oscillation, or due to spinning. We combine this with the animation of the volume rendering of the plasma drape showing signs of stretching and curling when seen from

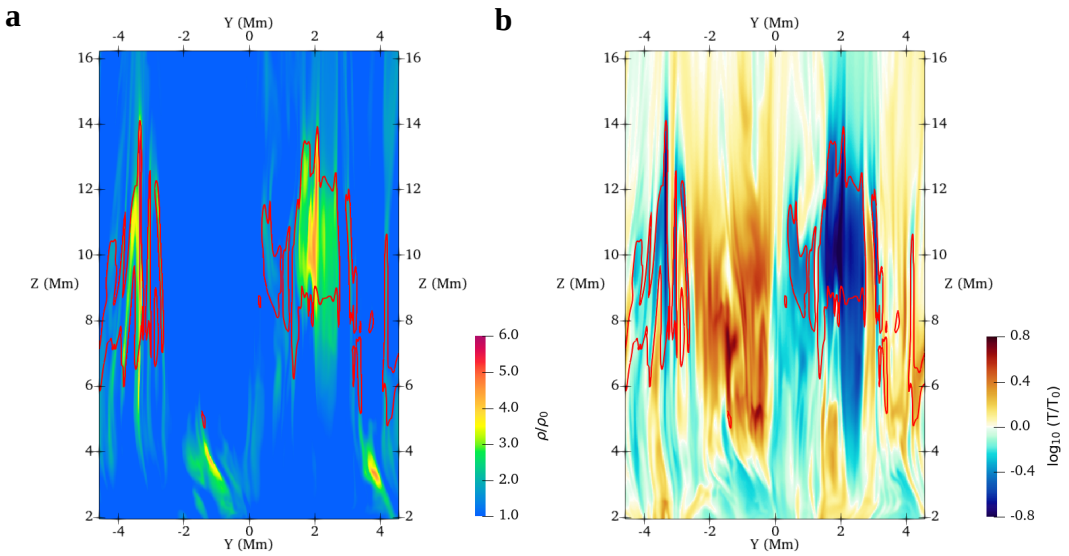

Fig. 4.5 Density (a) and temperature profile (b) of spicule tips relative to the horizontally averaged (over 6 Mm x 9 Mm) density $\rho 0$ (z) and temperature T0 (z) at x=constant plane. Red iso-contours enclose parts of the brightest intensity regions ($\log(I/I_0) > 1$) of the synthetic spicules.

an angle to conclude that the spicules are indeed spinning and not just undergoing independent kink motions. In the images taken at the solar limb, sometimes a spicule is seen splitting into multiple strands. The reverse, where several strands in a bunch appear to join together into a single spicule during the course of spinning is also reported in observations (Suematsu et al., 2008b; Sterling et al., 2010a). Here, we demonstrate that this multi-threaded appearance of spicules is the result of a line-of-sight (LOS) integration of a dynamic drapery-like plasma sheet. The LOS integration of volumetric plasma emission along different angles relative to the X-axis shows that spinning multiple strands that are actually part of the same plasma sheet can present an impression of splitting and merging(Fig. 4.6). To compare and put in context with our rMHD simulation data, we investigate a set of observed images of solar spicules from the Hinode satellite (Kosugi et al., 2007). Here is a comprehensive description of the satellite and onboard instruments and associated calibration techniques.

4.2 High-resolution observations from Hinode Satellite

Hinode is a global space-based Solar mission led by Japan, United States, Europe and United Kingdom. Hinode satellite consists of state-of-the-art observation components which can observe solar photosphere, dynamic and highly structured chromosphere and corona. There

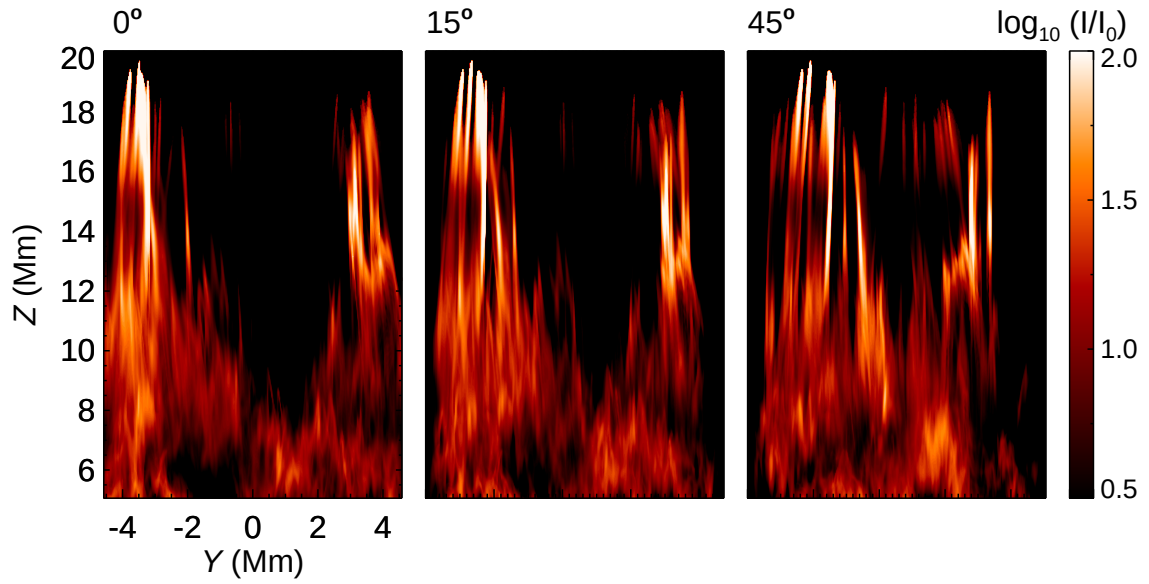

Fig. 4.6 Simulated forest of spicules as seen from different LOS angles. LOS integration is performed along the (a) x-axis of the domain, (b) 15° and (c) 45°, to the x-axis, respectively, to demonstrate how the multi-threaded structure and apparent synthetic intensity of spicule tips change with the viewing angle.

are three instruments on board the Hinode satellite, Solar Optical Telescope (SOT), Extreme Ultraviolet Imaging Spectrometer (EIS) and X-Ray Telescope (XRT). With CCD, spectro-polarimetric instruments, and imaging in narrow and far band filters, it becomes an ideal instrument to study small active regions, and transient features in the atmosphere, e.g., coronal mass ejection, solar flare. Here we will focus on the SOT instrument which has four units, The Broad-band Filter Imager (BFI), The Narrow-band Filter Imager (NFI), The Spectropolarimeter (SP), Correlation Tracker (CT). The Broad-band Filter Imager with an aperture of 0.5 m, can capture wide-band images (0.3–0.8 nm linewidth) in several optical channels between 388 – 668 nm. Among six channels, Ca II H line ($\lambda = 396.85$ nm and width = 0.3 nm) is sensitive to the solar chromospheric height. With a diffraction-limited resolution of 0.0541 arcsec/pixel and the highest cadence of 3.4 s, BFI can cover an area of 218×109 arcsec^2 in the plane of sky.

4.2.1 Filtering of Hinode SOT-BFI images:

We obtain Level-1 Ca II H BFI images from the SOT instrument, after performing `fg_prep.pro` (available under SolarSoftWare suite written in IDL) operation on the raw images as part of the calibration.

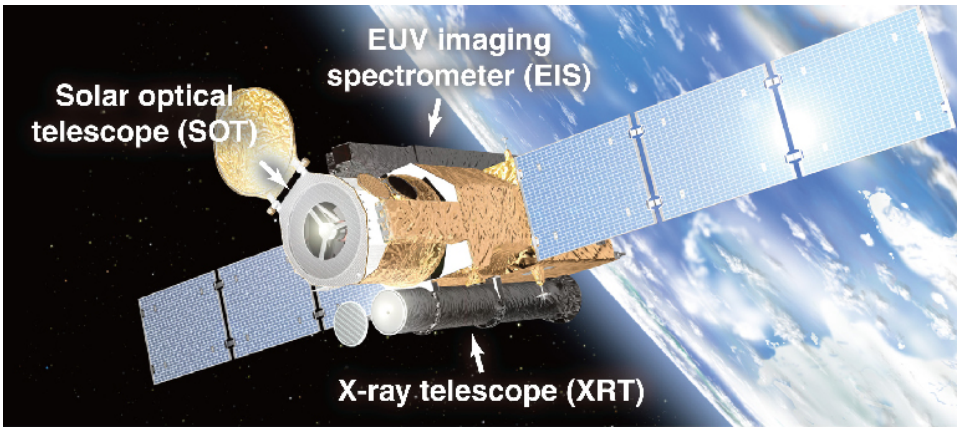

Fig. 4.7 A representation of the Hinode satellite, showing its scientific instruments (SOT, EIS, XRT). source: https://www.nasa.gov/mission_pages/hinode/instruments.html

To increase the brightness of spicular strands over the background, we utilize a radial filtering technique on the calibrated images. We first compute the non-dimensional weight factor as the ratio of intensity at each pixel to the average intensity over all pixels lying on the arc, parallel to the solar limb. After performing the same operation on all radii, we multiply the Level-1 intensity map with the square of the weight factor at every pixel. This filtering process makes relatively brighter (dimmer) pixels to become more brighter (dimmer) than before and hence it enhances the visibility of the spicule forest relative to the surroundings.

4.3 Comparison of observed solar spicules with their simulated counterparts

We analyze an observed dataset of $111'' \times 111''$ images of a region near the northern polar coronal hole taken on 07 Nov, 2007 (Judge & Carlsson, 2010) by the Broadband Filter Imager (BFI) of Solar Optical Telescope (SOT) instrument (Tsuneta et al., 2008; Suematsu et al., 2008a). A 56 min long observation sequence is used when the instrument was pointing towards the limb. We select five instances, where the bulk spinning motion is most discernible during the observation duration. Although there are many such examples of rotating bunches of spicules within the duration. The horizontal extents subtended on the plane of the sky by the spinning bunches vary between 2–4 Mm. For each of these cases, we construct a time-distance map as seen through a slit placed locally parallel to the solar limb. One such case is shown in Fig. 4.8b and the other four examples are in Fig. 4.9a. For comparison, we show the time-distance diagram of simulated and observed bunches of spicules (Fig. 4.9) together. In Section 4.4, we will describe the physical mechanism behind the spinning motion and analyze the above figure

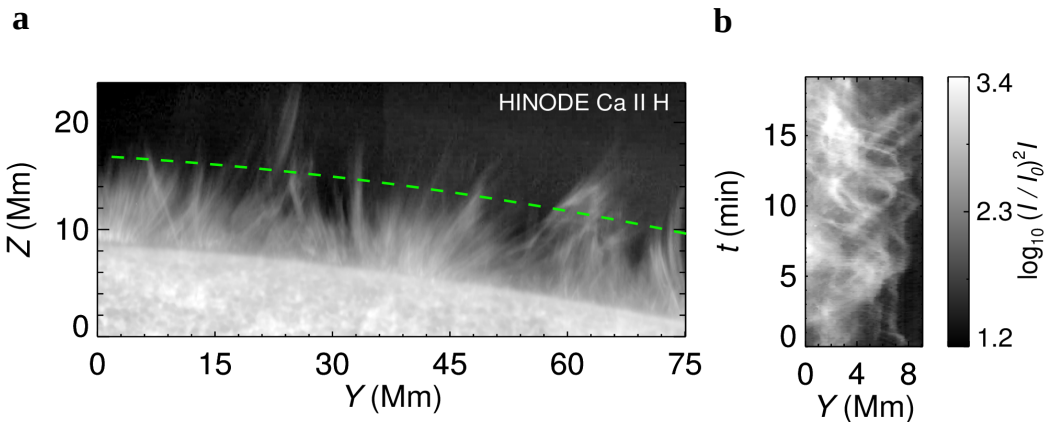

Fig. 4.8 Identification of spinning spicules in using time-distance diagram: (a) SOT–Ca II H filtered image of solar spicules at 19:11:37 UT on 2007 November 7. (b) Time-distance diagram of spinning spicules at 8 Mm height in the solar atmosphere, using a slit parallel to the limb (green-dashed line of panel e).

quantitatively for further insights.

High spatial resolution observations in the blue wing of Hα on the solar disk have shown signatures of rapidly developing vortex-like features in spicules (Kuridze et al., 2016).

A vortex is a rotating fluid structure, observed ubiquitously in various astrophysical scenarios. In the sun, they are rotating plasma column elements, often referred to as vortex tubes or swirls. These ubiquitous features are observed in various levels of the atmosphere,e.g., intergranular lanes of the convective granules (Wang et al., 1995; Bonet et al., 2008; Liu et al., 2019), and highly inhomogeneous chromospheric regions(Wedemeyer-Böhm & Rouppe van der Voort, 2009; Wedemeyer-Böhm et al., 2012; Tziotziou et al., 2018; Shetye et al., 2019; Liu et al., 2023), and are believed to be extended to the solar corona by coupling different layers of the atmosphere. Optical tracking of plasma motion, indirect tracing of the logarithmic motion of magnetic bright points, high-resolution solar atmospheric images reaching the diffraction limit of telescopes along with spectroscopic data reveal a broad spectrum of characteristics of swirls, such as size, lifetime, rotating speed, vertical plasma motion. Lateral motion of an initial dense cylindrical flux tube can induce Kelvin-Helmholtz instability (KHI) that has been shown analytically (Barbulescu et al., 2019) as well as using MHD simulations (Terradas et al., 2008; Antolin et al., 2018). The above scenario is similar to the case of a flow around a bluff body, where, the velocity shear at a no-slip boundary causes boundary layer inversion and subsequently leads to the accumulation of small-scale vortices ($\ll$ size of the body) and a thickening of the boundary layer (Batchelor, 2000). If the Reynolds number corresponding to transverse velocity is > 80 (Kundu & Cohen, 2008), then it can also lead to Alfvénic vortex shedding (Gruszecki et al., 2010) for sub-Alfvénic speeds. Compressibility is not an essential

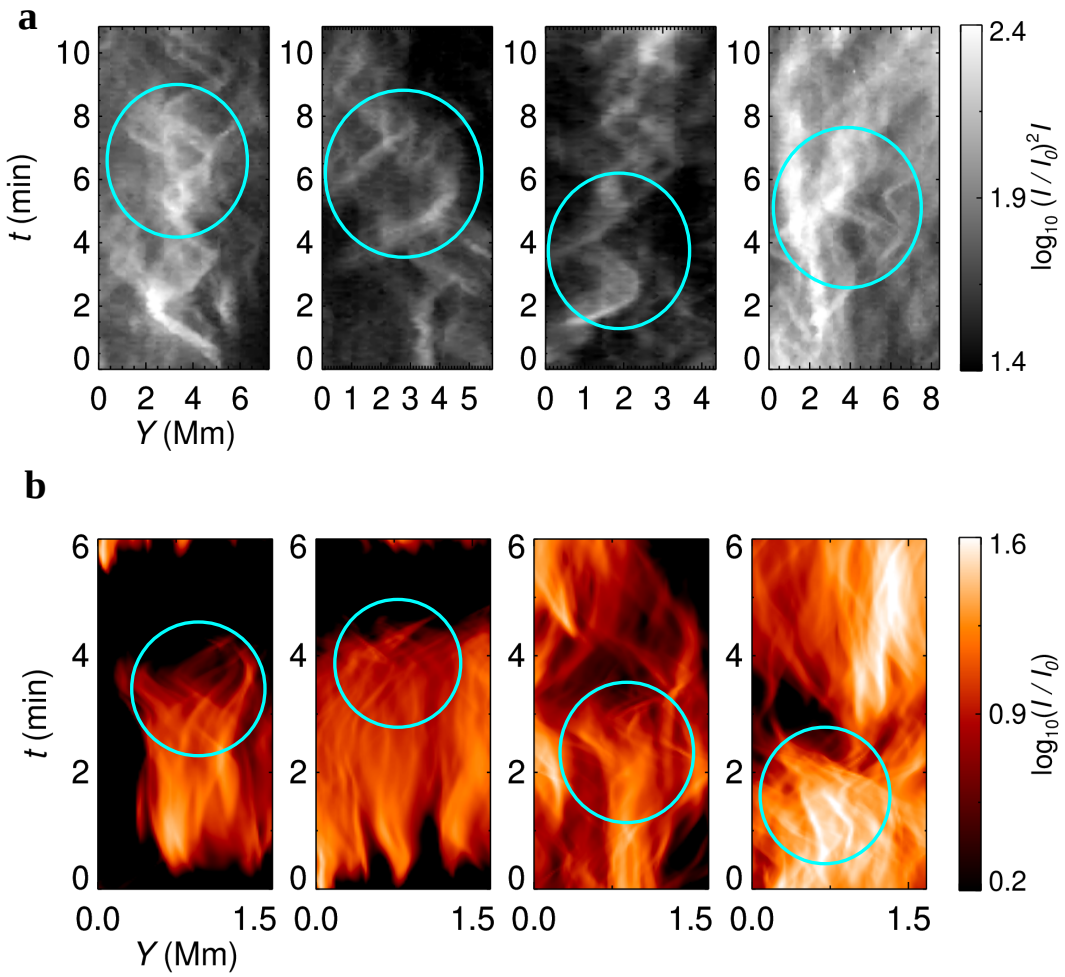

Fig. 4.9 Identification of spinning spicules in observations and simulations using time-distance diagrams. (a) Scaled Ca II H/SOT intensity as seen through four different horizontal slits placed $z = 8$ Mm above and parallel to the observed solar limb similar to Fig. 4.8a to capture several examples of spinning clusters. Encircled regions (cyan) show the crossing of spicule strands, a feature of spinning clusters of spicules. (b) Similar to panel (a), but for synthetic spicules seen through a slit at $z = 11$ Mm at four different times.

condition here, and for any non-zero viscosity, the vorticity at the boundary will eventually diffuse across the domain, outside the cylindrical tube.
In our simulations, we identify several highly dynamic and helical velocity streamlines tracked with the Automatic Swirl Detection Algorithm (Liu et al., 2019) (see the appendix) inside 3D data cubes sampled at a cadence of 2 s. We introduce the term – coronal swirling conduits (CoSCo)– for the stream tubes since they are rather tall, cylindrical, with widths comparable (factor of 0.5) to spicule widths in the range 300–600 km, rotational speed of 2–20 km/s and, have an average lifetime of 20–120 s (Fig. 4.14a and Fig. 4.15a for velocity streamlines indicating CoSCos). Along its entire length, the CoSCos are either clockwise or anti-clockwise. In the entire domain, we find an almost equal presence of them, therefore net zero kinetic helicity ejection to the upper atmosphere. This is because of the absence of any inherent mean rotational profile in the model. Statistically, we notice that approximately 75% of all CoSCos detected in snapshots covering a duration of 10 min are also noted to be hotter than the average temperature inside the spicules by a factor of 2.0–5.0 (Fig. 4.10). Similar characteristics are reported in recent observations as excess intensity in the core regions of the chromospheric swirls . Furthermore, the ASDA captures numerous CoSCos in the corona and far fewer in the chromosphere below.

4.4 Interplay between Spicule–CoSCo

The CoSCos are seen forming mainly at the edges lining the spicules and in turn modify the surrounding flow propelling the spicules to rotate. The synthetic spicules are seen to rotate noticeably during their end-of-life. A spicule can rotate easily in its falling stage when most of the mass has drained towards the surface than in the rising phase when the mass flux is strong and upwards. This demonstrates the role of the inertia of the spicular plasma in their dynamics. Most of the CoSCos have minimal overlap with spicules during most of their lifetime and along their height. However, occasionally, we find swirls that rotate the adjacent spicules by moving inside them. From the perspective of MHD waves, the Alfvén wave power is dominant (Fig.4.11) inside CoSCos. This is expected since by definition the Alfvén wave amplitude is proportional to $(\boldsymbol{\nabla} \times \mathbf{U})$ and CoSCos are regions where the vorticity component along the magnetic field is strong.

$$\Omega_{\text{Alfven}} = \mathbf{n}_{\parallel} \cdot (\boldsymbol{\nabla} \times \mathbf{U}) \tag{4.2}$$

Although the dissipation mechanism of these MHD wave modes at heights > 26 Mm is beyond the scope of our current model. This kind of swirl generation, attached to spicules, exists in our simulation without any prior assumption about either the geometry of the spicule or the properties of its oscillation modes. In order to estimate the rotation velocity and lifetime

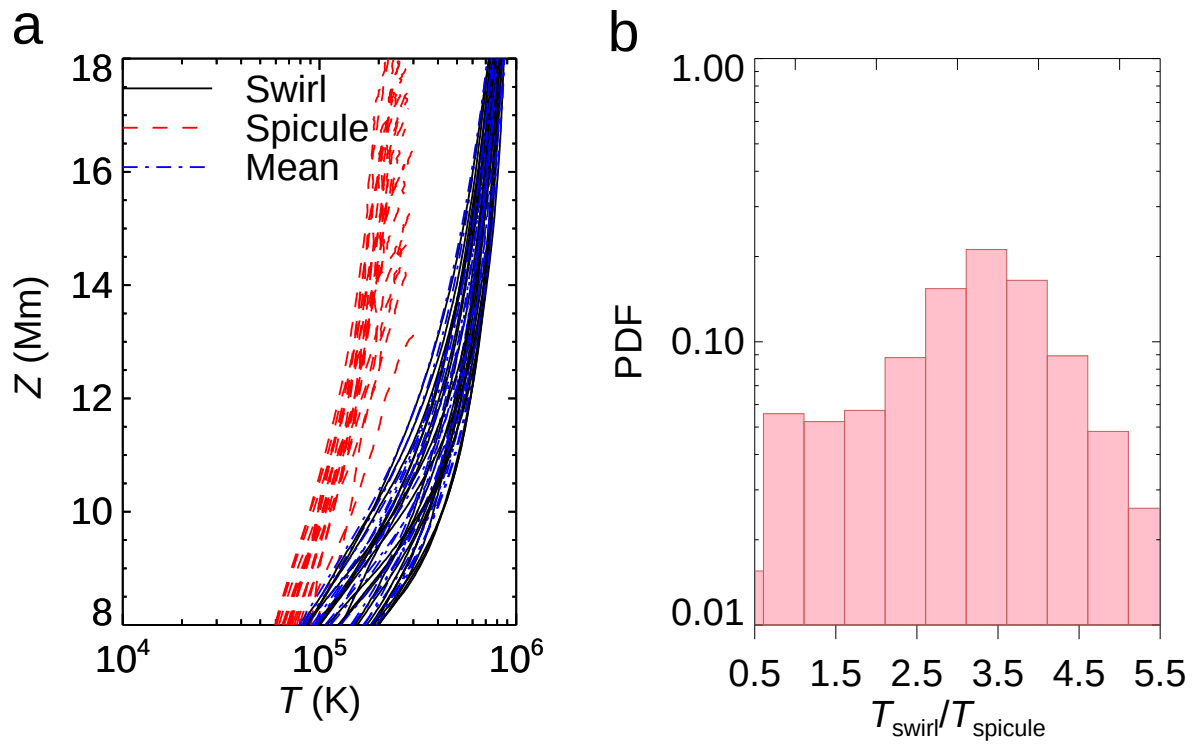

Fig. 4.10 Temperature distribution of spicules and CoSCos, measured for a duration of 30 min of solar time from Run 3 of Table 4.1. (a) Variation of horizontally averaged temperature profiles of CoSCos (black-solid), spicules (red-dashed) and the entire numerical box (blue-dashed dot) over different heights, computed at every 30 s. (b) Probability Density Function (PDF) of temperature of CoSCos relative to the horizontally averaged temperature of spicules in the same region.

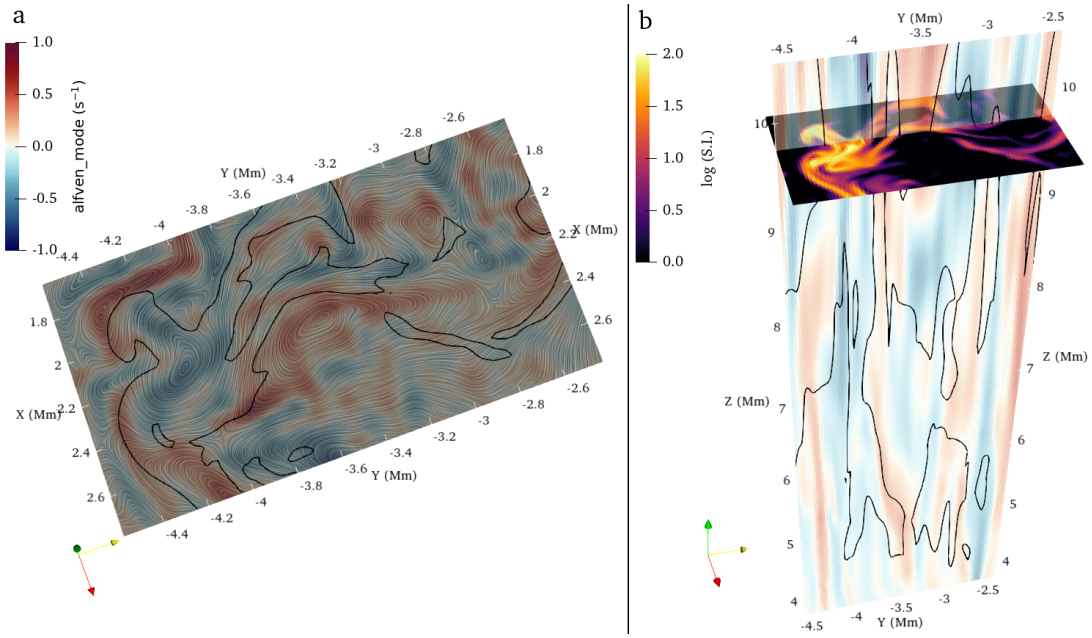

Fig. 4.11 Presence of Alfvén waves in the solar atmosphere. (a) Horizontal plasma velocity is visualized using the LIC technique and shown in the horizontal plane ($z = 9.5$ Mm) shaded by the amplitude of the Alfvén mode (obtained by computing $\mathbf{n}_{\parallel}.(\boldsymbol{\nabla} \times \mathbf{U})$, where $\hat{\mathbf{n}}$ is the unit vector along the magnetic field) and spicules are represented using the black iso-contours. (b) Synthetic intensity of spicules and the wave amplitude (colorbar same as panel a) are shown in vertical and horizontal planes, respectively.

of the spinning phenomena, the time-distance maps corresponding to spicule rotation from observations (simulations) are given in the top (bottom) row for several events in Fig. 4.9. Notable differences are i) that the number of thread crossings in the observed time-distance maps is more than in the synthetic case, ii) the spatial scale of the tangled motion of spicular strands is around 2.0–4.0 Mm in Hinode observations but 0.5–1.0 Mm in our numerical model. Simulated jets are much more closely bunched due to imposing a vertical field in the domain. In reality, the field would be vertical only in network regions (supergranules) that are further apart. If a larger domain with the same resolution is taken, then it is possible to observe spicule bunches of larger widths, iii) the time between two successive crossings is 1–4 min in observations as compared to 0.5– 2 min in our simulations. This indicates that the spicule bunches take longer to spin but complete several spins during their lifetime on the Sun than in the simulations. The likely reasons could be i) in the synthetic case, the CoSCos are seen forming near the end-of-life of spicules. This may be because the CoSCo rotational energies are lower than observed, and ii) a larger domain size could support a bigger CoSCo with longer lifetime which could not be captured by a horizontal extent of $6 \times 9\,\mathrm{Mm}^2$. Features such as chromospheric swirls, and magnetic tornadoes, were also found by other independent simulations (Finley et al., 2022), a few of them with the top boundary extending till the upper chromosphere only (Kitiashvili et al., 2011; Shelyag et al., 2011; Yadav et al., 2021; Battaglia et al., 2021). A complementary mechanism in which spicule matter can be lifted upwards by swirls has also been suggested (Scalisi et al., 2021). Although many of the CoSCos appear at the spicule periphery when the spicular plasma is falling back to the chromosphere, a few form while plasma is still shooting upwards. Such swirling conduits are directly associated with the spicules. For the underlying physical process behind swirling motion, we will perform the vorticity analysis for the magnetized plasma medium.

4.4.1 Vorticity sources in MHD

Vorticity ($\omega = \nabla \times v$) is a measure of rotation and shear effect of fluid and plasma mediums. The time evolution for the enstrophy ($\omega^2/2$) for only the vertical component of vorticity is described by Eq. 4.3 with relevant physical sources indicated. We write the equation for positive definite enstrophy instead of vorticity as the positive (negative) rate of change of enstrophy

denotes regions of increasing (decreasing) swirling or shearing.

$$\frac{\partial}{\partial t}\left(\frac{\omega_z^2}{2}\right) = \omega_z \hat{z}.\Bigg[\underbrace{-(v.\nabla)\,\omega}_{\text{advection}} \underbrace{-\omega\,(\nabla.v)+(\omega.\nabla)\,v}_{\text{tilt+stretch}} \underbrace{+\frac{1}{\rho^2}\nabla\rho\times\nabla\,(p_g+p_m)}_{\text{baro-pressure}} \underbrace{-\frac{1}{\rho^2}\nabla\,\rho\times\left(\frac{B.\nabla B}{\mu_0}\right)}_{\text{baro-tension}} \underbrace{+\frac{1}{\rho}\nabla\times\left(\frac{B.\nabla B}{\mu_0}\right)}_{\text{tension}}\Bigg] \tag{4.3}$$

The first term on the right-hand side of the equation 4.3 denotes the advection of already existing vortices from a neighborhood region by plasma flows. The second term is known as vortex tilt-stretching term for a compressible fluid which determines how a vortex tube can be stretched or tilted by the flow. Next, the baro-pressure term is proportional to the misalignment between the gradient of density and total pressure (gas + magnetic). Baro-tension is also a source which depends on the the misalignment between the density gradient and magnetic tension force. The rotating flow is the result of the density and pressure gradients trying to align in a bid to reach equilibrium. The last term is known as tension term which solely depends on the nature of the magnetic tension force. For our analysis, we combine both baro-pressure and baro-tension components into a single baroclinic term as the density gradient is associated with both of them. Here, we neglect the contribution of viscous diffusion of vortex filaments as their typical magnitude is 0.01–0.1 times smaller than the baroclinic component inside CoSCos. In our calculations, we only consider regions with swirls and not those with large shear flows which can also lead to large ω_z. It is achieved by masking regions of existing swirls with ASDA technique and then computing vorticity sources there.

4.4.2 Classification of CoSCos

According to the dominant vorticity sources, CoSCos may be classified into two categories. First, the CoSCo-I, or magnetic tension driven swirls, whose origin may not be directly correlated with spicules. They are characterized by oppositely directed velocity and magnetic field perturbation in horizontal components and co-spatial magnetic and velocity swirls. In our coarse grid simulation, Run 1 (Table 1), carried out in a larger domain, we find four cases of CoSCo-I reaching till the photosphere (see, Fig. 4.12). In Run 2, we clearly spot a tall CoSCo-I (1–18 Mm) rotating without any spicule activity nearby 4.13. The velocity streamlines have a collimated cylindrical geometry for $z > 6$ Mm whereas they resemble tapering funnels below.

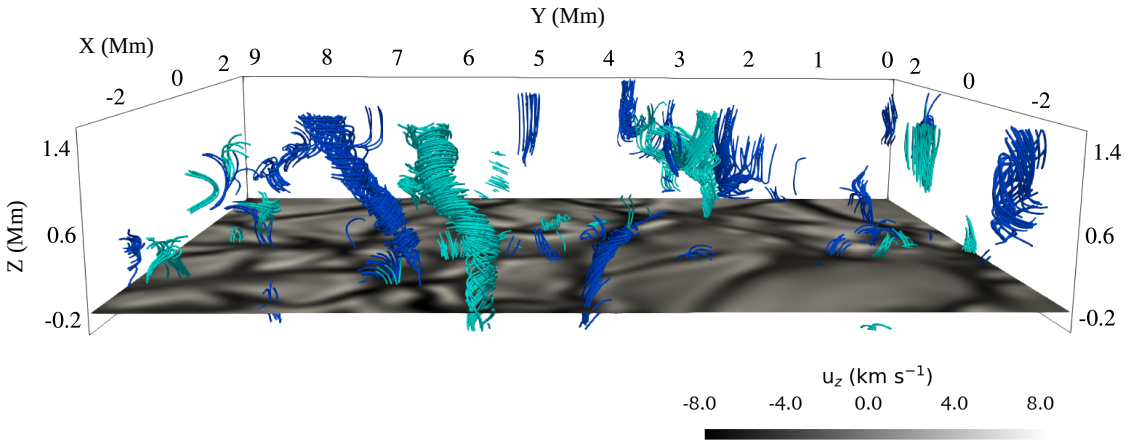

Fig. 4.12 Examples of CoSCos, deeply rooted at the convective down-flow lanes of the solar photosphere. Velocity streamlines of CoSCos are shown in cyan (blue) lines, corresponding to clockwise (anti-clockwise) rotating plasma flows. The above numerical experiment corresponds to the Run 1 of Table 4.1.

An exemplary case of spicule rotation is further detected in the fine grid simulation, Run 3 of Table 1, where the leftward horizontal movement of a spicule is first modified or stalled by a passing shock. Afterward, we identify a swirl as shown in Fig. 4.14a at the periphery of the spicule before moving inside. Thereafter, both the spicule and swirl continue to rotate clockwise. This is a possible case of CoSCo-I, where the helical velocity streamlines extend clearly between 4–8 Mm when first detected by the swirl detection algorithm and then move upwards finally interacting with the same falling spicule from much higher ($z > 8.0$ Mm) in

Table 4.1 A list of 3D rMHD simulations performed with different resolutions (Δ), domain size ($L_x \times L_y \times L_z$), imposed vertical magnetic field (B_0), kinematic viscosity (ν), and magnetic Prandtl number (P_m) used in the corona. Unless otherwise specified in the text, the results correspond to Run 3 with a grid resolution of 24 km.

Run	Δ (km)	$L_x \times L_y \times L_z$ (Mm^3)	B_0 (G)	ν (cm^{2}s^{-1})	P_m
1	48	$6.0 \times 18.4 \times 36.8$	25.0	4.0×10^{11}	1.0
2	48	$6.0 \times 9.0 \times 36.8$	3.0	8.0×10^{10}	20.0
3	24	$6.0 \times 9.2 \times 36.8$	7.5	7.5×10^{9}	1.0
4	24	$4.6 \times 4.6 \times 30.7$	10.0	1.0×10^{11}	1.0

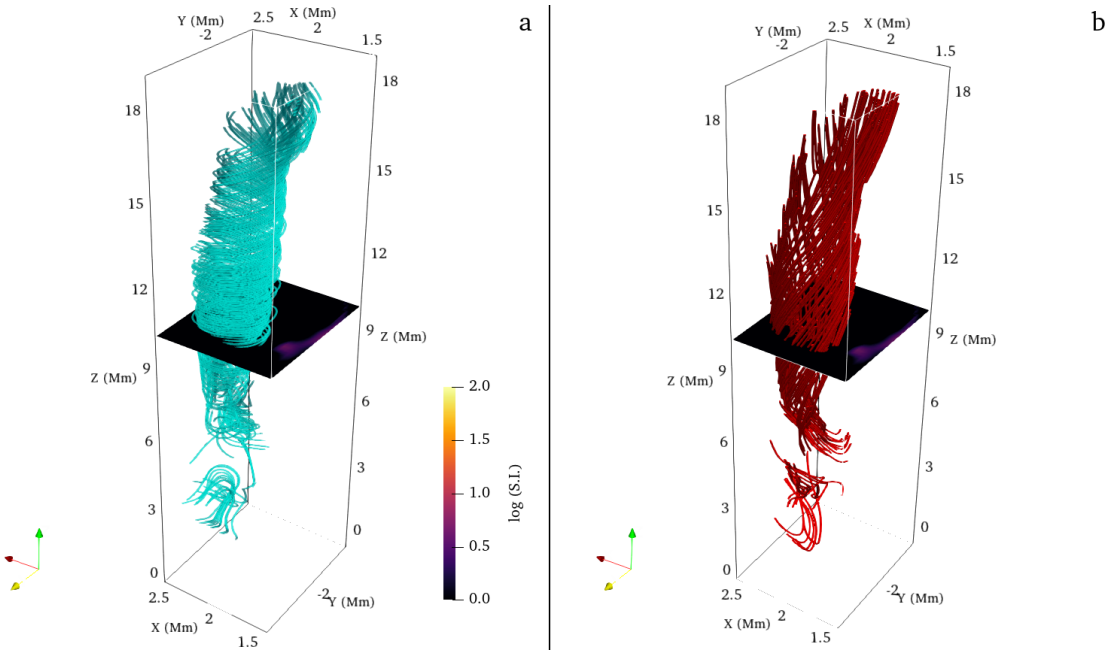

Fig. 4.13 An example of CoSCo-I which is rooted deep in the chromosphere region. (a) Horizontal plane at $z = 10$ Mm presents synthetic emission from spicules and velocity streamlines (cyan) associated with the CoSCo. (b) same as panel a, except magnetic field lines (red) are shown. This numerical configuration corresponds to the Run 2 of the Table 4.1.

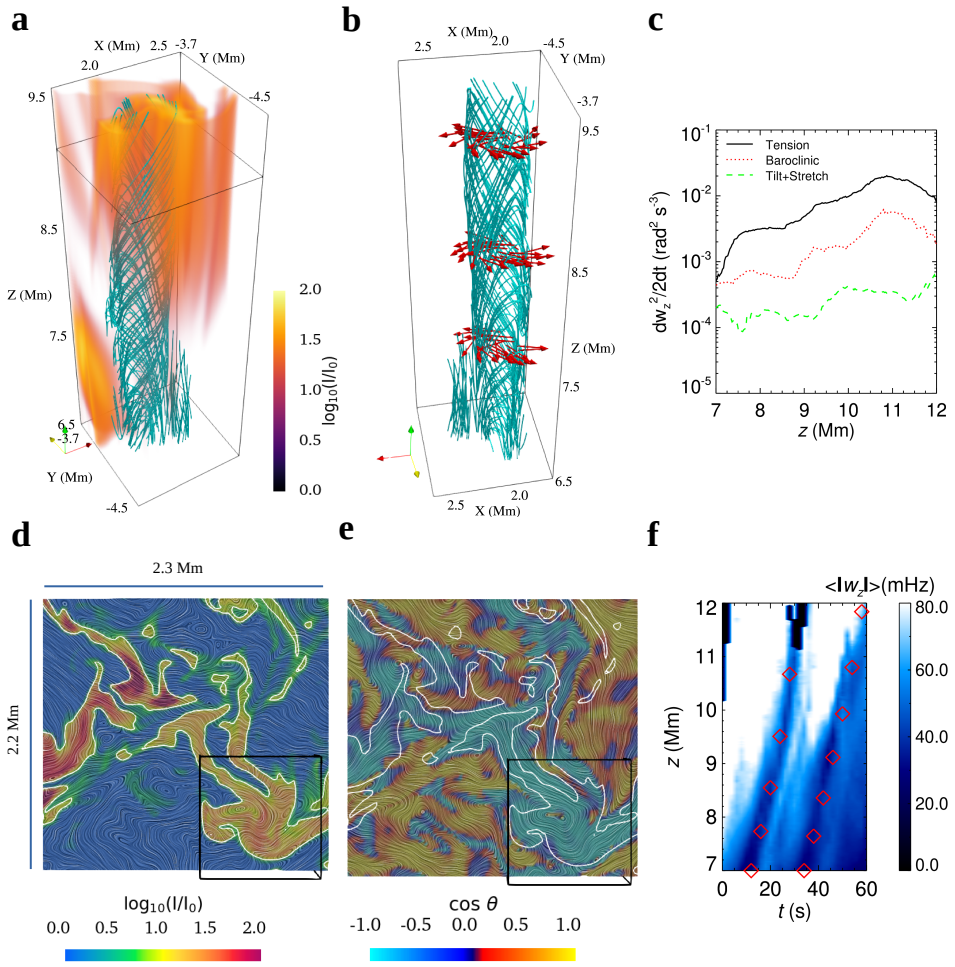

Fig. 4.14 Formation mechanism of CoSCo-I and their contribution to the bulk spinning motion of spicules. (a) Synthetic intensity of a spicule is shown in orange along with the co-spatial CoSCo-I (velocity streamlines are in cyan). (b) Horizontal component of twisted magnetic fields (red arrows) and velocity streamlines (cyan) are shown for the same region. (c) Rate of change of enstrophy due to different source components, averaged over the region of the corresponding CoSCo-I. (d) The horizontal magnetic field lines visualized by the Line Integral Convolution (LIC) technique and shaded by the synthetic intensity of spicules over the $z = 9$ Mm plane. (e) LIC representation of velocity streamlines shaded by the cosine of the angle between magnetic and velocity vector components lying on the same horizontal plane. White contours show the boundaries of spicules. The small black box corresponds to the same region as panel (a). (f) Time-distance diagram of absolute vertical vorticity, $|w_z|$, of the same CoSCo-I from panel (a), calculated using a 3D slit of extent 770 km $\times$830 km$\times$5 Mm, the longest dimension of which is oriented along the z-axis. Two Alfvén wave characteristics are shown by red diamonds for two different times. The Alfvén speed given by the slope of the curve varies between 125.3 – 302.8 km s^{-1} in the height range $6.6 < z < 12$ Mm

the atmosphere and making it rotate. Analysis of enstrophy- ω_z^2- generation terms inside that swirl indicates that the dynamics are dominated by magnetic tension (Fig. 4.14c). Magnetic fields are also found twisted at the same location as the swirl (panel b), contributing to a strong tension force. It is noteworthy that horizontal magnetic and velocity swirls coincide (Fig. 4.14 d–e), but the vectors are out of phase with each other for the entire height ($6.6 < z < 12$ Mm) of the CoSCo-I that could be detected by our vortex tracking method within its lifetime of ~ 76 s. Time-distance analysis of vertical vorticity enables quantifying the characteristic phase speed in the vertical direction. By averaging around a vertically oriented slit encompassing the region of the tall CoSCo-I (Fig. 4.14b), it is clear that these short-lived pulses propagate upward at the local Alfvén speed (Fig. 4.14f), similar to recently reported chromospheric swirls (Liu et al., 2019; Battaglia et al., 2021). The interaction mutually affects both the swirl and the spicule, although, it is difficult to estimate any energy exchange between the swirl and the spicule.

The second kind, CoSCo-II, proliferates next to spicules due to misaligned density and total pressure (gas+magnetic) gradients existing at their periphery. An example of CoSCo-II is shown in Fig. 4.15 with an anti-clockwise rotational sense and a lifetime of ~ 44 s. It originates at the periphery of a collapsing spicule and rotates spicular plasma in the same direction. Here, we find a prominent velocity swirl, but there is no corresponding magnetic swirl (Fig. 4.15b, d) along its height. The presence of the velocity swirl in the horizontal plane does not imply the existence of a corresponding magnetic swirl in this type of CoSCo. This is because the flow in these simulations is highly time-dependent, the velocity streamlines deviate from particle lines or pathlines as time progresses. Unlike in the CoSCo-I, the horizontal velocity and magnetic field vectors in this CoSCo-II do not have a 180° phase difference at any height range (Fig. 4.15d–e). From the enstrophy analysis, we find the vorticity generation due to the baroclinic term is large at the boundary of the associated spicule because of the sharp density gradient there (Fig. 4.15c) and supporting the formation of CoSCo-II there. More such examples of both CoSCo-I and II are shown in Fig. 4.16. This description holds true for the entire CoSCo's lifetime of ~ 44 s. It is therefore possible that, during their formation, CoSCo-IIs draw their energy from spicule-driven baroclinic instabilities. Because of a spicular source in the atmosphere, the spiraling velocity streamlines of these CoSCos and their fluxes may be disconnected from the photosphere. The resultant swirls also back-react on the spicules affecting their rotational and lateral motions. This refers to a highly coupled, non-linear nature of evolution between the spicule and the swirling plasma. Therefore it becomes difficult to separate the background state from the perturbed state in order to make any growth rate estimation for the baroclinic instability. Even with several crucial differences, similarities exist between the specific cases of the two kinds of CoSCos presented here. Both form in the atmosphere where the plasma $\beta < 1$. In the CoSCo-II instance too, a vortex pulse propagating

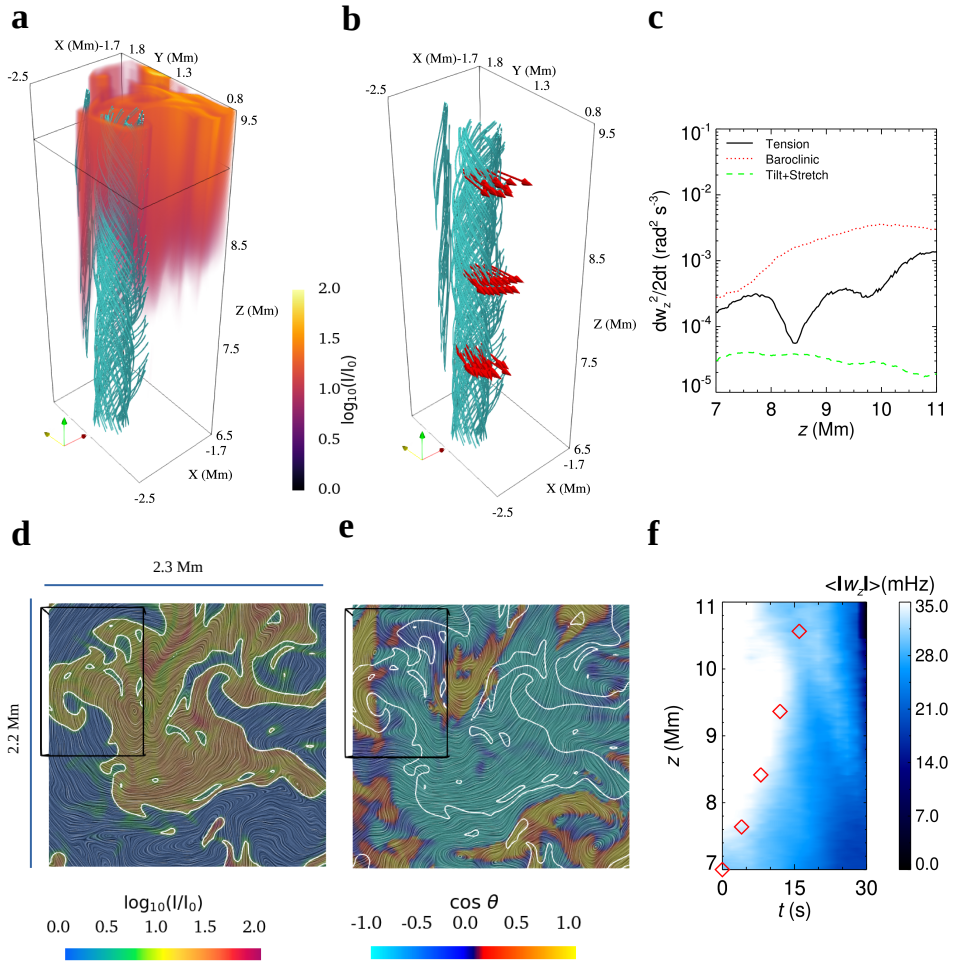

Fig. 4.15 Generation of CoSCo-II from the baroclinic instability at the periphery of a synthetic spicule. Same as Fig. 4.14 a–f panels but for a different spicule at a different location and time. The extent of the 3D vertical slit for the purpose of time-distance analysis is 600 km $\times$600 km$\times$4 Mm. The Alfvén wave speed varies in the range 217.2 – 489.5 km s^{-1} between $8 < z < 12$ Mm.

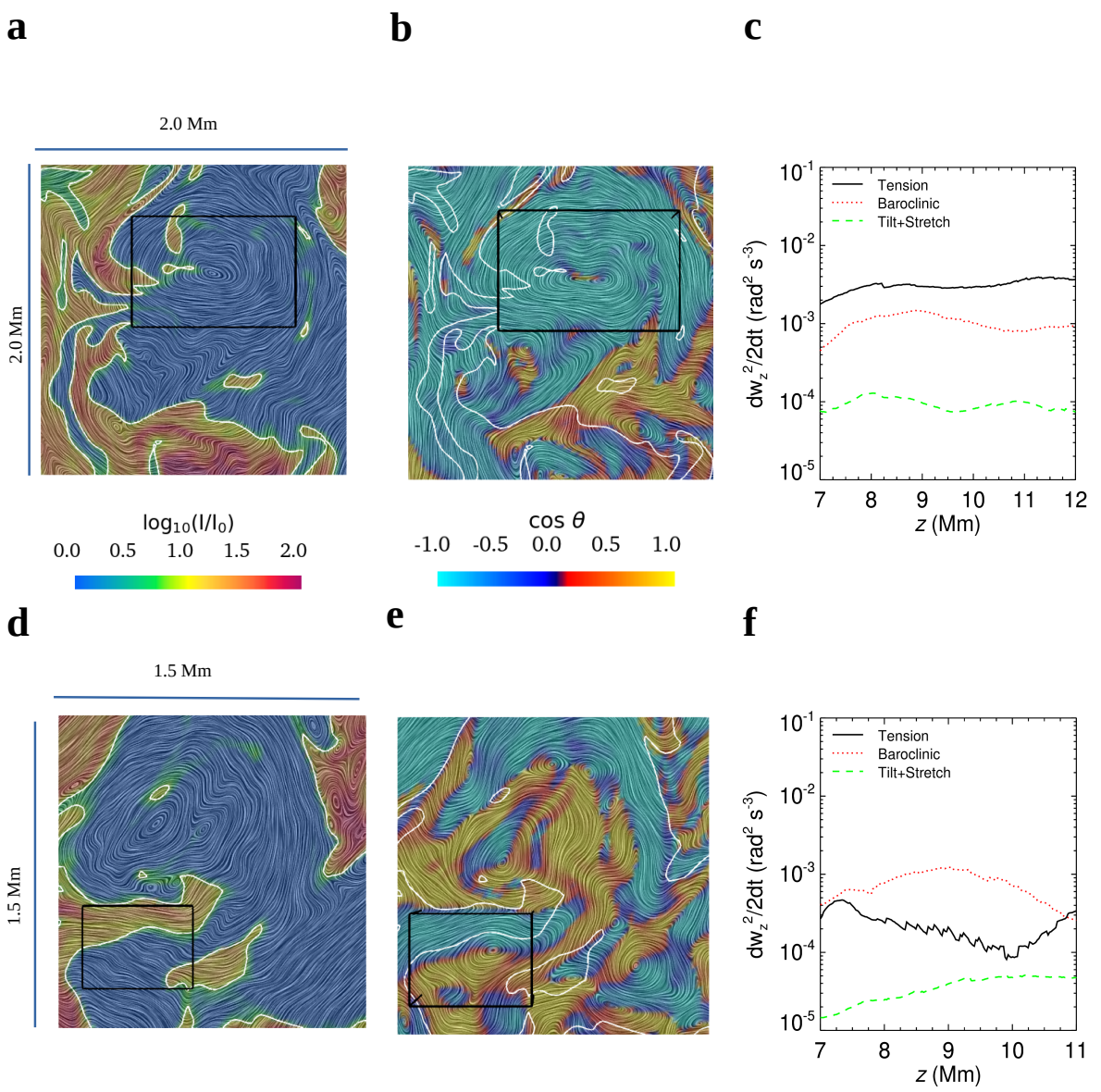

Fig. 4.16 Examples of different types of CoSCos and their associated enstrophy sources. (a) The horizontal magnetic field lines colored by the synthetic intensity of spicules is shown in the z = 9 Mm plane. (b) The velocity streamlines shaded by the cosine of the angle between the horizontal magnetic and velocity field vectors. Overplotted white contours represent the boundaries of spicules and black rectangular box locates the region of CoSCo-I. (c) Rate of change of enstrophy due to different source components, averaged over the region of the corresponding CoSCo-I. Panels (d)–(f) provide an example of CoSCo-II also at $z = 9.0$ Mm, similar to Panels (a)–(c).

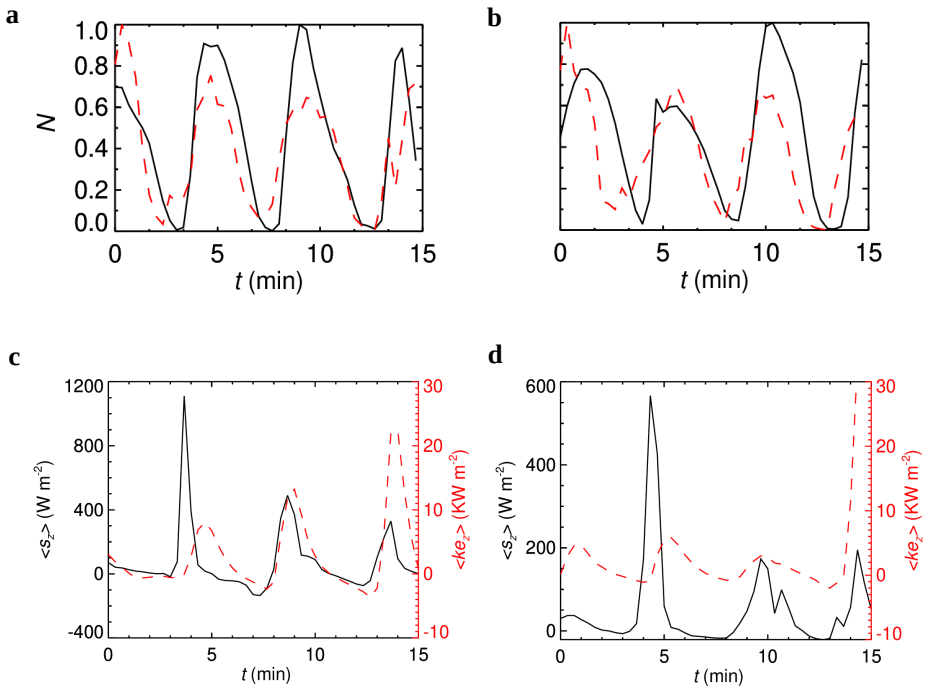

Fig. 4.17 Correlation between spicule and swirl abundance in a periodically forced setup: number of spicules (black) and swirls' (red) variation is shown with time, normalized with maximum population over the duration

with the local Alfvén speed is detected as shown in Fig. 4.15f. Both kinds of swirls are hotter than the spicules of their vicinity and they may move inside the spicules and spin them. To emphasize that some coronal swirls can be excited by spicules themselves, we carry out a simple 3D numerical experiment without a turbulent convection layer (Run 4 of Table 4.1). The model is driven by a periodic vertical forcing at the photosphere, mimicking solar *p*-mode oscillation. After 3–4 cycles of forcing, coherent spicules form in a similar vertically imposed magnetic field condition, reported by (Dey et al., 2022). The recurring nature of the population distribution of spicules and swirls with time is solely due to the nature of the driving. The correlation between the two distributions strongly supports the idea of the excitation of coronal swirls, coupled with spicular jets. To distinctly show the enstrophy sources of these swirl tubes due to only baroclinic and magnetic tension forces, we exclude the nonlinear advective term in the velocity equation for the Run4. As a consequence, there will be no tilt-stretch and advective sources of Enstrophy for the growth or decay of swirl tubes (see Equ. 4.3).Since CoSCos of both kinds are often seen to either extend vertically upward or downward with time, thereby spanning the entire atmosphere, the rotational and electromagnetic energies must also be propagating, likewise.

4.5 Contribution to the energy and mass flux

The rotational energy of the core region (size$\sim$ 300 km) of CoSCos (either type), estimated at different heights and averaged over 30 mins of the simulation is shown in Fig. 4.18a. From these plots, we conclude that i) The time variation of the rotational energy of the swirls is anti-correlated with the mass flux of spicules at a given height (Fig. 4.18a,c), i.e., in the falling phase of the spicules, the swirl rotational energy increases and vice-versa. This anti-correlation could be either because of CoSCos deriving their rotational energy via baroclinic and magnetic tension terms at spicule edges or due to spicular plasma in the rising phase suppressing the existing CoSCos. ii) The Poynting fluxes for swirls do not decrease appreciably in the indicated height range because of their tall cylindrical geometry. For the isolated CoSCo-I in Fig. 4.14, the estimated time averaged rotational energy flux, $\langle \rho (v_x^2 + v_y^2) v_A \rangle /2$ is 0.34 kW m^{-2} and the vertical Poynting flux is given by 0.49 kW m^{-2} at $z = 9$ Mm. iii) A curious phenomenon seen in all simulation runs is that the mass and the Poynting fluxes carried by spicules, once again identified by the bright regions of the drapery, are typically anti-correlated in time (Fig. 4.18c,d). At the end of their lifetime, spicules fall towards the photosphere, and yet the vertical Poynting flux contributed by the spicules, $\langle v_z B_h^2 - B_z (v_h . B_h) \rangle / \mu_0$ is positive. This is contrary to the case where all the spicules are driven by a harmonic forcing (Run 4 of Table 4.1) applied at the photosphere where we observe the mass and Poynting fluxes to be in phase at the same range of heights (Fig. 4.17c,d). A comparison between panel a-b of Fig. 4.19 provides supporting evidence for the spatio-temporal overlap between upward propagating Poynting flux and the regions with $B_z (v_h . B_h) < 0$ in the entire domain. There are strong indications of a relation between upward directed Poynting fluxes and the formation of CoSCos embedded in a sheared flow because we find several instances with large positive Poynting fluxes in regions surrounding the CoSCo cores (Fig. 4.19). One could deduce that the Poynting fluxes are not just transported by spicules (as defined by only the brightest parts of the drapery), but also by the surrounding regions that include the dimmer regions of the drapery as well as the swirls (Fig. 4.18b,d and 4.20a). In general, the averaged Poynting flux contribution over the entire horizontal extent can reach 100 W m^{-2} at $z = 12$ Mm. In the solar atmosphere, we find not just the transport of the Poynting fluxes from the photospheric to the solar corona but also the generation of fluxes locally (the encircled regions of the time-distance plot in Fig. 4.20a) Additionally, the oscillatory horizontally averaged mass flux $\langle \rho v_z \rangle$ over an area of 6×9 Mm^2, at all heights for simulations as a function of time is given in Fig. 4.20b. The time-height plot shows a positive slope in both rising and falling phases indicating that the maximum z at which the vertical velocity is positive (negative) shifts upward as the spicule rises (falls). At a fixed time indicated by the dashed line in Fig. 4.20b, the mass flux is positive above $z > 5.0$ Mm and negative below. The consequence of this is that the lighter matter at the spicule tip continues

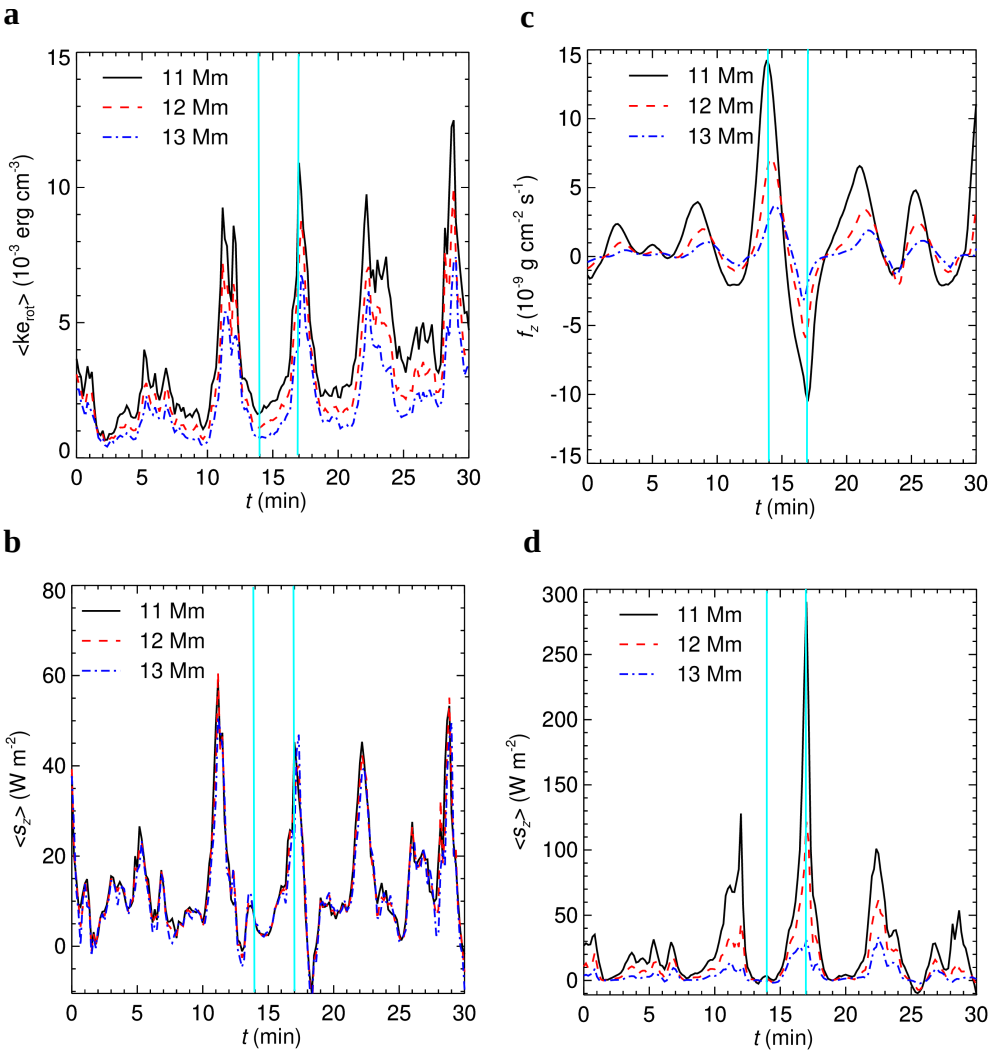

Fig. 4.18 Temporal variation of the horizontally averaged kinetic energy, mass, and Poynting energy fluxes (over the region of 6 Mm $\times$ 9 Mm) at three different heights in the atmosphere as indicated. (a) Rotational kinetic energy, $\rho v_h^2/2$, of the CoSCos, with v_h representing the horizontal component of velocity. (b) Poynting flux contribution from CoSCo cores only as detected by the ASDA technique. (c) Mass flux and, (d) Poynting flux contribution from spicules, identified by 80000 K plasma emission contours where the synthetic intensity is > 10 times its horizontal average. The vertical cyan lines are to guide the eye for temporal correlation between physical quantities plotted.

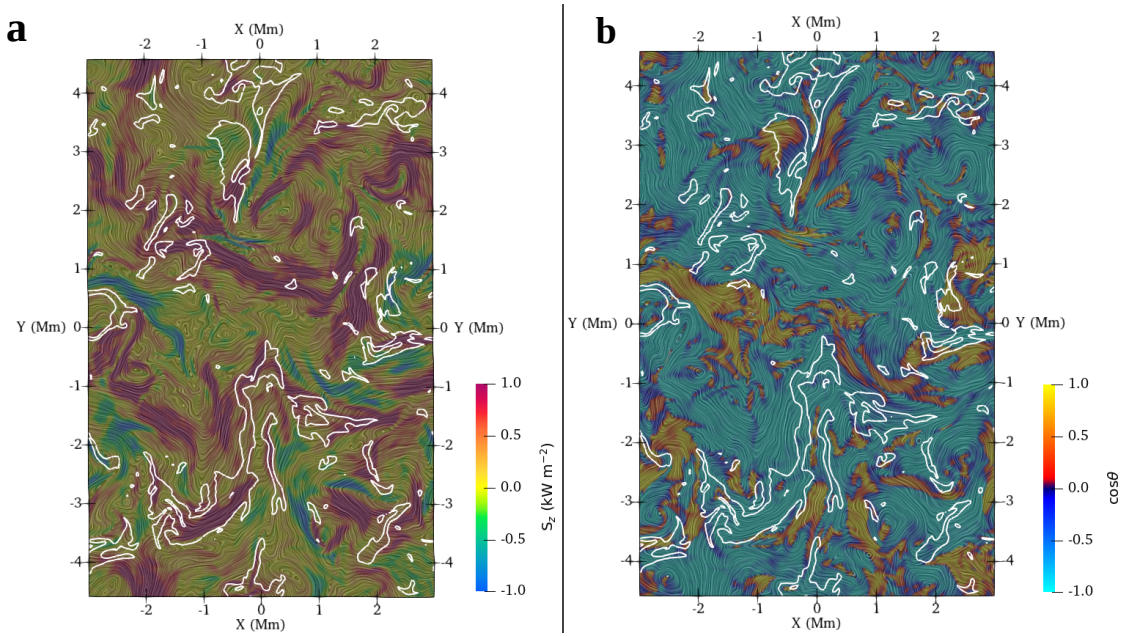

Fig. 4.19 Spatial distribution of the vertical Poynting flux over the entire horizontal domain of 6×9 Mm^2. (a) Horizontal magnetic field shown using Line Integral Convolution (LIC) technique (Methods) and shaded by the vertical Poynting flux (S_z) at the $z = 11$ Mm plane. Spicule boundaries are demarcated by white contours. (b) Velocity streamlines (visualized using LIC) shaded with the angle between horizontal magnetic and velocity field vectors in order to distinguish CoSCos of type I & II.

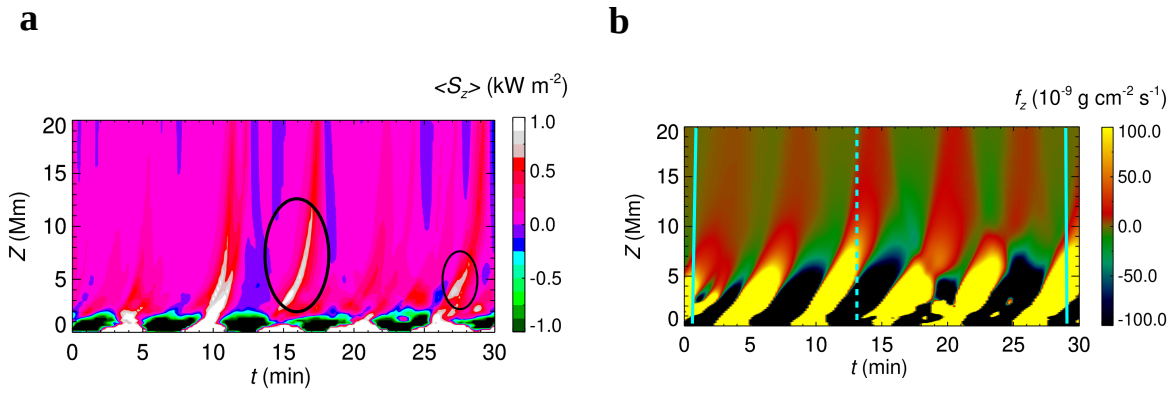

Fig. 4.20 Time-distance diagram of the (a) horizontally averaged Poynting flux. Encircled regions demarcate local enhancement of Poynting flux in the atmosphere. (b) mass flux contribution over the entire 6×9 Mm^2 domain. The vertical cyan solid lines confine five complete cycles to estimate the time-averaged mass flux correctly. The dashed line indicates a particular time at which the mass flux along the z-axis changes sign

to rise even while the heavier plasma in the lower base is falling. Even though the spicule, as imaged by transition region lines, do not reach beyond 16 Mm, the kicks imparted to the plasma column above the tip is accelerated layer-by-layer by a propagating slow mode shock. Thus, in the Sun, an ever-increasing acceleration communicated to successively lighter layers at the top could be creating a domino effect, allowing a small fraction of this mass to reach the height at which the solar wind becomes supersonic, where the plasma ceases to be ballistic. The temporally averaged mass flux over the five cycles spanning a 28 min duration is always positive for this sample simulation and is of the order of 2.16×10^{-9} g cm^{-2} s^{-1} at $z = 12$ Mm height. Note that in the solar coronal holes, the mass loss due to fast solar wind is estimated to be 2×10^{-10} g cm^{-2} s^{-1} in the solar corona from observations made near the Earth (Withbroe & Noyes, 1977). The difference between the two mass flux calculations could be attributed to the observation of rapid expansion of the angular area of a coronal hole region with distance from Sun (Munro & Jackson, 1977), a factor not accounted for in our Cartesian box simulations. In summary, our simulations indicate a pleated drapery-like morphology for spicules in a coronal hole region on the Sun, without the inclusion of any photospheric flux emergence and ionization non-equilibrium effects. The reason spicules can still appear as conical jets in observations is because the sheets appear brighter only in regions where pleats are gathered and thus less bright parts of the plasma drapery remain below detection thresholds. Stereoscopic observations of the same region on the Sun simultaneously with a pair of telescopes for chromospheric or transition region lines may be required to observationally establish, whether spicules are topologically two-dimensional fluted curtain embedded in three-dimensional plasma (Judge et al., 2011; Rast et al., 2021) or simply one-dimensional straws. Further, a domino-effect-like mechanism can explain a net positive mass flux found near the top of the domain and not just in the brightest regions of the plasma drapery (identified as straw-like spicules). The latter provides the mass reservoir for the fast solar wind along open magnetic field lines in the coronal hole regions Zirin (1988). In contrast to spicules that fall back to the solar chromosphere, the CoSCos and the associated shearing flow form by drawing energy from the thermal and magnetic energy reservoir of the chromospheric plasma via baroclinic and magnetic tension terms. Therefore, CoSCos have the potential to carry the rotational energy pulses further upward at Alfvén speeds than the typical length of spicules seen in the Si IV emission lines even when spicules are falling sun-ward. Detection of the rotating bunches of spicules both in observations and in simulations presented here affirms that rotating spicules on the Sun mark regions where CoSCos exist. Therefore a complete picture of momentum and energy transport to the fast solar wind must take into account this coupling between spicules and CoSCos. Looking forward, observations with high resolution and sensitivity taken simultaneously in different layers of a locally unipolar magnetic region on the Sun (Berger et al., 2004) will

help investigate the energy exchange between spicules and swirls and eventually its outward transport.

4.6 Appendix

4.6.1 Vortex detection and visualization with ASDA and LIC

The detection of vortices over multi-dimensional data is an active field of research, and its usage can be found across different disciplines. There are several methods, namely Automatic Swirl Detection Algorithm (Graftieaux et al., 2001) (ASDA), Swirling strength criterion (Zhou et al., 1999), Lagrangian Averaged Vorticity Deviation(LAVD) (Haller et al., 2016) to detect vortices over different time frames. Here, we use the ASDA method to track swirls distributed between the solar photosphere and lower corona. In this method, there exists a free parameter known as window size, which acts as a local filter to smooth out the small-scale fluctuations in the velocity field. We have selected a window of 480 km $\times$ 480 km, which is the typical diameter of existing vortices. Over the window in each horizontal plane, two crucial quantities γ_1 and γ_2 are computed to locate the center and circumference of the vortex tube. Incompressible fluid models provide a range of threshold values of axisymmetric vortices to demarcate the core rotating region. In our compressible turbulent convection model, we have noticed that $|\gamma_1| \geq 0.55$ regions distinguish clockwise and anti-clockwise rotating non-axisymmetric vortices even in the presence of strong shear flows. We have also confirmed these regions independently by comparison with a 2D flow visualization method known as Line Integral Convolution (LIC) applicable to streamlines in the horizontal plane. We apply this method at every horizontal layer in the height range 0–20 Mm and track the vortex tubes over the time duration of 30 minutes.

4.6.2 Characteristics of shock-fronts

Here we will find the characteristics of shock fronts in terms of jump profile in thermodynamic quantities across shock fronts and the propagation speed of fronts. Here, the jumps associated with shocks are provided in Fig. 4.21. The density compression ratio ranges from $1.86-2.19$ in between $3.5-4.5$ Mm height. Using the Rankine-Hugoniot jump condition, we estimate the corresponding upstream Mach number (u/c_s) of $1.61-1.90$ with respect to the shock front reference frame. We find temperature enhancement in the downstream flows by a factor of $2.01-2.64$ compared to the upstream. In panels (c) and (f) of Fig.1, we track the compression profile of associated shocks with Time-distance diagrams. The slope of the compression regions in the diagram represents the shock front speed from the rest frame. We determine the front speed (u_{shock}) independently from the definition of Mach no ($u_{shock}=c_s\times$ Ma+$u_{upstream}$) and

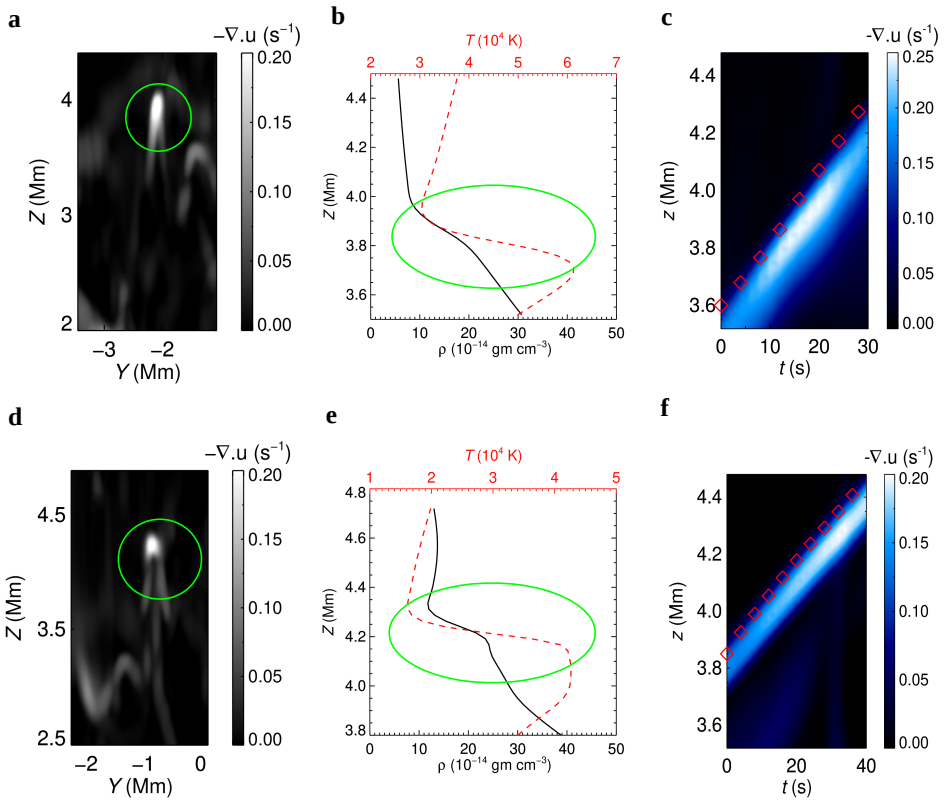

Fig. 4.21 Characteristics of shock-fronts: (a) Selected Field of Views (FOVs) in yz-plane to analyze shock front properties. (b) Density (black-solid) and temperature (red-dashed) across the selected shock fronts are shown in (a). (c) Time-distance plot of strong plasma compression (-$\boldsymbol{\nabla}$.**U**) associated with the shock. Overplotted red squares represent the height of the shock in the atmosphere with time. (d)-(f): Same as (a)-(c), but for a different shock location.

represent the characteristic curve by red squares. The slope of the characteristic curve matches well with the slope of the compression regions, showing the same shock front speed obtained from different methods.

5

A brief overview of the forest of solar spicules: from different numerical models

5.1 Introduction

Solar spicules are one of the features of the sun which have been extensively studied by different numerical simulations over the past several years. The modeling effort started with considering the ideal MHD setups and then moved to the non-ideal MHD sector with several intricate physics. Although a large section of the simulation results could not match with observed ubiquity and characteristics of spicules, particularly the height of the spicules. A large section of 2D, 2.5D, and 3D rMHD models assemble jets with a maximum height range of ≈ 7 Mm (Heggland et al., 2011; Iijima & Yokoyama, 2015; Iijima & Yokoyama, 2017; Martínez-Sykora et al., 2017; Wójcik et al., 2020), whereas in observations, spicules are found with a height range $4-16$ Mm (Zhang et al., 2012). In a 3D ideal MHD model, Iijima & Yokoyama (2017) found that only a single simulated spicule reached $10-11$ Mm height by the action of twisted and inclined magnetic field lines. Whereas Martínez-Sykora et al. (2017) reported that the abrupt release of magnetic tensions supported by Ambipolar diffusion could drive a few spicules to reach the 10 Mm range. Often, it becomes difficult to compare results across

different models as they have different spatial resolutions, different approximations in terms of physical processes, variations in the treatment of numerical diffusion and boundary conditions. In our context, the definition of spicular jets also plays a crucial role in studying their properties from numerical models. It is important to notice whether features are assigned as spicules only in terms of thin, cool temperature profiles or through synthetic emission profiles by considering the density and temperature contribution or by non-trivial NLTE modeling. Understand the lack of coherency among different numerical models; we perform a brief comparative study of the forest of solar spicules by combining our 3D rMHD model with two publicly available setups from the Bifrost code (Gudiksen et al., 2011).

5.2 Description of numerical models

We first select two independent 3D Bifrost models, **ch024031_by200bz005** & **qs006005_dyc**, which have the closest similarities with our 3D rMHD models. The overall magnetic topology corresponding to model **ch024031_by200bz005** matches with solar coronal hole regions, where open magnetic field lines dominate (Carlsson et al., 2016). In model **qs006005_dyc**, local dynamo operates; hence there are small-scale flux emergence at the photosphere, resembling Quiet Sun regions (Martínez-Sykora et al., 2019). Here we provide critical details of the Bifrost and Pencil code setups.

5.2.1 Bifrost Code: ch024031_by200bz005

- Name: **Bif1**
- Domain size ($x \times y \times z$): $24.0 \times 24.0 \times 17.0$ Mm^3
- Location of bottom and top boundary: at -2.5 Mm & 14.3 Mm
- Resolution: a uniform horizontal resolution of 31 km and non-uniform vertical resolution ranging from 12 to 82 km
- Magnetic field: The signed averaged magnetic field of 5 G, similar to coronal hole regions. Additionally, horizontal fluxtubes are fed from the bottom boundary.
- Inclusion of NLTE physics: No

5.2.1.1 Bifrost Code: qs006005_dyc

- Name: **Bif2**

- Domain size ($x \times y \times z$): $6.0 \times 6.0 \times 10.5$ Mm^3
- Location of bottom and top boundary: at -2.5 Mm & 8.0 Mm
- Resolution: a uniform horizontal resolution of 5 km and non-uniform vertical resolution ranging from 4 to 20 km
- Magnetic field: The r.m.s. magnetic field of 56 G developed through the local dynamo process
- Inclusion of NLTE physics: Yes

5.2.2 Pencil Code: setup1

- Name of the setup: **PC1**
- Domain size ($x \times y \times z$): $6.0 \times 9.0 \times 36.8$ Mm^3
- Location of bottom and top boundary: at -5.0 Mm & 31.8 Mm
- Resolution: uniform resolution of 24 km in every direction
- Magnetic field: The signed averaged vertical magnetic field of 7.5G, similar to coronal hole regions.
- Inclusion of NLTE physics: No

5.2.3 Pencil Code: setup2

- Name of the setup: **PC2**
- Domain size ($x \times y \times z$): $6.0 \times 18.0 \times 36.8$ Mm^3
- Location of bottom and top boundary: at -5.0 Mm & 31.8 Mm
- Resolution: uniform resolution of 48 km in every direction
- Magnetic field: The signed averaged vertical magnetic field of 5G, similar to coronal hole regions.
- Inclusion of NLTE physics: No

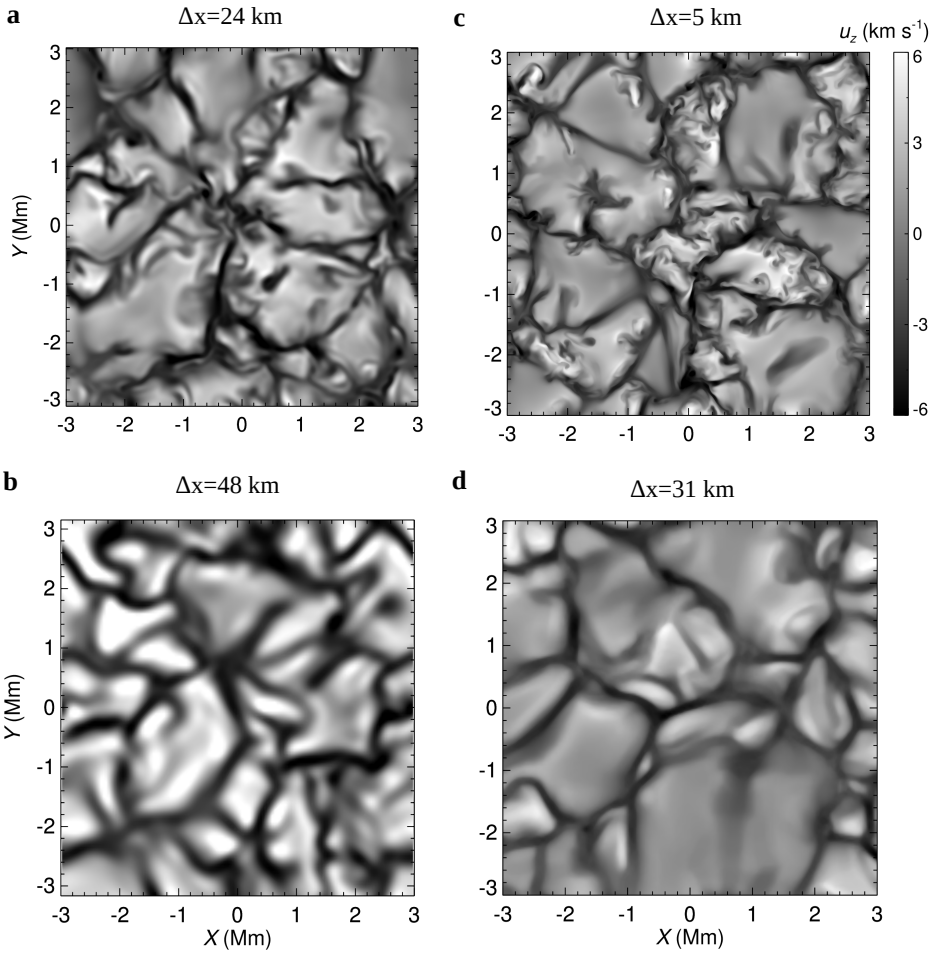

Fig. 5.1 A comparison of simulated granulation structures in terms of vertical velocity, u_z, at the photosphere: (a) From model **PC1** (b) **PC2** (c) **Bif2** (d) **Bif1**

5.3 Results

The driver to evolve all considered rMHD models here is the same, the self-sustained solar convection. Hence, we first compare the granulation patterns at the photosphere in terms of the vertical plasma velocity (Fig. 5.1). The spatial scale of granules is one of the indicators of correct density scale heights and cooling process. We notice granules with a horizontal spatial scale of 1–3 Mm for all four cases, consistent with observations (Nordlund et al., 2009). In terms of the small-scale structures, a clear difference is present between coarse (**Bif1** & **PC2**) and fine grid data sets (**Bif2** & **PC1**). It is expected due to the high numerical diffusion for coarse grid ones. At the downflow or intergranular lanes, we find a strong presence of small-scale vortices similar to photospheric observations due to the shearing motion of nearby granules (Nordlund et al., 2009; Shelyag et al., 2011).

To get insights into the overall behavior of rMHD models, we focus on the plasma density (ρ), temperature (T), and plasma-β. For all three models, we find an excellent agreement in terms of the variation of horizontal mean plasma density (black solid) along the height (Fig. 5.2). At, $z = -2$ Mm (8 Mm), $\rho \approx 10^{-5}$gm cm^{-3}(10^{-15}gm cm^{-3}). Although the behavior of the temperature profile (red dot-dashed) is different. At $z = -2$ Mm, all models have a similar averaged temperature of 2×10^4 K. **Bif1** model shows a much steeper nature of the temperature curve. At $z = 8$ Mm, it reaches 6×10^5 K. Atmosphere of our model, **PC1** and **Bif2** are much cooler ($\approx 2 \times 10^5$ K) than **Bif1** model. We describe the cooler characteristic of our model with the presence of numerous tall spicules in the atmosphere. It requires additional investigation to understand whether magnetic flux emergence has any contribution to the high temperature of model **Bif1** or not. To understand the governing factor in dynamics, plasma-β, the ratio of gas pressure and magnetic pressure is a useful parameter. Hence, we analyze the horizontally averaged plasma-β profile with height. All curves (blue-dashed) present a similar behavior but have different values. For **PC1** model and **Bif1** model, it is approximately 0.1 at $z = 8$ Mm, although, for **Bif2** model, it is 0.01. Therefore the Quiet-sun model (**Bif2**) exhibits a higher level of magnetic dominance in the corona than its counterparts. We also want to mention that the treatment of the gas pressure in our model is based on LTE approximation with the help of Saha ionization equation, whereas **Bif1** and **Bif2** models are based on opacity tables and non-equilibrium ionization fraction of Hydrogen atoms, respectively.

Now we shed light on the jet structures by computing the line of sight integrated synthetic intensity profile at $T = 20000$ K (Fig. 5.3), following the same technique discussed in Chapter 3. In our model (**PC1**), a large number of fine-scale spicules are assembled, presenting a forest-like visual impression akin to solar observations. These jets are able to reach up to 16 Mm in height during their evolutionary phase. From the coronal hole model (**Bif1**), we detect a few

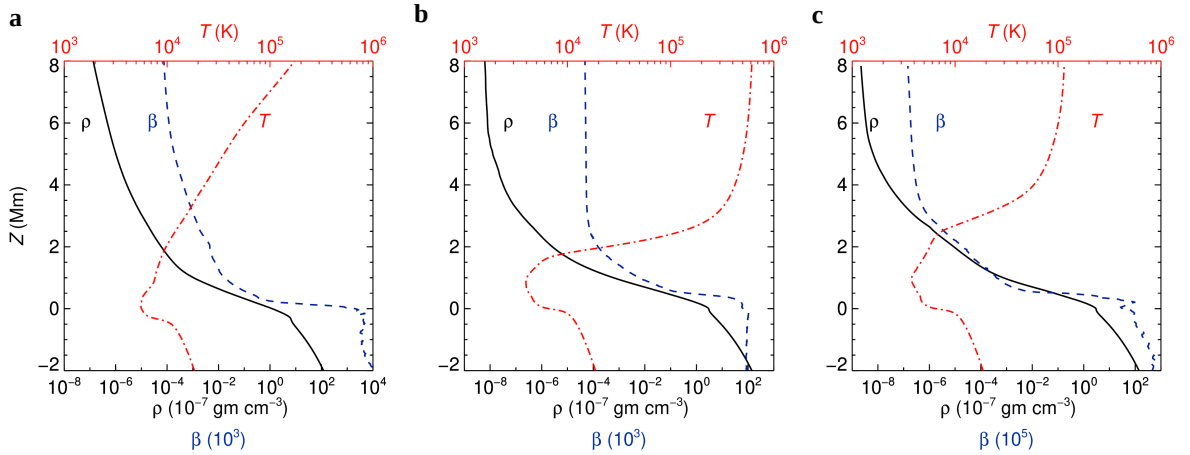

Fig. 5.2 Stratification profile of plasma density, temperature, and plasma-β under constant solar gravity: (a) From model **PC1** (b) **Bif1** (c) **Bif2**

spicular structures with a maximum height of 8 Mm. There are many fine-scale jets in the **Bif2** model, although the maximum height is only 6 Mm. Further, we investigate the triggering mechanism of jet structures by analyzing shock fronts in the atmosphere Fig.5.4. Detection of these fronts is performed by the strong compression regions ($-\nabla \cdot \mathbf{U}$), similar to Chapter 4. They are primarily associated with the propagating slow MHD modes in the higher atmosphere. In our model (**PC1**), these accelerating fronts are highly wedged-shaped, or the focusing of the acoustic power is stronger than in other models. Hence, shock fronts in our model help accelerate the spicular plasma, which can reach a maximum height of 16 Mm. We can also notice a general characteristic from all models: jets mostly follow the shock front morphology in the lower atmosphere. The acoustic modes leaking from the photosphere form shock fronts as they propagate upwards into a rarefied atmosphere thereby creating the positive vertical acceleration regions. While this positive acceleration region propagates upwards at slow MHD wave speed, it energizes the plasma locally so as to form jets that shoot upwards against the local gravity. Therefore, MHD shocks drive spicules in our model. However, vice versa i.e., spicules driving shocks are not found in our model. In this context, we want to mention that in panel c of Fig 5.4, a green horizontal line is present due to a numerical artifact. It was produced while interpolating the data set from cell faces to the cell centers as a part of post-processing. In this brief overview study, we notice some remarkable similarities in the qualitative and quantitative aspects of the Bifrost and Pencil code data. Apart from similarities, we see differences in temperature profiles, height distribution of spicules, and shock front structure, even after performing all analyses from the same footing. This helps to locate the origin of the discrepancy, which is probably the shock front here.

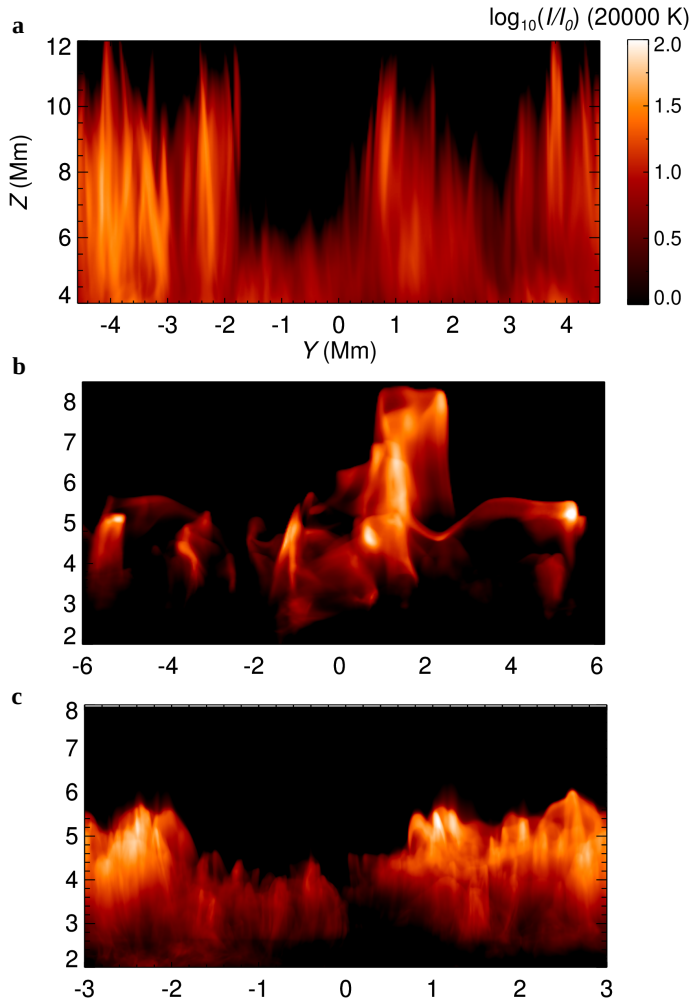

Fig. 5.3 A comparative analysis of line-of-sight integrated synthetic intensity profile of spicular jets at $T = 20000$ K. Here $I_0 represents$ the horizontally averaged intensity of plasma, which is a function of height(z) : (a) from model **PC1** (b) **Bif1** (c) **Bif2**

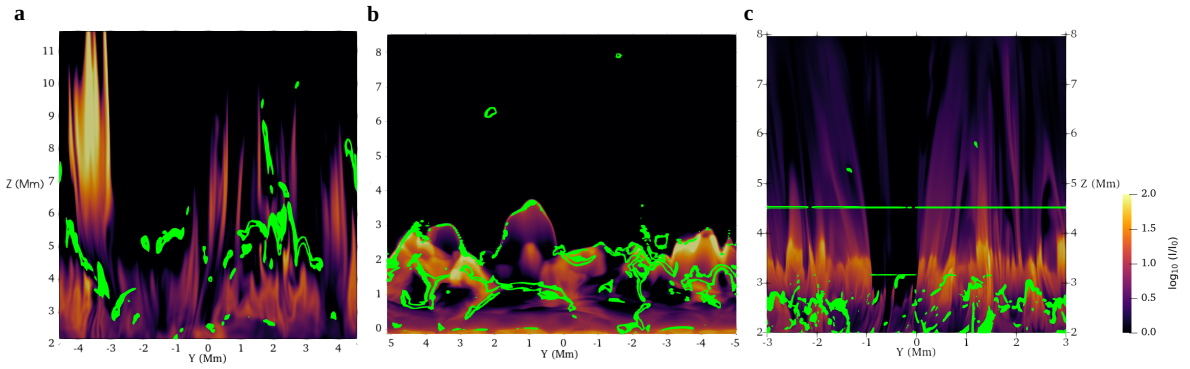

Fig. 5.4 Association of the shock fronts with spicular jets: shock fronts are shown with green iso-contours, and synthetic intensity of spicule is presented in the vertical plane for model (a) **PC1** (b) **Bif1** (c) **Bif2**

6

Discussions and future prospects

6.1 Discussions

In this thesis, we study the genesis and dynamics of one of the ubiquitous features of the sun called solar spicules. For this purpose, we combine numerical simulations, laboratory experiments, and observed data sets to gain in-depth insights into the system.
In Chapter 1, we present a brief overview of the forest of solar spicules from the perspective of solar observations and numerical modeling. In Chapter 2, we build our radiative Magnetohydrodynamics (rMHD) model to investigate solar plasma by including several non-ideal, non-adiabatic physical processes. Under Chapter 3, we focus on the formation mechanism of the solar spicule forest. To the bottom of a gravitationally stratified atmosphere with imposed vertical magnetic fields, we apply sinusoidal vertical forcing to replicate the effect of global acoustic oscillations (p-mode) in the absence of the subsurface convection zone. These models with sinusoidal forcing are able to excite a forest of synthetic spicules with large amplitude forcing. Motivated by surprising similarities in characteristic non-dimensional quantities of the solar plasma and laboratory fluid system, we apply vertical vibrations on polymeric fluids by a subwoofer speaker. A similar jetting behavior at the free surface of a polymeric fluid is noticed. The variation of critical scaled acceleration to drive jets with applied scaled frequency becomes

similar for these two disparate systems. Next, we demonstrate that coherent jet formation becomes possible only in the anisotropic system by comparing visco-elastic filled with polymer chains and isotropic Newtonian fluids. For the polymeric solution, turbulent energy is absorbed by polymer chains, and hence underlying Plateau-Rayleigh Instability is suppressed. In the MHD plasma, magnetic fields provide this anisotropy by to form coherent jet structures via Maxwell's stress tensor, thereby arresting the Kelvin-Helmholtz instability. We report the suppression of both instabilities have parallel nature with increasing polymer concentration and imposed magnetic field strength. In the end, we provide the sufficient conditions (a) fluid medium, (b) gravity, (c) large-amplitude quasi-periodic driving, (d) anisotropy of the medium to assemble a forest of jets irrespective of the nature of the medium by inducing non-linear development.

Next, we include a convective layer and couple it with the solar atmosphere to to check if solar convection can drive a forest of spicules with properties similar to those observed. Solar global oscillations naturally arise due to the sub-surface convective motion. These undulations leak into the upper atmosphere and energise the plasma as a steep acceleration front develops and propagates upwards is similar to the "Domino effect" and causes spicular jets. Characteristics of synthetic jets, e.g., height range of $6-25$ Mm and speed range of $30-85$ km/s, match astonishingly well with observed properties of spicules even in the absence of chromospheric microphysics of ambipolar diffusion and non-local thermodynamic equilibrium of the partially ionized plasma. We distinguish that several mechanisms associated with triggering jets, e.g., (i) squeezing by granular buffeting (ii) solar global modes (iii) aided by magnetic reconnection, are present in our model. However, we report that each process is ultimately controlled by the same underlying driver: solar convection.

In Chapter 4, we extend our model to three dimensions and compare it with high-resolution solar observations. From our 3D rMHD model with a background vertical magnetic field, we report spicules as pleated drapery of plasma, in contrast to the standard perception of conical or tube-like geometry. Although, we find the line-of-sight (LOS) integrated profile still shows the bright conical structure. This is so because the LOS integration takes into consideration several folds of inhomogeneous fluted plasma sheets. These extended plasma structures in our model are mostly formed in the first place by the slow MHD shock fronts resulting from leaking global acoustic oscillations into the solar atmosphere. Hence with such morphology, the filling factor of the denser plasma becomes different for the solar atmosphere, and as a consequence, the estimation of mass, momentum, and energy fluxes transported to the solar corona gets altered. Our laboratory fluid experiments also direct to such morphology of jets. A fluted current sheet-like morphology has already been observationally conjectured for spicules (Judge et al., 2011, 2012; Lipartito et al., 2014). Next, we target yet another aspects of the complex evolutionary

phases of observed solar spicules, namely, their bulk spinning motion. In our self-consistent 3D rMHD model, we find several cases of bulk spinning motions amongst clusters of spicular jets. Next, we analyze an observed dataset from the Broadband Filter Imager (BFI) of the Solar Optical Telescope (SOT) instrument onboard the Hinode satellite. Comparing the time-distance diagram of observed spicules with their synthetic counterparts, we notice similar inter-crossing features of spicular strands as a consequence of the bulk spinning motion with similar order of spinning time periods. In understanding the fundamental mechanism behind this motion, we identify highly dynamic, coherent, swirling elements that interact with spicules and spin them. We call them coronal swirling conduits (CoSCo)– as they are tall, cylindrical structures, have rotational speeds of 2˜20 $\mathrm{km\,s^{-1}}$, average lifetime of 20˜120 s, and are parallel to the local magnetic field. In terms of the vorticity source behind spinning motion, we categorized CoSCos into two classes. The CoSCo-I, or magnetic tension-driven swirls, are generated due to the continuous perturbation of magnetic fields by the turbulent granules at the photospheric height. They are also characterized by co-spatial magnetic, velocity swirls, and oppositely phased velocity and magnetic field perturbations. The twisted magnetic fields at the exact location of the swirl provide a strong tension force and therefore excite CoSCo-I. The second kind, CoSCo-II, forms next to spicules by the misaligned density and temperature gradients existing at the spicule periphery. It is formally known as Baroclinic instability. Here we report a completely novel category of swirl, CoSCo-II, which is indirectly induced by the spicular jets in the atmosphere. For CoSCo-II, the magnetic swirl is not detected at the same location as the velocity swirl. Apart from differences, both types of CoSCos frequently overlap and rotate spicules and propagate above the chromosphere with the local Alfvén speed. Hence signatures of rotating clusters of spicules both in observations and simulations confirm that rotating spicules are indirect evidence of the presence of CoSCos in the solar atmosphere.
Further, we explore the energy and mass flux contribution of spicules and swirls to the solar corona, which can support against the local radiative losses and supply mass and momentum to the solar wind. We find that the rotational energy of swirls and mass flux contribution of spicules are anti-correlated in time as the spinning motion is mostly dominant at the falling phase of the spicule. A curious phenomenon is noticed about the mass and the Poynting fluxes carried by spicules. The Poynting flux curve is anti-correlated with mass flux, although it correlates with the rotational energy of swirls. Hence it indicates that CoSCos form by drawing energy from the thermal and magnetic energy reservoir of spicules, and energy is transferred to much higher heights due to their tall structure. We also notice that the Poynting fluxes are not just transported by spicules but also by the surrounding regions that include the dimmer regions of the drapery as well as the swirls. For the horizontally averaged mass flux over the domain, we observe a dominant periodic profile in time due to the solar global acoustic oscillation

(p-mode) and the Domino effect on the subsequent upper layer of the atmosphere. We estimate that the simulated mass flux is adequate to support the mass reservoir of the fast solar wind. Therefore for a complete picture of momentum and energy transport to the solar wind, it is crucial to consider this interplay effect between spicules and CoSCos.

Finally in Chapter 5, we compare our rMHD model results with two publicly available rMHD setups from the Bifrost code. Surprisingly we find some remarkable similarities in the qualitative and quantitative aspects of the Pencil and Bifrost data cubes. However, several differences are also present in terms of the characteristics of spicules, swirls, thermodynamic quantities, and overall magnetic topology. Hence it helps us to understand essential physical processes responsible for such parallels and opens up the door to future studies for coherent physical outcomes across different numerical frameworks.

6.2 Future Prospects

We believe the study we have presented here has lot of scope in the future for gaining further knowledge about the forest of spicules and its' extensive influence on the solar wind.
In this thesis, we uncover a new facet of spicules that turns out to be a manifestation of the two-dimensional plasma drapery. In relation to the dynamics of spicules, it is found that the entire plasma inside the synthetic solar spicule does not rise and fall in unison. We have also reported a new class of swirl, CoSCo-II, which is indirectly induced by the spicular jets in the atmosphere. It would be captivating to detect observational counterparts of mentioned features with the help of unprecedentedly resolved data sets of the state-of-the-art Daniel K. Inouye Solar Telescope (DKIST). From our existing numerical datasets of the rMHD model, it is possible to characterize shorter and taller distributions of spicules in connection with the strength of shock fronts. One can also perform an extensive statistical survey on CoSCo-I and II to determine their relative contribution of transferring the kinetic energy flux and the Poynting flux to the solar corona.

Our current 3-dimensional radiation magnetohydrodynamics model has built the foundation to address several unresolved questions in solar physics. Presently, it is not understood how the slow solar wind with a speed slower than $500\,\mathrm{km\,s^{-1}}$ originates in the lower atmosphere of the sun. It is suggested that coronal hole boundaries with the Quiet Sun region (Fisk & Schwadron, 2001) or coronal holes with diverging magnetic fields (Wang & Sheeley, 1992) can drive the slow solar wind. Therefore the magnetic topology at the photospheric height plays a pivotal role in characterizing the wind. Our current 3D rMHD model is suitable for investigating different magnetic environments, e.g., the coronal hole boundary region in the neighborhood of the Quiet Sun area. By including sub-surface magnetic flux emergence partially over the domain

and with background vertical magnetic fields, we expect that spicules, CoSCos, reconnected, and blowout jets will be triggered at the simulated coronal hole boundary. Then we can shed light on several important scientific themes, e.g., (a) mass and momentum flux budget of slow solar wind from the contribution of spicules and swirls (b) genesis of ubiquitous magnetic switchbacks (c) coronal heating due to the photospheric flux emergence in contrast with the Poynting flux transfer through dynamic features like spicules and swirls (d) statistical survey of solar wind acceleration contributed by p-mode driven and magnetic reconnection driven spicules or blowout jets. We believe extensive studies following such themes have great potential to address several critical science questions of the DKIST facility (Rast et al., 2021).

References

Anan T., et al., 2010, *Pub. Astron. Soc. Japan* , 62, 871

Antolin P., Schmit D., Pereira T. M. D., De Pontieu B., De Moortel I., 2018, *Astrophys. J.* , 856, 44

Asplund M., 2005, *Ann. Rev. of Astron. Astrophys.*, 43, 481

Bai Y., Crumeyrolle O., Mutabazi I., 2015, Phys. Rev. E, 92, 031001

Ballai I., Forgács-Dajka E., Marcu A., 2007, Astronomische Nachrichten, 328, 734

Barbulescu M., Ruderman M. S., Van Doorsselaere T., Erdélyi R., 2019, *Astrophys. J.* , 870, 108

Barnes H., F. H. J., Walters K., 1989, An introduction to rheology. Elsevier, London

Batchelor G. K., 2000, An Introduction to Fluid Dynamics

Bate W., et al., 2022, *Astrophys. J.* , 930, 129

Battaglia A. F., Canivete Cuissa J. R., Calvo F., Bossart A. A., Steiner O., 2021, *Astron. Astrophys.* , 649, A121

Beck C., Bellot Rubio L. R., Schlichenmaier R., Sütterlin P., 2007, *Astron. Astrophys.* , 472, 607

Beckers J. M., 1972, Ann. Rev. A&A, 10, 73

Berger T. E., Title A. M., 2001, *Astrophys. J.* , 553, 449

Berger T. E., et al., 2004, *Astron. Astrophys.* , 428, 613

Bethe H. A., 1939, Physical Review, 55, 103

Bhat P., Brandenburg A., 2016, *Astron. Astrophys.* , 587, A90

Boldyrev S., Huynh D., Pariev V., 2009, Phys. Rev. E, 80, 066310

Bonet J. A., Márquez I., Sánchez Almeida J., Cabello I., Domingo V., 2008, *Astrophys. J. Lett.* , 687, L131

Bourdin P. A., Bingert S., Peter H., 2013, *Astron. Astrophys.* , 555, A123

Braginskii S. I., 1965, Reviews of Plasma Physics, 1, 205

Brandenburg A., et al., 2020, arXiv e-prints, p. arXiv:2009.08231

Buneman O., 1964, Physics of Fluids, 7, S3

Burgess A., 1964, *Astrophys. J.* , 139, 776

Cabeza C., Rosen M., 2007, *International Journal of Bifurcation and Chaos*, 17, 1599

Carlsson M., Leenaarts J., 2012, *Astron. Astrophys.* , 539, A39

Carlsson M., Hansteen V. H., Gudiksen B. V., Leenaarts J., De Pontieu B., 2016, *Astron. Astrophys.* , 585, A4

Casanovas J., 1997, in Schmieder B., del Toro Iniesta J. C., Vazquez M., eds, Astronomical Society of the Pacific Conference Series Vol. 118, 1st Advances in Solar Physics Euroconference. Advances in Physics of Sunspots. p. 3

Chatterjee P., 2020, *Geophysical and Astrophysical Fluid Dynamics*, 114, 213

Chatterjee P., Dey S., 2022, Configuration files for simulations of the solar spicule forest, Zenodo, doi:10.5281/zenodo.5807020

Chatterjee P., Fan Y., 2013, *Astrophys. J. Lett.* , 778, L8

Chatterjee P., Nandy D., Choudhuri A. R., 2004, *Astron. Astrophys.* , 427, 1019

Chatterjee P., Hansteen V., Carlsson M., 2016, *Phys. Rev. Lett.* , 116, 101101

Christensen-Dalsgaard J., et al., 1996, Science, 272, 1286

Conselice C. J., Wilkinson A., Duncan K., Mortlock A., 2016, *Astrophys. J.* , 830, 83

Cook J. W., Cheng C. C., Jacobs V. L., Antiochos S. K., 1989, *Astrophys. J.* , 338, 1176

Danilovic S., 2022, arXiv e-prints, p. arXiv:2208.03744

De Pontieu B., Erdélyi R., James S. P., 2004, *Nature* , 430, 536

De Pontieu B., et al., 2007a, *Pub. Astron. Soc. Japan* , 59, S655

De Pontieu B., et al., 2007b, Science, 318, 1574

De Pontieu B., Hansteen V. H., Rouppe van der Voort L., van Noort M., Carlsson M., 2007c, *Astrophys. J.* , 655, 624

De Pontieu B., Carlsson M., Rouppe van der Voort L. H. M., Rutten R. J., Hansteen V. H., Watanabe H., 2012, *Astrophys. J. Lett.* , 752, L12

De Pontieu B., et al., 2014, *Solar Phys.* , 289, 2733

Dedner A., Kemm F., Kröner D., Munz C. D., Schnitzer T., Wesenberg M., 2002, Journal of Computational Physics, 175, 645

Dere K. P., Landi E., Mason H. E., Monsignori Fossi B. C., Young P. R., 1997, *Astron. Astrophys. Suppl.* , 125, 149

Dey S., Chatterjee P., Murthy O. V. S. N., Korsós M. B., Liu J., Nelson C. J., Erdélyi R., 2022, Nature Physics, 18, 595

Dinic J., Sharma V., 2019, *PNAS*, 116, 8766

Engquist B., Majda A., 1977, Mathematics of Computation, 31, 629

Fan Y., 2017, *Astrophys. J.* , 844, 26

Faraday M., 1831, *Phil. Trans. Soc. Lond., 52, 319*

Feldman U., Mandelbaum P., Seely J. F., Doschek G. A., Gursky H., 1992, Astrophysical Journal Supplement Series, 81, 387

Finley A. J., Brun A. S., Carlsson M., Szydlarski M., Hansteen V., Shoda M., 2022, Astron. Astrophys. , 665, A118

Fisk L. A., Schwadron N. A., 2001, Astrophys. J. , 560, 425

Fleck B., Carlsson M., Khomenko E., Rempel M., Riva F., Steiner O., Vigeesh G., 2022, in 44th COSPAR Scientific Assembly. Held 16-24 July. p. 2503

García R. A., et al., 2005, Astron. Astrophys. , 442, 385

Gombosi T. I., Tóth G., De Zeeuw D. L., Hansen K. C., Kabin K., Powell K. G., 2002, Journal of Computational Physics, 177, 176

Goodridge C. L., Hentschel H. G. E., Lathrop D. P., 1996, Phys. Rev. Lett. , 76, 1824

Goodridge C. L., Shi W. T., Hentschel H. G. E., Lathrop D. P., 1997, Phys. Rev. E , 56, 472

Goodridge C. L., Hentschel H. G. E., Lathrop D. P., 1999, Phys. Rev. Lett. , 82, 3062

Graftieaux L., Michard M., Grosjean N., 2001, Measurement Science and Technology, 12, 1422

Grevesse N., Sauval A. J., 1998, Space Sci. Rev. , 85, 161

Gruszecki M., Nakariakov V. M., Van Doorsselaere T., Arber T. D., 2010, Phys. Rev. Lett., 105, 055004

Gudiksen B. V., Carlsson M., Hansteen V. H., Hayek W., Leenaarts J., Martínez-Sykora J., 2011, Astron. Astrophys. , 531, A154

Haerendel G., 1992, Nature , 360, 241

Haller G., Hadjighasem A., Farazmand M., Huhn F., 2016, Journal of Fluid Mechanics, 795, 136

Hansen C. J., Kawaler S. D., 1994, Stellar Interiors. Physical Principles, Structure, and Evolution., doi:10.1007/978-1-4419-9110-2.

Hansteen V. H., De Pontieu B., Rouppe van der Voort L., van Noort M., Carlsson M., 2006, Astrophys. J. Lett. , 647, L73

Heggland L., Pontieu B. D., Hansteen V. H., 2007, The Astrophysical Journal, 666, 1277

Heggland L., Hansteen V. H., De Pontieu B., Carlsson M., 2011, Astrophys. J. , 743, 142

Heinemann T., Dobler W., Nordlund Å., Brandenburg A., 2006, Astron. Astrophys. , 448, 731

Henriques V. M. J., Kuridze D., Mathioudakis M., Keenan F. P., 2016, Astrophys. J. , 820, 124

Hollweg J. V., 1982, Astrophys. J. , 257, 345

Hudson H. S., 1991, Solar Phys. , 133, 357

Iglesias C. A., Rogers F. J., 1996, Astrophys. J. , 464, 943

Iijima H., Yokoyama T., 2015, Astrophys. J. , 812, L30

Iijima H., Yokoyama T., 2017, Astrophys. J. , 848, 38

Jafarzadeh S., et al., 2017, Astrophysical Journal Supplement Series, 229, 9

Judge P. G., Carlsson M., 2010, The Astrophysical Journal, 719, 469

Judge P. G., Tritschler A., Chye Low B., 2011, Astrophys. J. Lett. , 730, L4

Judge P. G., Reardon K., Cauzzi G., 2012, Astrophys. J. Lett. , 755, L11

Keil S. L., Canfield R. C., 1978, Astron. Astrophys. , 70, 169

Khomenko E., Vitas N., Collados M., de Vicente A., 2018, Astron. Astrophys. , 618, A87

Kitiashvili I. N., Kosovichev A. G., Mansour N. N., Wray A. A., 2011, Astrophys. J. Lett. , 727, L50

Kitiashvili I. N., Kosovichev A. G., Mansour N. N., Wray A. A., 2012, Astrophys. J. Lett. , 751, L21

Kosugi T., et al., 2007, Solar Phys. , 243, 3

Kriginsky M., Oliver R., Freij N., Kuridze D., Asensio Ramos A., Antolin P., 2020, arXiv e-prints, p. arXiv:2006.01809

Kundu P. K., Cohen I. M., 2008, Fluid Mechanics: Fourth Edition

Kuridze D., Zaqarashvili T. V., Henriques V., Mathioudakis M., Keenan F. P., Hanslmeier A., 2016, Astrophys. J. , 830, 133

Landi E., Chiuderi Drago F., 2008, Astrophys. J. , 675, 1629

Landi E., Landini M., 1999, Astron. Astrophys. , 347, 401

Leake J. E., Lukin V. S., Linton M. G., 2013, Physics of Plasmas, 20, 061202

Leenaarts J., 2020, Living Reviews in Solar Physics, 17, 3

Lehmann A., Federrath C., Wardle M., 2016, Mon. Not. Roy. Astron. Soc. , 463, 1026

Lemen J. R., et al., 2012, Solar Phys. , 275, 17

Lipartito I., Judge P. G., Reardon K., Cauzzi G., 2014, Astrophys. J. , 785, 109

Liu J., Nelson C. J., Snow B., Wang Y., Erdélyi R., 2019, Nat. Comm., 10, 3504

Liu J., Jess D., Erdélyi R., Mathioudakis M., 2023, Astron. Astrophys. , 674, A142

Longcope D. W., McLeish T. C. B., Fisher G. H., 2003, Astrophys. J. , 599, 661

Lumley J. L., Newman G. R., 1977, Journal of Fluid Mechanics, 82, 161–178

Lyra W., McNally C. P., Heinemann T., Masset F., 2017, Astron. J. , 154, 146

Malanushenko A., Cheung M. C. M., DeForest C. E., Klimchuk J. A., Rempel M., 2022, Astrophys. J. , 927, 1

Maoz D., 2016, Astrophysics in a Nutshell

Marciano Y., Brochard-Wyart F., 1995, Macromolecules, 28, 985

Martínez-Sykora J., Hansteen V., Pontieu B. D., Carlsson M., 2009, Astrophys. J. , 701, 1569

Martínez-Sykora J., De Pontieu B., Hansteen V. H., Rouppe van der Voort L., Carlsson M., Pereira T. M. D., 2017, Science. , 356, 1269

Martínez-Sykora J., Hansteen V. H., Gudiksen B., Carlsson M., De Pontieu B., Gosić M., 2019, Astrophys. J. , 878, 40

Meyer J. P., 1985, Astrophysical Journal Supplement Series, 57, 173

Mitalas R., Sills K. R., 1992, Astrophys. J. , 401, 759

Mooroogen K., Morton R. J., Henriques V., 2017, Astron. Astrophys. , 607, A46

Munro R. H., Jackson B. V., 1977, Astrophys. J. , 213, 874

Narang N., Arbacher R. T., Tian H., Banerjee D., Cranmer S. R., DeLuca E. E., McKillop S., 2016, Solar Phys. , 291, 1129

Ni L., Ji H., Murphy N. A., Jara-Almonte J., 2020, Proceedings of the Royal Society of London Series A, 476, 20190867

Nordlund A., 1982, Astron. Astrophys. , 107, 1

Nordlund Å., Stein R. F., Asplund M., 2009, Living Reviews in Solar Physics, 6, 2

Ogilvie G. I., Proctor M. R. E., 2003, J. Fluid Mech. , 476, 389

Oldroyd J. G., 1950, Proc. Roy. Soc. London, 200, 523

Orta J. A., Huerta M. A., Boynton G. C., 2003, Astrophys. J. , 596, 646

Oxley W., Scalisi J., Ruderman M. S., Erdélyi R., 2020, Astrophys. J. , 905, 168

Parker E. N., 1958, Astrophys. J. , 128, 664

Pencil Code Collaboration et al., 2021, The Journal of Open Source Software, 6, 2807

Pereira T. M. D., De Pontieu B., Carlsson M., 2012, Astrophys. J. , 759, 18

Pereira T. M. D., et al., 2014, Astrophys. J. Lett. , 792, L15

Petschek H. E., 1958, Reviews of Modern Physics, 30, 966

Pietarila A., Hirzberger J., Zakharov V., Solanki S. K., 2009, Astron. Astrophys. , 502, 647

Pishkalo M. I., 1994, Astronomische Nachrichten, 315, 391

Plateau J. A. F., 1873, Paris: Gauthier Villars, 2

Powell K. G., 1994, Approximate Riemann solver for magnetohydrodynamics (that works in more than one dimension)

Priest E., 2014, Magnetohydrodynamics of the Sun, doi:10.1017/CBO9781139020732.

Rajchenbach J., Clamond D., Leroux A., 2013, Phys. Rev. Lett. , 110, 094502

Rast M. P., 2003, Astrophys. J. , 597, 1200

Rast M. P., et al., 2021, Solar Phys. , 296, 70

Rayleigh L., 1892, Phil. Mag., 34, 145

Rempel M., 2016, Astrophys. J. , 834, 10

Rieutord M., Rincon F., 2010, Living Reviews in Solar Physics, 7, 2

Roberts B., 1979, Solar Phys. , 61, 23

Rompolt B., 1975, Solar Phys. , 41, 329

Rouppe van der Voort L., de la Cruz Rodríguez J., 2013, Astrophys. J. , 776, 56

Rutten R. J., Kostik R. I., 1982, Astron. Astrophys. , 115, 104

Sakaue T., Shibata K., 2020, Astrophys. J. , 900, 120

Samanta T., et al., 2019, Science. , 366, 890

Scalisi J., Ruderman M. S., Erdélyi R., 2021, Astrophys. J. , 922, 118

Scalisi J., Ruderman M. S., Erdélyi R., 2023, Astrophys. J. , 951, 60

Scharmer G. B., 2006, Astron. Astrophys. , 447, 1111

Secchi A., 1877, L'astronomia in Roma nel pontificato DI Pio IX.

Sekse D. H., Rouppe van der Voort L., De Pontieu B., Scullion E., 2013, Astrophys. J. , 769, 44

Shelyag S., Keys P., Mathioudakis M., Keenan F. P., 2011, Astron. Astrophys. , 526, A5

Shetye J., Verwichte E., Stangalini M., Judge P. G., Doyle J. G., Arber T., Scullion E., Wedemeyer S., 2019, Astrophys. J. , 881, 83

Shibata K., et al., 2007, Science. , 318, 1591

Singh B., Srivastava A. K., Sharma K., Mishra S. K., Dwivedi B. N., 2022, Mon. Not. Roy. Astron. Soc. , 511, 4134

Skogsrud H., Rouppe van der Voort L., De Pontieu B., Pereira T. M. D., 2015, Astrophys. J. , 806, 170

Socas-Navarro H., Elmore D., Pietarila A., Darnell A., Lites B. W., Tomczyk S., Hegwer S., 2006, Solar Phys. , 235, 55

Solanki S. K., 2003, Astron. Astrophys. Rev. , 11, 153

Solanki S. K., Stenflo J. O., 1984, Astron. Astrophys. , 140, 185

Spitzer L., 1962, Physics of Fully Ionized Gases

Srivastava A. K., Singh B., Murawski K., Chen Y., Sharma K., Yuan D., Tiwari S. K., Mathioudakis M., 2023, European Physical Journal Plus, 138, 209

Stein R. F., Nordlund Å., 1998, Astrophys. J. , 499, 914

Sterling A. C., 2000, Solar Phys. , 196, 79

Sterling A. C., Mariska J. T., Shibata K., Suematsu Y., 1991, Astrophys. J. , 381, 313

Sterling A. C., Moore R. L., DeForest C. E., 2010a, Astrophys. J. Lett. , 714, L1

Sterling A. C., Harra L. K., Moore R. L., 2010b, Astrophys. J. , 722, 1644

Sterling A. C., Moore R. L., Samanta T., Yurchyshyn V., 2020, Astrophys. J. Lett. , 893, L45

Suematsu Y., Shibata K., Nishikawa T., Kitai R., 1982, Solar Phys. , 75, 99

Suematsu Y., Wang H., Zirin H., 1995, Astrophys. J. , 450, 411

Suematsu Y., et al., 2008a, Solar Phys. , 249, 197

Suematsu Y., Ichimoto K., Katsukawa Y., Shimizu T., Okamoto T., Tsuneta S., Tarbell T., Shine R. A., 2008b, in Matthews S. A., Davis J. M., Harra L. K., eds, Astronomical Society of the Pacific Conference Series Vol. 397, First Results From Hinode. p. 27

Tegmark M., Silk J., Rees M. J., Blanchard A., Abel T., Palla F., 1997, Astrophys. J. , 474, 1

Terradas J., Andries J., Goossens M., Arregui I., Oliver R., Ballester J. L., 2008, Astrophys. J. Lett. , 687, L115

Tian H., et al., 2014, Science, 346, 1255711

Tóth G., Meng X., Gombosi T. I., Ridley A. J., 2011, Journal of Geophysical Research (Space Physics), 116, A07211

Tsiropoula G., Tziotziou K., Kontogiannis I., Madjarska M. S., Doyle J. G., Suematsu Y., 2012, Space Sci. Rev. , 169, 181

Tsuneta S., et al., 2008, Solar Phys. , 249, 167

Tziotziou K., Tsiropoula G., Kontogiannis I., Scullion E., Doyle J. G., 2018, Astron. Astrophys. , 618, A51

Uchida Y., 1961, Pub. Astron. Soc. Japan , 13, 321

Van Doorsselaere T., Antolin P., Yuan D., Reznikova V., Magyar N., 2016, Frontiers in Astronomy and Space Sciences, 3, 4

Vernazza J. E., Avrett E. H., Loeser R., 1981, Astrophysical Journal Supplement Series, 45, 635

Vögler A., Schüssler M., 2003, Astronomische Nachrichten, 324, 399

Wagner C., Müller H. W., Knorr K., 1999, Phys. Rev. Lett. , 83, 308

Wang Y. M., Sheeley N. R. J., 1992, Astrophys. J. , 392, 310

Wang Y., Noyes R. W., Tarbell T. D., Title A. M., 1995, Astrophys. J. , 447, 419

Wang Y., Yokoyama T., Iijima H., 2021, Astrophys. J. Lett. , 916, L10

Warnecke J., Bingert S., 2020, Geophysical and Astrophysical Fluid Dynamics, 114, 261

Wedemeyer-Böhm S., Rouppe van der Voort L., 2009, Astron. Astrophys. , 507, L9

Wedemeyer-Böhm S., Scullion E., Steiner O., Rouppe van der Voort L., de La Cruz Rodriguez J., Fedun V., Erdélyi R., 2012, Nature , 486, 505

Williamson J. H., 1980, Journal of Computational Physics, 35, 48

Withbroe G. L., Noyes R. W., 1977, Ann. Rev. of Astron. Astrophys., 15, 363

Wöger F., Rimmele T., Ferayorni A., Beard A., Gregory B. S., Sekulic P., Hegwer S. L., 2021, Solar Phys. , 296, 145

Wójcik D., Kuźma B., Murawski K., Musielak Z. E., 2020, Astron. Astrophys. , 635, A28

Wu S. T., Wang J. F., 1987, Computer Methods in Applied Mechanics and Engineering, 64, 267

Yadav N., Cameron R. H., Solanki S. K., 2021, Astron. Astrophys. , 645, A3

Young, R.J., and Lovell, P.A 2011, Introduction to Polymers. Elsevier, Boca Raton, doi:https://doi.org/10.1201/9781439894156

Zaqarashvili T. V., Erdélyi R., 2009, Space Sci. Rev. , 149, 355

Zeff B. W., Kleber B., Fineberg J., Lathrop D. P., 2000, Nature , 403, 401

Zel'dovich Y. B., Raizer Y. P., 1967, Physics of shock waves and high-temperature hydrodynamic phenomena

Zhang Y. Z., Shibata K., Wang J. X., Mao X. J., Matsumoto T., Liu Y., Su J. T., 2012, Astrophys. J. , 750, 16

Zhou J., Adrian R. J., Balachandar S., Kendall T. M., 1999, Journal of Fluid Mechanics, 387, 353

Zirin H., 1988, Astrophysics of the sun

de Vicente A., del Pino Alemán T., Trujillo Bueno J., 2021, Astrophys. J. , 912, 63

van Noort M. J., Rouppe van der Voort L. H. M., 2006, Astrophys. J. Lett. , 648, L67

van Wettum T., 2013, PhD thesis, Georg August University of Gottingen, Germany